

DESULPHURIZATION KINETICS OF
MOLTEN IRON BY MAGNESIUM VAPOUR

by

Gordon A. IRONS

A Thesis Submitted to the Faculty of Graduate Studies and Research
in Partial Fulfilment of the Requirements for the Degree of
Doctor of Philosophy

Department of Mining and Metallurgical Engineering
McGill University
Montreal, Canada

August 1978

ABSTRACT

Magnesium is used for the desulphurization of iron from the blast furnace, yet the kinetic reaction mechanism is unknown. In order to calculate the specific dissolution rate from the magnesium bubbles, a preliminary study was conducted on argon bubble formation in 60 kg heats of carbon-saturated iron at 1523 K. The frequency of bubble formation was measured over a wide range of variables. Supplementary information from X-ray cinematographic observations in a low temperature alloy (indium-gallium), enabled the postulation of a mechanism for bubble formation in liquid metals.

In the second part of the study, magnesium vapour was injected into the iron. It was found that the bubbles were at least 10 cm^3 initially, and dissolved with a mass transfer coefficient of $4.6 \pm 3.4 \times 10^{-3} \text{ cm s}^{-1}$. Furthermore, the desulphurization primarily occurred in the liquid by a second order (with respect to dissolved magnesium and sulphur) heterogeneous reaction, for which a specific mechanism is postulated.

RESUME

Le magnésium est utilisé pour la désulfurisation du fer du haut fourneau, cependant le mécanisme de la cinétique de la réaction est inconnu. Pour calculer la vitesse de dissolution spécifique des bulles de magnésium, une étude préliminaire a été faite sur la formation des bulles d'argon dans 60 kg de fer fondu, saturé de carbone à 1523 K. La fréquence de formation des bulles a été mesurée d'après un large éventail de variables. Des informations supplémentaires d'un alliage (indium-gallium) à basse température, émanant d'observations cinématographiques par rayons X, a permis de postuler un mécanisme de formation de bulles dans les métaux liquides.

Dans la deuxième partie de l'étude, la vapeur de magnésium a été injectée dans le fer. Il a été trouvé que le volume initial des bulles était d'au moins 10 cm^3 et qu'elles ont été dissoutes avec un coefficient de transfert de masse de $4.6 \pm 3.4 \times 10^{-3} \text{ cm s}^{-1}$. De plus, la désulfurisation s'est effectuée dans le liquide, en plus grande part, suivant une réaction hétérogène de second ordre (fonction du magnésium et du soufre dissout), pour laquelle un mécanisme spécifique a été proposé.

ACKNOWLEDGEMENTS AND AUTHENTICATION

Sincere gratitude is extended to Professor R.I.L. Guthrie for his supervision and assistance during the course of this work. Discussions with Professor W.T. Thompson were also very helpful. The cooperation of Dr. K.G. Davis in the Foundry Division of CANMET is also gratefully acknowledged. He performed the X-ray cinematography experiments with his equipment, under conditions specified by the author. The analysis and interpretation of the results are the author's.

Special thanks are due to Mr. R.J. Barnhurst who operated and maintained the induction furnace, as well as monitored the strip chart recorder during the experiments. Similar assistance from Mr. S.J. Calvert during the summer of 1977 with the experiments, as well as with graphite machining and magnesium analysis, was also greatly appreciated.

The expert advice of Mr. M. Knoepfel on machining, Mrs. M. McTague on atomic absorption spectrometry and the DATAC Laboratory staff on electronics were very much appreciated, although virtually all aspects of equipment design, construction, machining of graphite, electronic repairs and modifications, experimental procedure and chemical analysis were performed by the author. (The silicon analysis was contracted to Concordia University.) The difficult task of welding and re-welding of the magnesium retort was capably performed by the cooperative staff at the Canadian Liquid Air Research Laboratory, under the management of Mr. J. Read. Quebec Iron and Titanium, Ltd. very kindly supplied the high quality iron used throughout these experiments.

The attractive appearance of this manuscript is largely due to the efforts of Mrs. H. Rousseau in typing, Mrs. M. Oeltzschner in preparing the diagrams for Part II and to Mr. R. Selbach in preparing the photographs.

The National Research Council of Canada, the Graduate Faculty of McGill University and the Quebec Ministry of Education are all gratefully acknowledged for the scholarships they granted to the author.

TABLE OF CONTENTS

	<u>Page</u>
ABSTRACT	i
RESUME	ii
ACKNOWLEDGEMENT AND AUTHENTICATION	iii
<u>INTRODUCTION TO THE THESIS</u>	1
PART I: BUBBLE FORMATION IN LIQUID METALS	4
ABSTRACT	5
INTRODUCTION	6
THEORY	8
Constant Volume Regime	8
Contact Angle Considerations	10
Constant Frequency Regime	12
Gas Chamber Volume Effects	15
APPARATUS AND PROCEDURE	19
High Temperature System	19
X-Ray System	24
RESULTS	27
High Temperature System	27
DISCUSSION	32
Description of High Temperature Results	32
Nozzle Orientation	39
Surface Tension Effects	39
Discussion of X-Ray Results	42
Sources of Experimental Error	44
Capacitance Effects	47
Mechanism of Bubble Formation	52
Comparison with Previous Work	57
CONCLUSIONS	60
NOMENCLATURE	61
REFERENCES	63
LIST OF FIGURES AND TABLE	65

	<u>Page</u>
PART II: MAGNESIUM DESULPHURIZATION OF IRON-CARBON MELTS	68
ABSTRACT	69
INTRODUCTION	70
PREVIOUS WORK	71
Thermodynamics	71
Magnesium Solubility in Iron	71
Desulphurization	71
Mass Transfer and Reactions	75
Liquid Phase Control	75
Gas Phase Control	79
Adsorption	79
Homogeneous Nucleation	82
Heterogeneous Deoxidation	86
APPARATUS AND PROCEDURE	90
Apparatus	90
Procedure	92
Chemical Analysis	94
RESULTS	95
DISCUSSION	103
Calculations	103
Transport To and From Bubbles	103
Gas Phase Control	113
Homogeneous Nucleation	114
Heterogeneous Desulphurization	116
Proposed Mechanism of Desulphurization	118
Model Predictions	121
Holding Periods	124
Experimental Error	125
Industrial Implications	127
CONCLUSIONS	132
LIST OF SYMBOLS	134
REFERENCES	138
LIST OF FIGURES	142
LIST OF TABLES	144
<u>CONCLUSIONS TO THE THESIS</u>	145
General Conclusions	146
Part I	146
Part II	147
Claim to Originality	149

	<u>Page</u>
APPENDIX A: Magnesium Desulphurization Practice	151
References	155
APPENDIX B: Magnesium Solubility	156
References	161
APPENDIX C: Mass Transfer Correlations	162
References	165
Nomenclature	166
APPENDIX D: Extra Experimental Results and Calculations	167
References	179
APPENDIX E: Computer Simulations	180
Nomenclature	181
List of Figures for Appendices	185
List of Tables for Appendices	186

INTRODUCTION TO THE THESIS

There is currently a great deal of interest in magnesium desulphurization of blast furnace hot metal. The impetus for this extra refining operation is a result of two diverging trends: the sulphur contents of metallurgical coke are generally increasing, and secondly, sulphur specifications are becoming more stringent, particularly in pipeline grades. Desulphurization in a blast furnace is accomplished by a favourable partition of sulphur between slag and metal, and hence larger slag volumes are required for higher sulphur loading. By employing external desulphurization instead, one can reduce the slag volume and increase the productivity of a blast furnace. Apart from magnesium, lime (CaO) and calcium carbide (CaC_2) are also widely used as desulphurizing agents. The various injection methods have been discussed extensively elsewhere (see Appendix A). The major problem with pure magnesium is that it boils at 1380 K, and consequently explodes when plunged into hot metal which is typically hotter than 1520 K. All previous studies on the magnesium desulphurization processes have attempted to find means of moderating the vaporization. There have been no studies on the kinetics of the desulphurization reaction itself, to determine if any limitations are imposed by reaction kinetics. Preliminary work by the present author^{1,2} indicated that magnesium readily dissolved in iron when little sulphur was present. This fact raised an interesting question about the mechanism of desulphurization, as to whether the reaction proceeds in the bulk of the liquid, or at the bubble interface. A further question is whether an interfacial layer of surface active

sulphur or the reaction product, magnesium sulphide blocks the reaction in any way. The aim of the present study was to answer some of these basic questions.

In that preliminary work^{1,2} with very low sulphur iron, bubble sizes were not measured, so that the specific rates of reaction and transport could only be estimated. In order to overcome this deficiency, a method of measuring the frequency of bubble formation at high temperature in an induction furnace was developed. This work was initially conducted with argon bubbles in iron-carbon alloys. Several interesting phenomena regarding the mechanism of bubble formation in liquid metals were identified. However, the frequency measurement technique only provided indirect insight into the mechanisms of bubble formation and release. Thus a complementary X-ray technique was used to directly observe bubble formation in a low temperature alloy. These two experimental studies have been already published^{3,4}, but appear together, along with some unpublished interpretation as Part I of this Thesis. The work on magnesium desulphurization is presented separately as Part II. There are also five Appendices which contain work from this author's Master's Thesis¹ and calculations concerned with the present experiments. Therefore each Part and Appendix has its own numbering scheme for equations, figures, tables, and references. The present format is intended to improve the readability of the Thesis and conforms with the McGill University Guidelines Concerning Thesis Preparation, Section 7, which states that:

"The candidate has the option, subject to the approval of the Department, of including as part of the thesis the text of an original paper, or papers, suitable for submission to learned journals for publication. In this case the thesis must still conform to all other requirements explained in this document, and additional material (e.g. experimental data, details of equipment and experimental design) may need to be provided. In any case abstract, full introduction and conclusion must be included, and where more than one manuscript appears, connecting texts and common abstract, introduction and conclusions are required. A mere collection of manuscripts is not acceptable; nor can reprints of published papers be accepted.

While the inclusion of manuscripts co-authored by the Candidate and others is not prohibited for a test period, the Candidate is warned to make an explicit statement on who contributed to such work and to what extent, and Supervisors and others will have to bear witness to the accuracy of such claims before the Oral Committee. It should also be noted that the task of the External Examiner is much more difficult in such cases.

The text of this Section 7 should be cited in full in the introduction of any thesis to which it applies.

REFERENCES

1. Irons, G.A.: M.Sc. Thesis, McGill University, 1975.
2. Irons, G.A. and Guthrie, R.I.L.: Can. Met. Quart., 1976 Vol. 15, No.4, pp.325-32.
3. Irons, G.A. and Guthrie, R.I.L.: Met. Trans. B, 1978, Vol. 9B, pp.101-10.
4. Davis, K.G., Irons, G.A. and Guthrie, R.I.L.: in press, Met. Trans. B.

C

C

C

PART I

BUBBLE FORMATION IN LIQUID METALS

ABSTRACT

Bubble formation at graphite nozzles in 60 kg of carbon-saturated iron at 1523 K was investigated. The frequency of bubble formation was measured, and the resulting bubble volumes were between 0.5 and 100 cm³ for flow rates up to 1000 cm³s⁻¹. It was inferred that the bubbles formed at the outer diameter of the nozzle due to the non-wettability of the nozzle. At the higher flow rates a constant frequency (~ 10 bubbles s⁻¹) was established. The bubble volume was also strongly dependent on the volume of the gas train, which is a "capacitance" effect.

Additionally, X-ray cinematography was used to observe nitrogen bubble formation in a room temperature, indium-gallium alloy. The bubbles were seen to form at the outer diameter of the glass nozzle which was pointing sideways; however, they generally spread to the top of the nozzle. A mechanism for bubble formation in metallic systems is postulated.

INTRODUCTION

The injection of gas from submerged nozzles or orifices into liquid metal baths is an integral feature of many metallurgical processing and refining operations. Familiar examples include the mixing of liquid metals by inert gas bubbling through porous plugs or submerged lances, as well as tuyere-based injection processes for producing steel, blister copper or Bessemer matte.

Any successful understanding of process kinetics under such circumstances requires a detailed knowledge of the fluid mechanic phenomena involved. The present paper is concerned specifically with a study of those factors determining bubble sizes when the gas is injected at low and moderate flow rates through submerged nozzles. Although much data have been accumulated on aqueous systems, direct extrapolation to liquid metal systems can often be misleading and yield erroneous conclusions. Consequently the work now described has been largely experimental, due to the paucity of phenomenological data on liquid metal systems. Such studies should precede the development of appropriate theoretical models, which are necessarily mechanistic in approach.

The high temperature system chosen involved graphite lances submerged in carbon-saturated pig iron at 1523 K. It should be noted that the study made use of pilot-scale, induction melting facilities, and this enabled reasonably large gas flow rates and nozzle dimensions to be used in the work.

The bubble volumes in the high temperature study were obtained from the frequency of bubble formation, and thus only indirectly revealed the mechanisms of bubble formation. In the second part of the work the technique of X-ray cinematography was used to make direct observations of individual bubbles formed at a nozzle in a low-temperature, metallic alloy.

THEORY

Although several aspects of bubble formation have received successful theoretical interpretation, as discussed below, many observations still lack quantitative explanations, particularly those at high flow rates.

Constant Volume Regime

It has been found that at low flow rates of gas through submerged nozzles, the volume of the bubble at release, V_{bm} , is determined by a balance between its buoyancy force in the liquid and the surface tension forces constraining it to the inner circumference of the nozzle^{1,2}, hence

$$V_{bm} = \frac{\pi D_{ni} \sigma}{\rho g} \quad (1)$$

These predicted bubble volumes apply to aqueous-type systems in which the liquid wets the nozzle material. However, for non-wetting, metallic-type systems, the bubbles generally tend to form at the outer circumference of the nozzle³⁻⁵, as shown in Figure 1, so that the bubble volume becomes

$$V_{bm} = \frac{\pi D_{no} \sigma}{\rho g} \quad (2)$$

Both relations are restricted to those cases in which the gas flow rate is low and the volume of the gas train is small. As can be seen from Equations (1) and (2), bubble volumes in this so-called "constant-volume" bubbling regime are independent of flow rate.

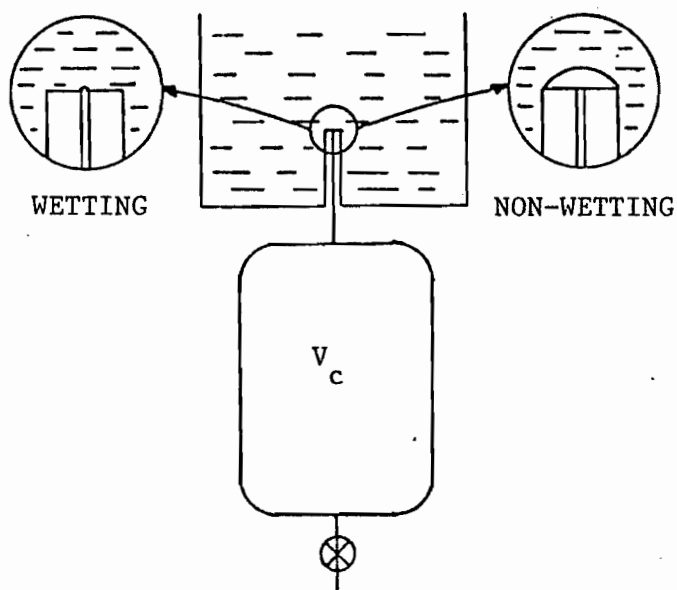


FIGURE 1. Schematic representation of bubble formation in aqueous wetting and metallic non-wetting systems.

Contact Angle Considerations

The terms "wetting" and "non-wetting" are somewhat arbitrary, since a liquid is said not to wet a solid if the contact angle (measured through the liquid) is greater than 90° .^{*} On the other hand, a liquid is only considered to wet a solid if the contact angle is zero.⁶ Most liquid metals exhibit contact angles greater than 90° on most solid substrates, so they are non-wetting.

Contact angles are determined on flat surfaces, so that corners and edges present special situations which are relevant to bubble formation at orifices and nozzles. Gibbs^{7,8} was the first to consider the edge effect and he postulated that a sharp edge, when sufficiently magnified, would be rounded, as shown in Figure 2. When a bubble approaches this edge with an equilibrium contact angle, θ_0 , the bubble would maintain the same tangential contact angle on the microscale. For a right-angle corner, the macroscopically-observed contact angle, θ , can then have two limiting values:

$$(\theta_0 - 90^\circ) < \theta < \theta_0 \quad (3)$$

Relation (3) is commonly called the Gibbs' Inequality. In an experimental investigation of this relationship⁸, it was found that small drops on horizontal plates would spread to the second limit before release. However, for larger drops and bubbles, the effect of buoyancy must also be considered; in fact it predominates. In the absence of gravity, the

* The S.I. unit of angle is the radian (57.3°). Dynes (10^{-5}N) and minutes (60 s) are also used in this part of the Thesis. All compositions expressed in % and ppm are on a weight basis.

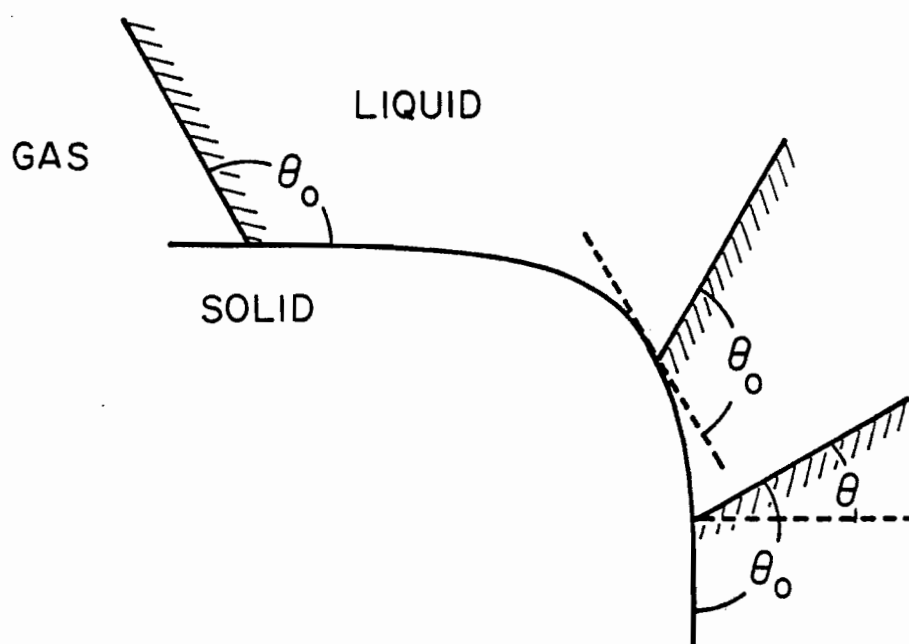


FIGURE 2. The effect of an edge on an approaching gas/liquid interface having an equilibrium contact angle θ_0 and an observed one of θ , after References 7 and 8.

bubble surface is spherical, and its volume from simple geometry⁸ is

$$V_b = \frac{\pi}{24} D^3 \frac{(1 - \cos\phi)^2 (2 + \cos\phi)}{\sin^3\phi} \quad (4)$$

where ϕ is the supplement of the contact angle, $(180^\circ - \theta_o)$.

Constant Frequency Regime

As the gas flow rate is raised above a certain limit, the bubble volume also begins to increase. When this occurs, the static force balance discussed above is no longer applicable. One of the first theories⁹ to explain this phenomenon suggested that during bubble formation, the buoyancy force is balanced against the force required to accelerate the liquid away from the expanding gas-liquid interface. Adopting a classical added mass coefficient of 11/16 for the flow of liquid in the vicinity of a flat, accelerating plate, application of Newton's Law yields:

$$V_b \rho g = \frac{d}{dt} \left[\frac{11}{16} \rho V_b \frac{ds}{dt} \right] \quad (5)$$

where s refers to the distance between the bubble centre and the plane of the orifice. Detachment is postulated to occur when the trailing edge of the bubble is tangential to the orifice. Integrating twice with respect to time, t , Equation (5) then becomes

$$V_b = 1.378 Q^{1.2} g^{-0.6} \quad (6)$$

Equation (6) shows that the bubble volume is almost directly proportional to the flow rate. It follows that the frequency of bubble formation must be practically constant and independent of gas flow rate. In a review¹⁰ of bubble formation theories, it was shown that more complicated models involving such factors as buoyancy, surface tension, liquid inertial forces, viscous drag and/or gas momentum have met with considerable success. However, it is difficult to compare these models directly, as the solutions are generally numerical in nature. A more recent model¹¹ which includes all the above factors agrees quite closely with Equation (6). This model is also in excellent agreement with experimental results in aqueous systems^{12,13}, particularly with respect to the observed square root dependency on orifice diameter which does not appear in Equation (6). In addition, it shows that for low viscosity liquids, such as water and liquid metals, the effect of viscosity is small.

In this so-called "constant frequency" regime, the vertical displacement between successive bubbles is normally equal. However, sometimes two bubbles may rise together, and may in fact even touch one another. Such bubbles are termed "doublets" and their characteristics are summarized in Figure 3. One theoretical model¹⁴ was able to predict that the wake of a preceding bubble could enhance the size of a forming bubble, but the elongated shapes exhibited by the bubbles made quantitative predictions difficult.


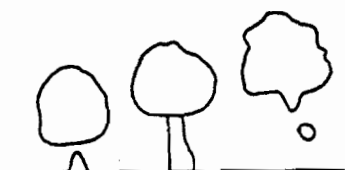
	DOUBLETS	PAIRS
TRACES OF HIGH-SPEED CINEMATOGRAPHY		
DURING FORMATION	FIRST BUBBLE IS FLATTENED OR TOROIDAL, WHILE SECOND IS ELONGATED.	THE SECOND BUBBLE BECOMES A CONNECTING TUBE OR "TAIL" FROM THE ORIFICE TO THE FIRST ONE.
CAUSE	REDUCED PRESSURE IN THE WAKE OF THE FIRST BUBBLE.	RESIDUAL PRESSURE IN THE GAS CHAMBER UPSTREAM.
CHARACTERISTICS	<p>EACH BUBBLE IS 2-15% LARGER THAN A SINGLE BUBBLE.</p> <p>2 BUBBLES OF THE SAME VOLUME WHICH COALESCE DURING RISE.</p> <p>FREQUENTLY REVERT TO SINGLE BUBBLES.</p>	<p>THE PAIR HAS THE SAME VOLUME AS A SINGLE BUBBLE.</p> <p>THE "TAIL" INCREASES IN VOLUME WITH FLOWRATE, AND MAY BECOME DETACHED.</p> <p>UNDER SOME CONDITIONS CAN REVERT TO SINGLE BUBBLES.</p>
CONDITIONS	<p>SMALL V_c.</p> <p>AT LEAST MODERATE FLOWRATES.</p>	<p>LARGE V_c ($N_c \gtrsim 10$).</p> <p>AT ALL FLOWRATES.</p>

FIGURE 3. A comparison of doublet and pair formation with traces of bubbles photographed at high speed, after References 2, 13, 14 and 18.

Gas Chamber Volume Effects

Because of the compressibility of the gas, the volume of the gas train can have a considerable effect on bubble size. As shown in Figure 1, the chamber volume is defined as the volume between the last large pressure drop and the orifice. Tadaki and Maeda² consider that the pressure in this antechamber increases to a maximum prior to bubble release:

$$P_{\max} = P_s + \frac{4\sigma}{D_{ni}} \quad (7)$$

Following detachment, the pressure in the antechamber then drops back to the static pressure:

$$P_{\min} = P_s = P_o + \rho gh \quad (8)$$

Applying the principle of mass conservation before and after release yields

$$V_c P_{\max} = (V_c + V_b) P_{\min} \quad (9)$$

for isothermal expansion of the gas. The bubble volume obtained by combining these three equations then becomes:

$$V_b = \frac{4\sigma V_c}{D_{ni} P_s} \quad (10)$$

However, the bubble volume cannot be varied arbitrarily through manipulating the chamber volume as Equation (10) would predict. Thus, for very small chamber volumes, bubble volumes predicted by Equation (1) exceed those based on Equation (10). As a consequence, such bubbles continue to grow until buoyancy and surface tension forces balance and Equation (1) is satisfied. It is therefore convenient to define a capacitance group, N_c , as the ratio of Equations (10) to (1):

$$N_c = \frac{4\rho g V_c}{\pi D_{ni}^2 P_s} \quad (11)$$

Consequently, formation at low flow rates can be summarized as follows:

$$V_b = V_{bm} \quad , \quad 0 < N_c < 1 \quad (12)$$

$$V_b = N_c V_{bm} \quad , \quad 1 < N_c (< 9) \quad (13)$$

At high chamber volumes, Tadaki and Maeda² found experimentally that

$$V_b = 9.14 V_{bm} \quad , \quad N_c > 9 \quad (14)$$

because "pairs" are formed, as discussed below.

For non-wetting systems, Sano and Mori⁴ demonstrated that the appropriate capacitance group is:

$$N'_c = \frac{4\rho g \sin\theta V_c}{\pi D_{ni} D_{no} P_s} \quad (15)$$

where $\sin\theta$ is assumed to be unity in the absence of measured wetting angles. Also when there is a temperature difference between parts of the chamber volume T_{V_c} and the bath temperature, T_s , this group must be further modified⁴:

$$N'_c = \frac{4\rho g T_s}{\pi D_{ni} D_{no} P_s} \int_0^{V_c} \frac{dV_c}{T_{V_c}} \quad (16)$$

Hughes et al.¹⁵ were the first to suggest the use of a capacitance group, which in their analysis took the form

$$N_c^a = \frac{4(\rho - \rho_g) V_c g}{\pi D_{ni}^2 \rho_g c^2} \quad (17)$$

One can show that N_c^a represents the capacitance group for adiabatic expansion in the antechamber during bubble release, and that

$$N_c = \gamma N_c^a \quad (18)$$

where γ is the ratio of specific heats of the gas¹⁶.

Theoretical models of bubble formation have also been used at higher flow rates for capacitance numbers larger than one. The limiting case is one of "constant pressure" in the antechamber which is achieved when the chamber is much larger in volume than each bubble released. (This is in contrast to the models discussed in the section on constant frequency bubbling in which the chamber volumes were small and "constant flow" of gas was assumed during bubble formation.) The models^{14,17} predict that bubble volume increases with flow rate and

chamber volume, but precise predictions are limited, owing to bubble "pair" formation. These are distinguished from "doublets" in Figure 3. McCann and Prince^{14,18} have used their model to show that the pressure immediately behind the first bubble can be less than the chamber pressure, so that a second bubble will form. As before, the complex shapes of the bubbles preclude the calculation of the size of the second bubble, which is generally considerably smaller than the leading one.

APPARATUS AND PROCEDURE

High Temperature System

These high temperature experiments were performed with carbon-saturated iron at 1523 K using a Tocco Meltmaster Induction Furnace (150 kVA, 400 V, 3 kHz) to melt and hold the 60 kg charge. The alumina crucibles (Engineering Ceramics, Hycor TA530) had an internal diameter of 20 cm and a height of 36 cm. The iron as supplied by Quebec Iron and Titanium contained 4.0% Carbon, 0.1-0.2% Silicon, 0.1% Manganese and 10-100 ppm Sulphur. The purity of the argon was in excess of 99.9%. The graphite chips on the bath surface contained some sulphur. The graphite lances were machined from high grade, fine-grained graphite (Union Carbide, AGSX). One of the lance and nozzle assemblies with the crucible diameter and a typical bath depth is shown to scale in Figure 4. The remainder of the diagram is schematic.

The gas train, shown in Figure 4, was constructed from 3.18 and 6.35 mm steel pipe, except for the larger chamber volume sections. These sections were glass bottles inserted into the gas train by means of O-ring seals. The chamber volumes used were as follows: 23 (without any glass chamber), 342, 615, 1175, 2192 and 2242 cm³. Needle valves were used to produce a large pressure drop (345 KPa) and thus establish the extent of the chamber volume. These two valves (Hoke Inc., 1335G4B and 1654G4B) also accurately and reproducibly controlled the flow rate over three orders of magnitude.

One of the most common ways to determine the bubble volume is to measure the frequency of bubble formation and volumetric flow rate, Q . The volume is then given by:

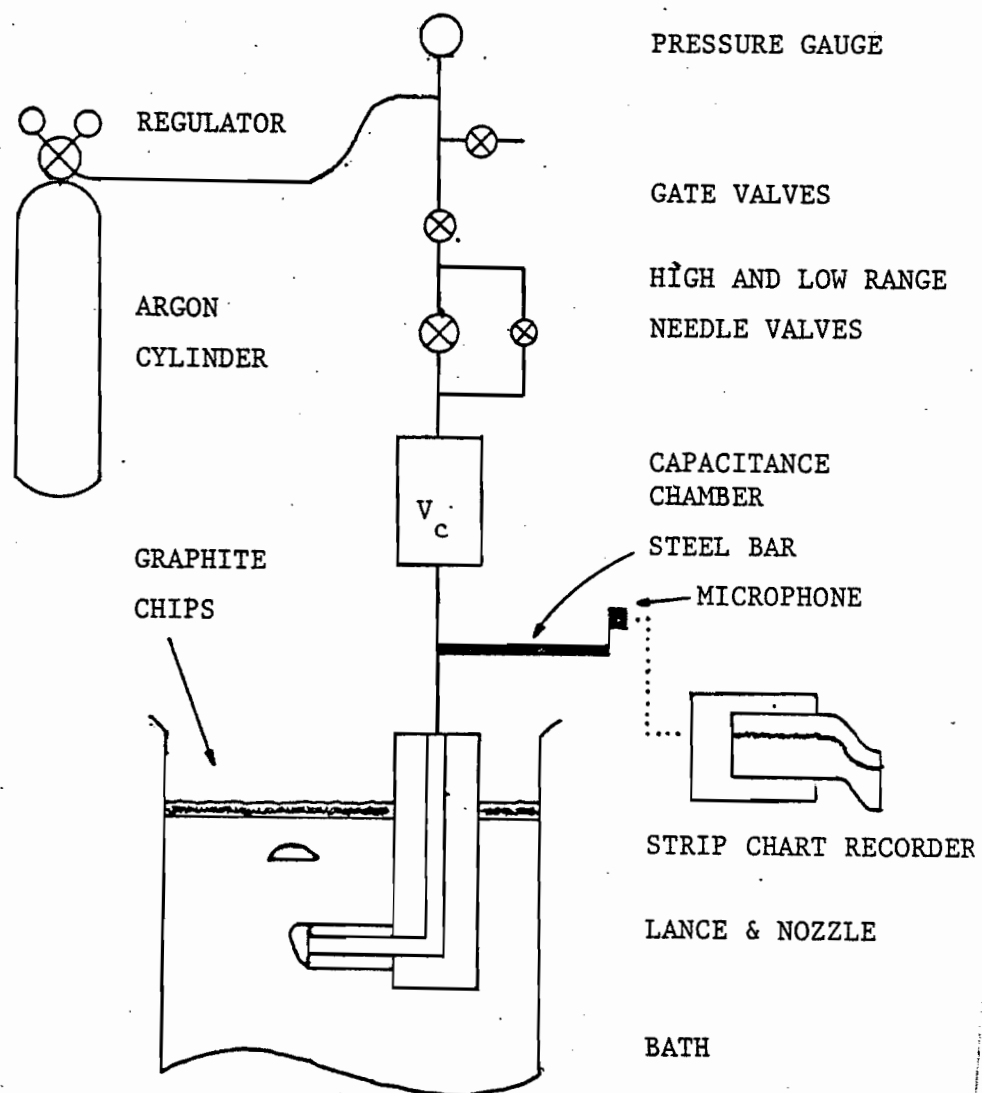


FIGURE 4. A schematic diagram of the high temperature experimental apparatus.

$$v_b = \frac{Q}{f} \quad (19)$$

However, as induction furnaces generate considerable audio- and radio-frequency noise, it was not possible to use an oscilloscope, even with low-pass filters, due to the intensity of the interference. The problem was solved by using a crystal contact microphone to detect the vibrations of a bubble detaching from a nozzle. The output of the microphone was connected to a hot-pen, strip-chart recorder (Hewlett-Packard 7702B Oscillographic Recording System with a 8803A High Gain DC Pre-Amplifier). The recorder was ideally suited to this application because its frequency response (DC to less than 3dB at 125 Hz for a chart deflection of 10 divisions) was such that the bubbles could be clearly detected, while higher frequencies were "filtered" out. A steel bar was used to transmit the vibrations from the gas train to the microphone.

In some cases, the vibrations of the smallest bubbles formed were too small to be detected electronically. Consequently, when a bubble broke the surface the bar was tapped and this could be easily detected as in Figure 6. This procedure was used only up to 3 bubbles/second. Above these frequencies, the bubble could usually be detected electronically with sufficient sensitivity; agreement between manual and electronic counting was within $\pm 5\%$. When there was any doubt about a trace, the frequency of bubbles breaking the surface was compared with the frequency felt by hand on the steel bar and with that being obtained on the recorder. This uncertainty occurred most often at the higher flow rates, and was an important factor in determining the highest useable flow rate.

The meltdown of the iron was performed using an excess of graphite so as to prevent iron oxidation and to ensure carbon saturation. The molten charge was degassed with argon for at least 20 minutes, in order to approach equilibrium. This treatment was necessary for eliminating small bubbles which tended to nucleate at the lance/nozzle junction. (The bubbles were not due to leakage through joints because single piece lance/nozzle assemblies behaved in the same manner.) The nozzles were submerged to a measured depth (usually 7.6 cm) and measurements were commenced once the lance reached temperature. Usually measurements were taken starting with the lowest flow rate and finishing when the traces became indistinct or when splashing of metal became excessive. Pin samples for chemical analysis were taken before and after each series.

The samples were aspirated into quartz tubes and quenched in water. The analysers, standards and analyser accuracies are listed in Table I. The analyser accuracy quoted is the maximum deviation from the standards.

The temperature was monitored after every 1 or 2 measurements with a Leeds and Northrup Dip Tip (Type S) Thermocouple connected to a digital voltmeter. The temperature was maintained at 1523 ± 15 K.

In run 8, ferrous sulphide was plunged into the bath to reduce the surface tension. A 5 cm-diameter graphite bell having a 2.5 cm bore and 1 cm holes along its length contained 300 g of FeS. After the plunge and stirring, any undissolved sulphide was skimmed from the surface and the graphite coverage renewed.

TABLE I
CHEMICAL ANALYSES OF THE PIG IRON BATHS

	CARBON (%)	OXYGEN (PPM)	SULPHUR (PPM)
Leco Analyser	WR 12	RO 17	IR 32
Standard	NBS 122f	LECO 501-644	NBS 122f
Analyser Accuracy	$\pm .05$	± 3	± 5
Run			
1	4.35 \pm .17*	9.0 \pm 2.0*	63.0 \pm 34. *
2	4.47 .19	20.0 4.9	75.3 6.7
3	4.18 .06	17.3 3.2	119. 5.7
4	4.42 .20	10.8 6.3	7.8 3.5
5	4.49 .14	14.0 2.2	15.3 4.6
6	4.43 .09	20.2 6.9	16.8 6.6
7	4.34 .22	16.5 3.7	12.7 4.8
8	4.38 .15	16.2 7.1	74.5 1.6
8 High S	4.46 .15	14.5 -	2250. 330.
9	4.15 .14	18.5 7.7	106. 5.0
Average (Low S)	4.35 \pm .19	15.7 \pm 6.3	54.5 \pm -

* Quoted as ± 1 standard deviation.

At least 20 and usually 40 or more bubbles were counted on the strip chart (except when there was less than one bubble every 30 seconds) and the frequency was averaged. All the experimental conditions and results were computerized to perform the sorting and statistical calculations and to generate Figures 9 to 15.

X-Ray System

Direct observation of the bubbles was achieved through the use of X-ray cinematography. As seen in Figure 5, an X-ray beam from a 200 kV source (Phillips, Model PG 200) was passed through a plexi-glass container filled with liquid metal. A fluorescent screen placed immediately behind the container was used to form an image which was transmitted via an image intensifier to a television camera, the latter three components being contained in the "Decalix 12-1/2", (N.V. Optische Industrie, Delft, Holland). The output from the camera was displayed on a television monitor and recorded on videotape. Movies were taken from the monitor displaying the videotape playback; the results shown in Figure 16 are taken from such individual movie frames.

The volume of the gas chamber used in these experiments was 33 cm^3 . The inner dimensions of the plastic container which was filled to a depth of approximately 95 mm, were 13 mm thick by 65 mm long. The nozzle, which projected approximately 30 mm horizontally into the liquid, was a glass tube having inner and outer diameters of 3.2 and 11.1 mm, respectively. It should be noted that this configuration left only 0.8 mm between the wall and nozzle. Consequently, the proximity of the wall no doubt affected the free flow of liquid around the forming bubbles. How-

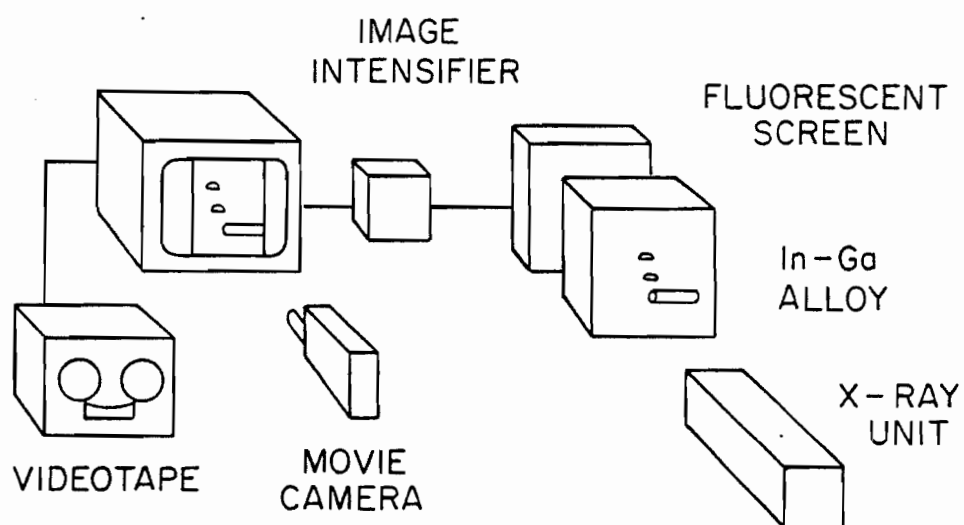


FIGURE 5. Schematic representation of X-ray cinematographic apparatus.

ever, at the low flow rates used in this study, this problem was minimized as visual observation of the melt showed that the rising gas bubbles seldom touched the plexiglass wall.

In choosing a suitable metallic medium, it has been found from previous work¹⁹ that materials with atomic numbers around 25 give the best compromise between image contrast at a liquid/gas interface and sufficient transparency to X-rays. Unfortunately, most readily available low melting point alloys contain high proportions of lead or bismuth, and are therefore unsuitable owing to their opacity to X-rays. Consequently, the alloy chosen for this room temperature study was a gallium-indium eutectic, having a melting point of 289 K and a eutectic composition of 25% In. As the atomic numbers for gallium and indium are 31 and 49, respectively, the alloy was more opaque than would have been ideal. The thickness of the liquid that could be penetrated was limited to around 13 mm. To test for resolution, carbon rods were inserted into the bath; a 3.2 mm diameter rod could not be detected, while one of 6.5 mm diameter could just be seen at the full 180 kV, 4 mA power of the X-ray unit. Consequently, a quantitative study of bubble sizes was not possible.

RESULTS

High Temperature System

Typical traces generated by the strip-chart recorder are shown in Figures 6 to 8. The experimental conditions for both traces in Figure 6 were almost identical, yet the bubbles in 6B were only one-half the volume of those in A. This phenomenon was observed in several cases, and was different from doublet formation as discussed later. The next traces, in Figure 7, were typical of those obtained in the constant frequency regime with small chamber volumes. Referring to Figure 7B, it will be seen that there were several instances in which the regular frequency was briefly interrupted by one of half the value. This behaviour could be attributed to bubble coalescence at the orifice, just prior to release, as observed by Davidson and Amick¹³ in water. The final traces (Figure 8A and B) represent much larger bubbles generated at large chamber volumes in the constant volume regime. One can see a weaker bubble marked with an "X" in Figure 8A. Visual observation of the melt surface confirmed that two bubbles in close proximity broke the surface, followed by a much longer delay until the next "pair". These secondary bubbles closely following the primary bubbles are characteristic of "pair" formation observed in water (Figure 3). Only the total bubble pair volume was calculated from the traces; that is, the smaller bubbles were ignored in the counting procedure.

The principal chemical analyses of the bath are shown in Table I. The values are average ones obtained from at least 5 samples, taken throughout each run. As expected, the carbon contents are very close to graphite saturation at 1523 K which is 4.52% C.²⁰

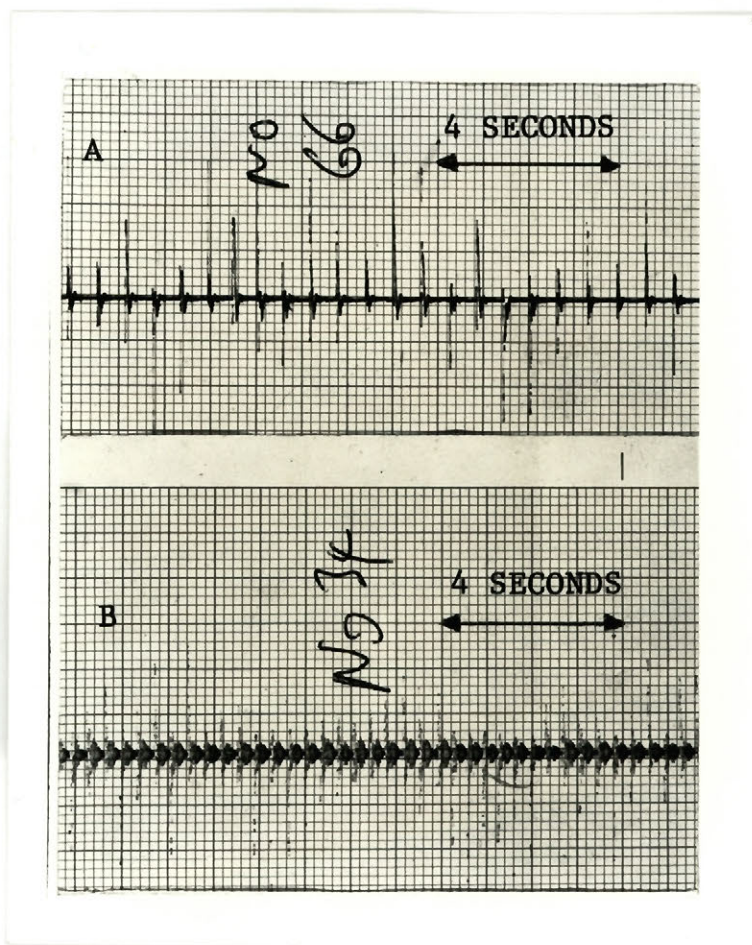


FIGURE 6. Strip-chart traces of bubbles, "tapped" by hand, nozzle outside diameter, 1.27 cm; inside diameter, 0.635 cm; chamber volume, 23 cm³; chart speed, 5 cm s⁻¹; μ V/vertical division, 1000.

A: flow rate, 2.78 cm³s⁻¹; f , 1.65 s⁻¹, bubble volume, 1.68 cm³

B. flow rate, 2.45 cm³s⁻¹; f , 2.71 s⁻¹, bubble volume, 0.904 cm³

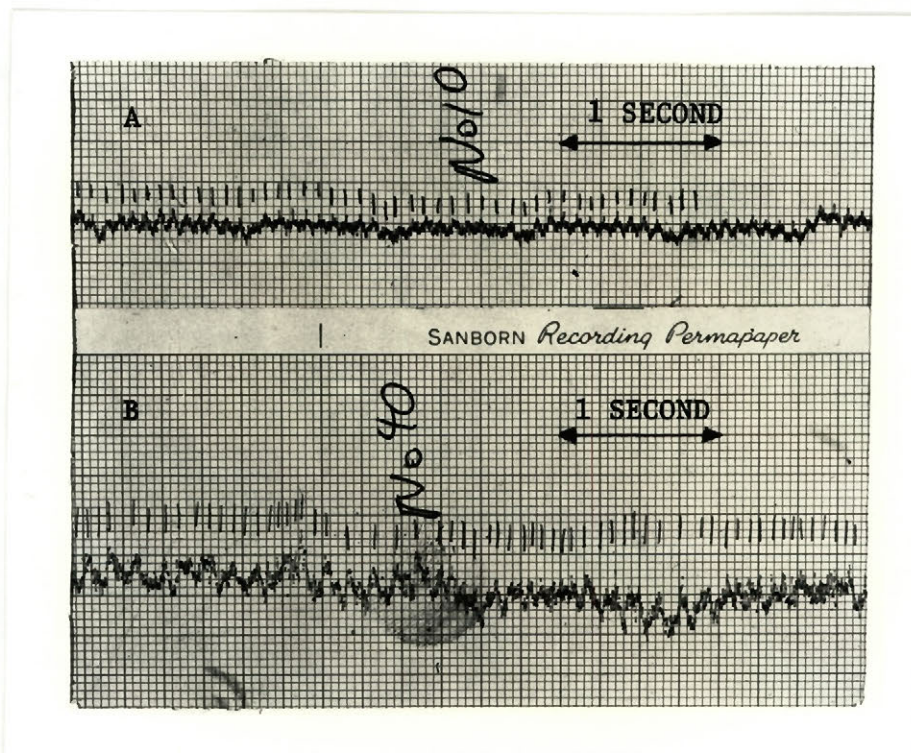


FIGURE 7. Strip-chart traces of bubbles, obtained electronically.

- A. nozzle outside diameter, 5.08 cm; inside diameter, 0.635 cm; chamber volume, 23 cm³; flow rate, 40 cm³s⁻¹; chart speed, 20 cm s⁻¹; μ V/vertical division, 200; f, 11.9; bubble volume, 3.36 cm³
- B. nozzle outside diameter, 1.27 cm; inside diameter, 0.635 cm; chamber volume, 23 cm³; flow rate, 40 cm³s⁻¹; chart speed, 20 cm s⁻¹; μ V/vertical division, 20; f, 13.7 s⁻¹; bubble volume, 2.92 cm³

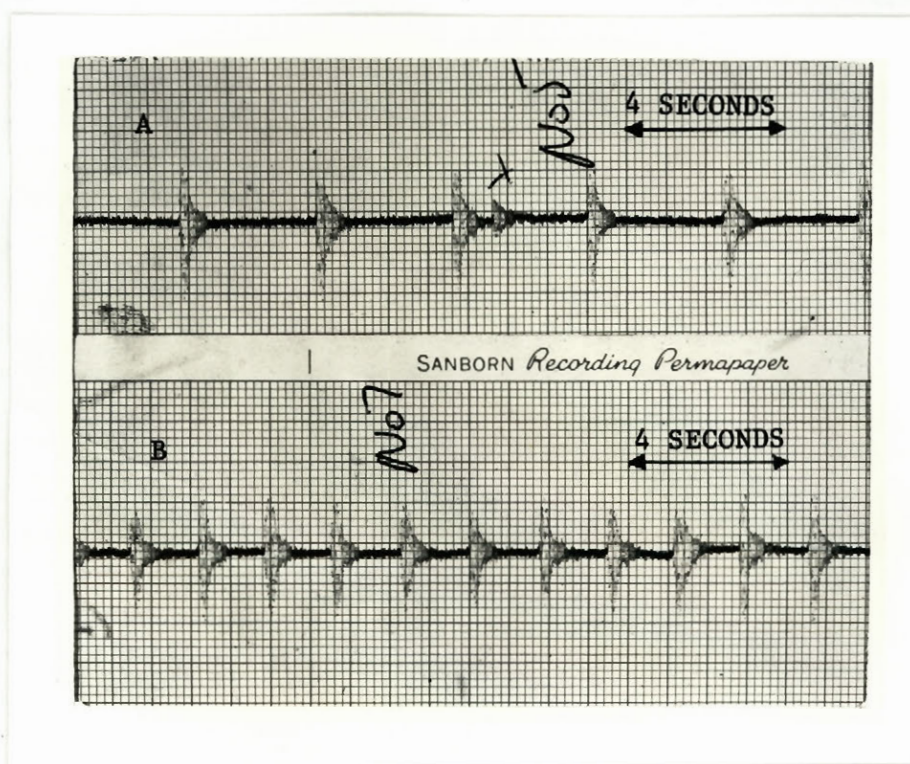


FIGURE 8. Strip-chart traces of bubbles, obtained electronically, nozzle outside diameter, 2.54 cm; inside diameter, 0.635 cm; chamber volume, 342 cm³; chart speed, 5 cm s⁻¹; μ V/vertical division, 100.

A: flow rate, 2.78 cm³s⁻¹; f, 0.294 s⁻¹; bubble volume, 9.45 cm³

B: flow rate, 5.51 cm³s⁻¹; f, 0.586 s⁻¹; bubble volume, 9.40 cm³

Note: Bubble marked with "X" is a pair.

Table I also shows that the average oxygen content was 16 ppm, which is considerably in excess of the 3.5 ppm value at equilibrium.²⁰ However, it was found that 20 minutes of vigorous argon degassing eliminated bubble nucleation at the lance/nozzle junction, so it is not expected that carbon monoxide or any other dissolved gas had a significant effect on the argon bubble volumes. The sulphur contents were quite variable from run to run (7.8 to 119 ppm), as shown in Table I, while within each run they were generally quite constant. These variations are due to differences in the iron charge and graphite chips (which contained some sulphur).

The results have been summarized in Figures 9 to 15. Following normal practice, the bubble size was expressed as an equivalent diameter, that is, the diameter of a sphere of the same volume as the bubble. Both the equivalent diameter, D_e and bubble volume, V_b , were plotted as a function of the flow rate, Q . These three variables were corrected to the bath temperature, 1523 K. The symbols represent the various chamber volumes, which in turn were converted to capacitance numbers, N'_c (calculated using Equation (16)). For the reader's convenience the same symbol in Figures 9 to 15 corresponds to the same chamber volume, namely, X for 2192 and 2242, 0 for 1175, Δ for 615, \square for 343 and + for 23 to 33 cm³. The curves for each chamber volume were obtained from Equation (23) with $m = 0.816$ (except in Figure 14 in which $m = 1.0$). This parameter, m , is the capacitance dependency, which is discussed later.

DISCUSSION

Description of High Temperature Results

Figure 9 contains the results obtained with the largest lance, which had an outside diameter, D_{no} of 5.08 cm and an inside diameter, D_{ni} , of 0.635 cm. It can be seen that increasing the chamber volume from 23 to 2242 cm^3 was responsible for a 30-fold increase in bubble volume. In addition, there was considerable scatter in the small chamber volume results which were all below their corresponding curve. The next plot, Figure 10, demonstrates the effect of halving the outer diameter of the nozzle. At low flow rates, with a small chamber volume, the bubble volumes were quite close to the 0.503 capacitance curve, meaning that the bubbles were formed at the outer diameter. There were also some bubbles of approximately 1 cm^3 . At higher flow rates, in the constant frequency regime, the data fitted the curve very well, but one can see that the data fell within the same band as in the previous diagram. Referring again to Figure 10, it is apparent that increasing the chamber volume increased the bubble size in reasonable agreement with the curves. For the largest chamber volumes in both Figures 9 and 10 (2242 cm^3), the bubble volumes were both approximately 50 cm^3 . This is functionally consistent with Equation (10), in which D_{no} does not appear. Most of these large bubbles were "pairs" which were described earlier. In several instances the pairs could not be distinguished from two bubbles each of half the volume; for example, as seen in Figure 10, chamber volumes of 2242 cm^3 produced both 50 and 25 cm^3 bubbles. At the higher flow rates the fitted curves were considerably below the experimental results.

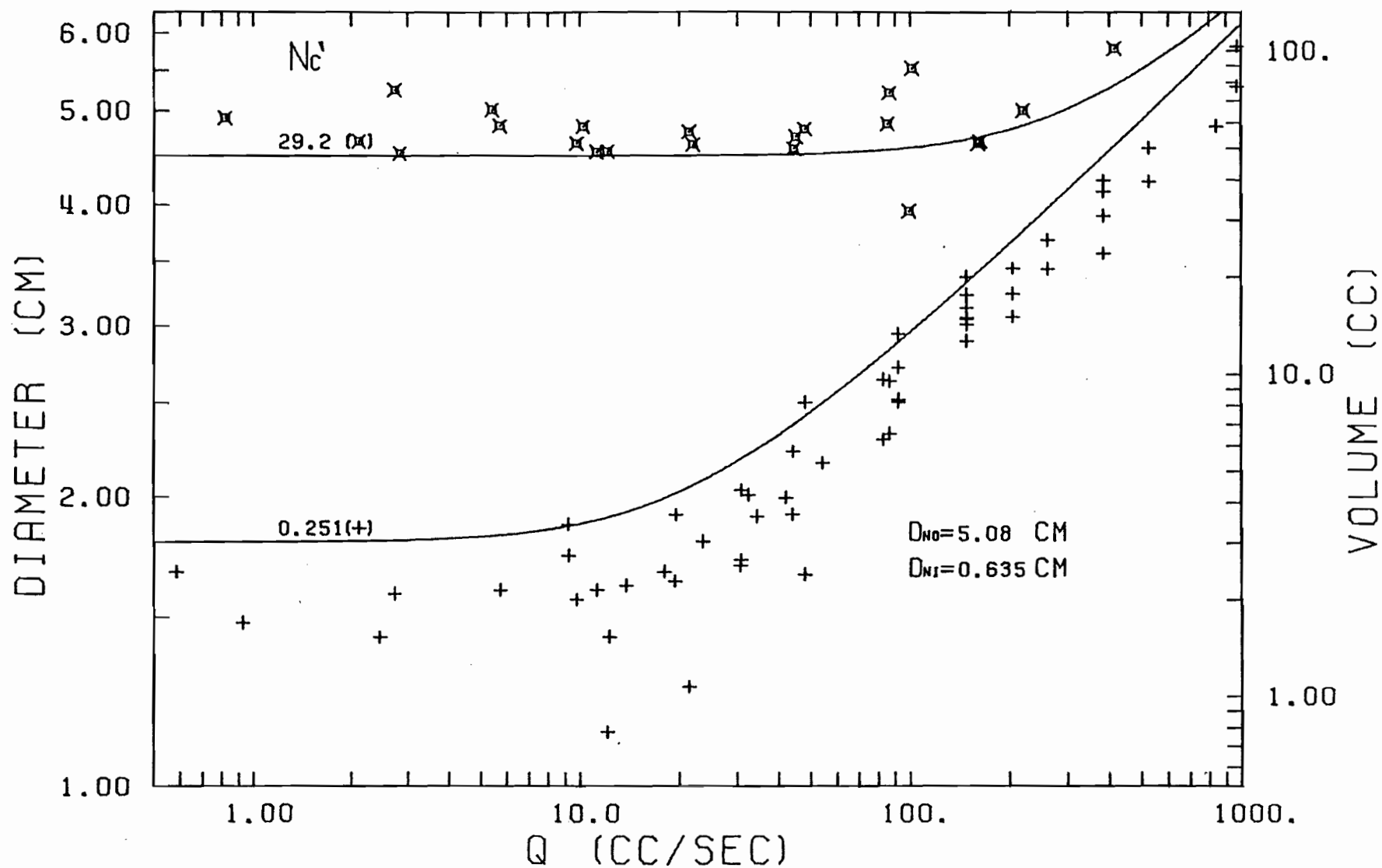


FIGURE 9. Bubble volume and equivalent diameter as a function of flow rate, at 1523 K, for an outside nozzle diameter of 5.08 cm and inside diameter of 0.635 cm.

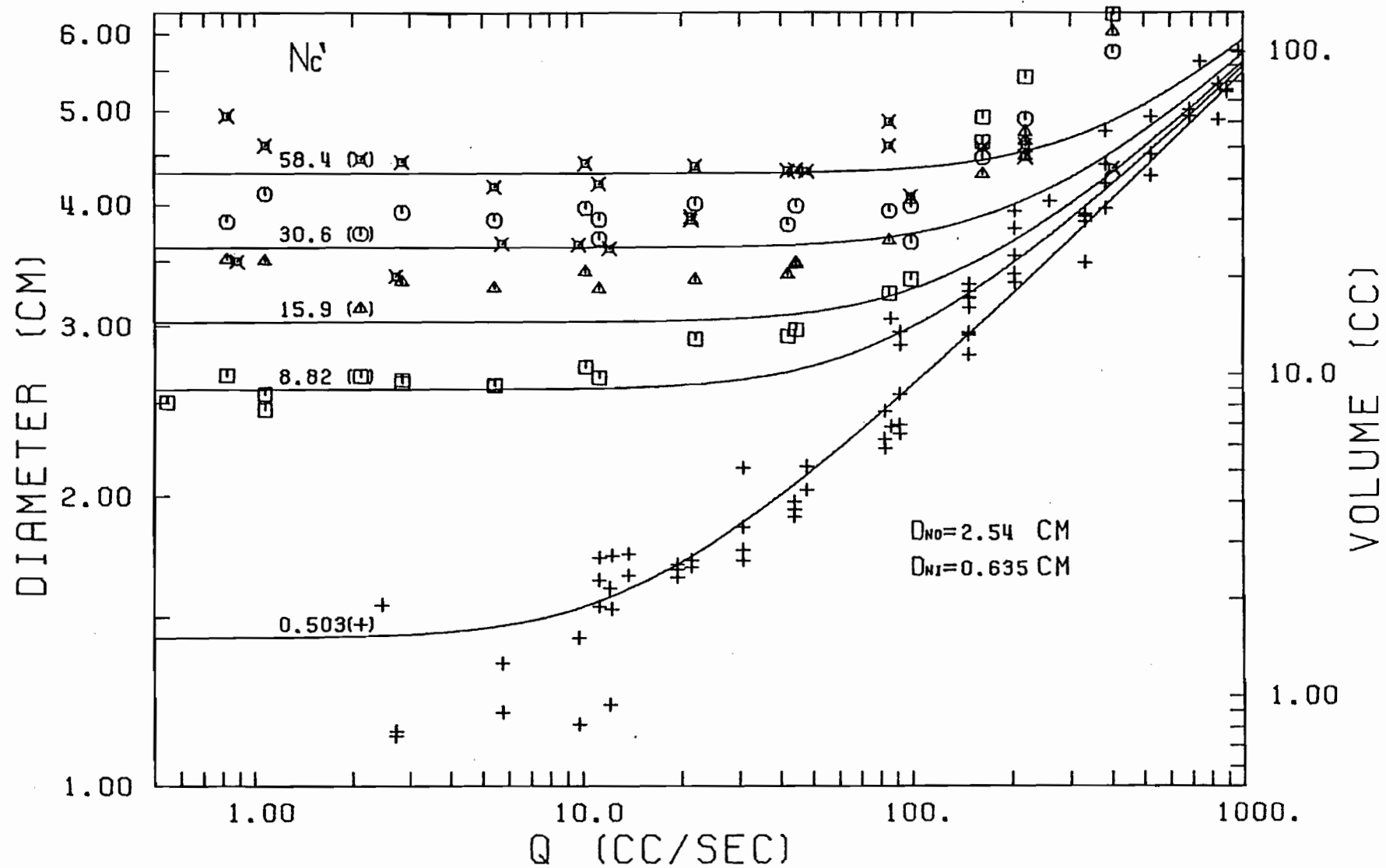


FIGURE 10. Bubble volume and equivalent diameter as a function of flow rate, at 1523 K, for an outside nozzle diameter of 2.54 cm and inside diameter of 0.635 cm.

Examination of Figure 11 reveals that halving the inside diameter almost doubled the bubble volume for the larger chamber volumes. Again this is in substantial agreement with Equation (10). The results for the smallest chamber volume were almost the same as in the previous figure, which is expected if the bubbles form at the outer diameter in accordance with Equation (2).

The next two Figures, 12 and 13, contain the results for nozzles of 1.27 cm outside diameter and two inside diameters, 0.635 and 0.318 cm, respectively. With nozzle sizes reported in Figure 12 at small flow rates and capacitances, bubbles were of about twice the volume (2 cm^3) of bubbles forming at the outer diameter. In contrast to this, in the previous figures bubble volumes equal to and one-half that predicted by Equation (2) were obtained. In the constant frequency regime of Figures 12 and 13 the data fell within the same band as in the previous figures.

Mori and co-workers^{4,21} were able to demonstrate that an empirical correlation developed by Davidson and Amick¹³ for aqueous systems

$$V_b = 0.083 Q^{0.867} D_{ni}^{0.435} \quad (20)$$

could describe their results at higher flow rates in mercury and silver if D_{ni} were replaced by D_{no} . As a consequence, the constant frequency curves should have been displaced upwards as the outer diameter was increased. However, this was not observed in the present study for nozzles between 1.27 and 5.08 cm outside diameter. A smaller nozzle,

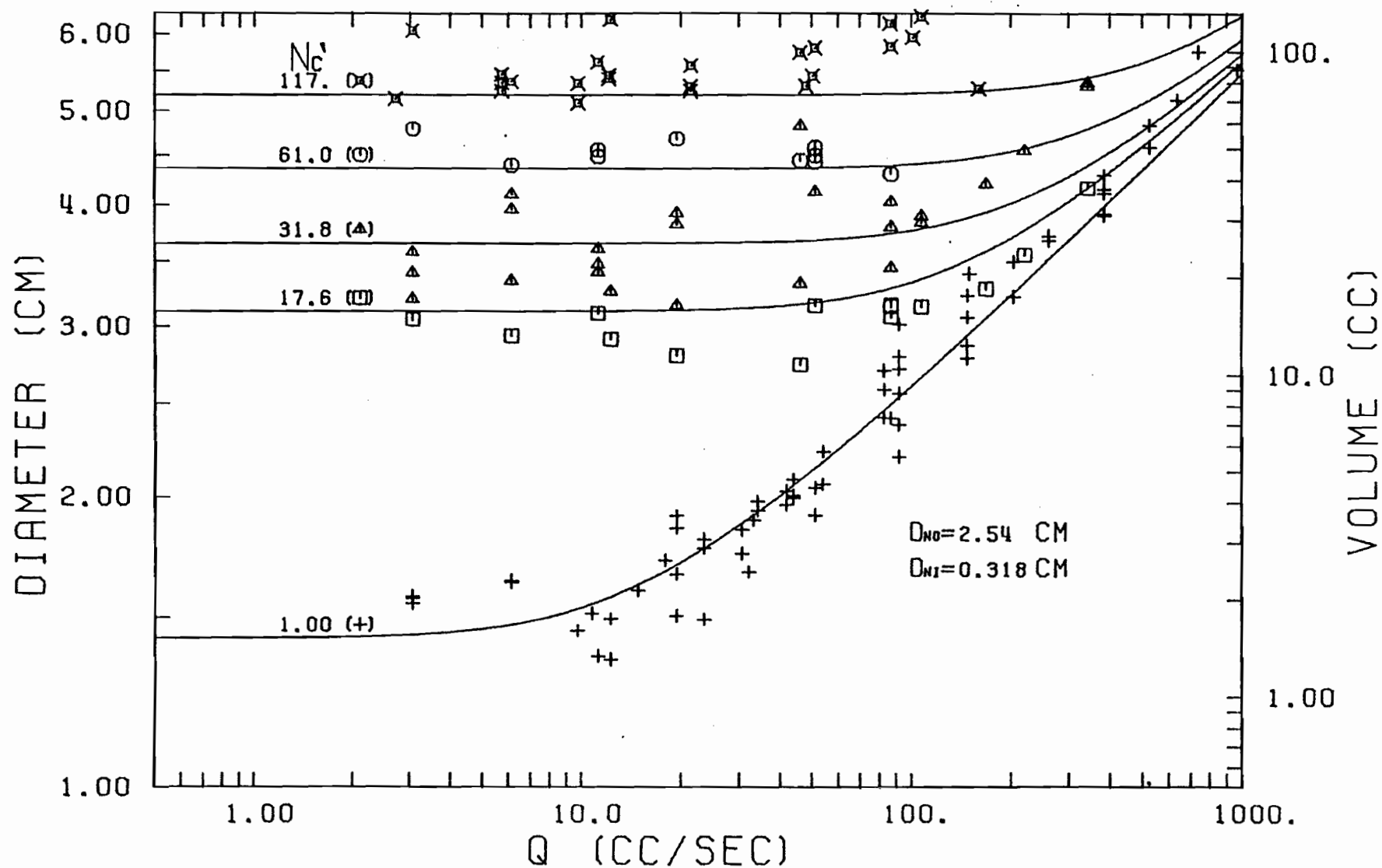


FIGURE 11. Bubble volume and equivalent diameter as a function of flow rate, at 1523 K, for an outside nozzle diameter of 2.54 cm and inside diameter of 0.318 cm.

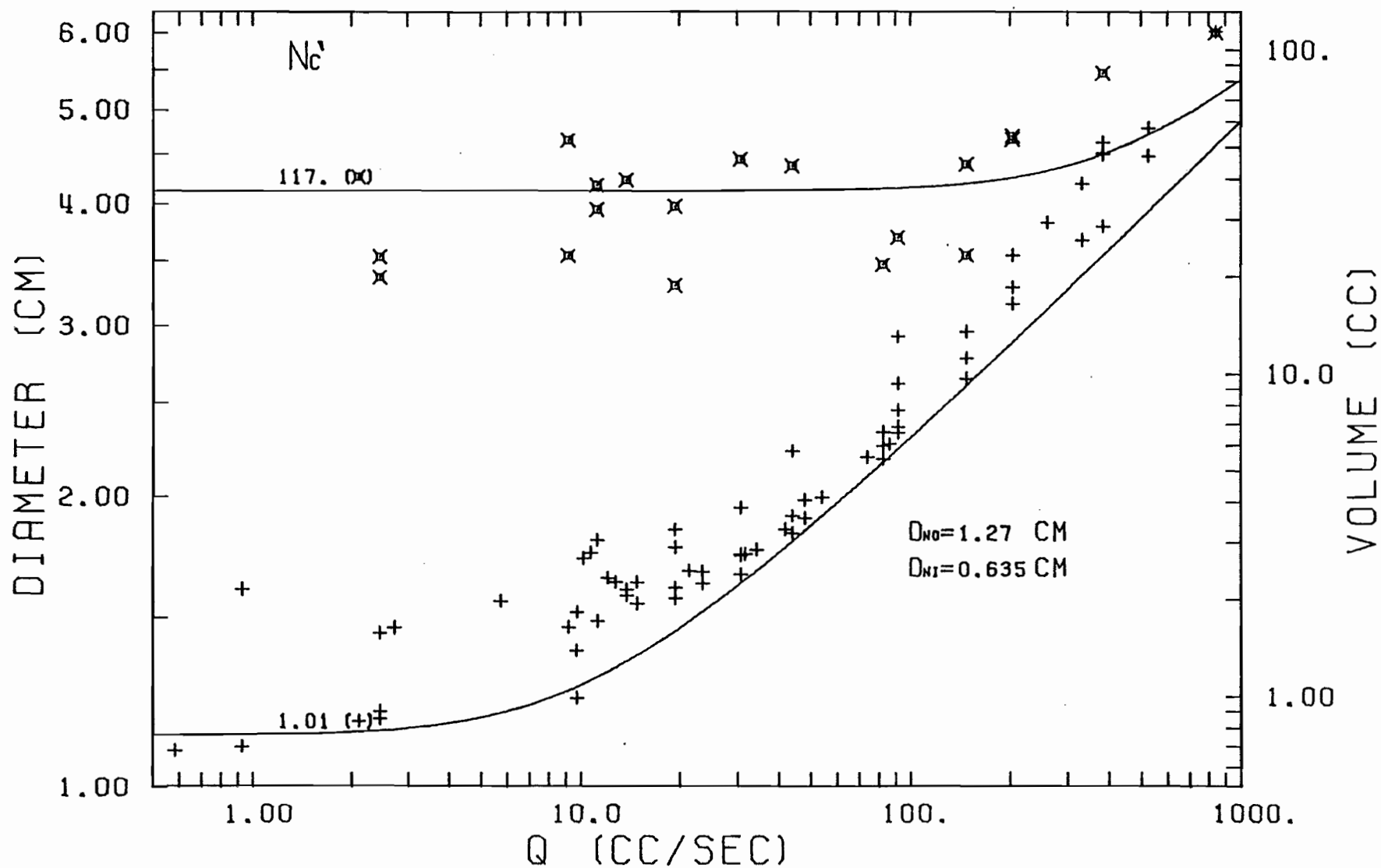


FIGURE 12. Bubble volume and equivalent diameter as a function of flow rate, at 1523 K, for an outside nozzle diameter of 1.27 cm and inside diameter of 0.635 cm.

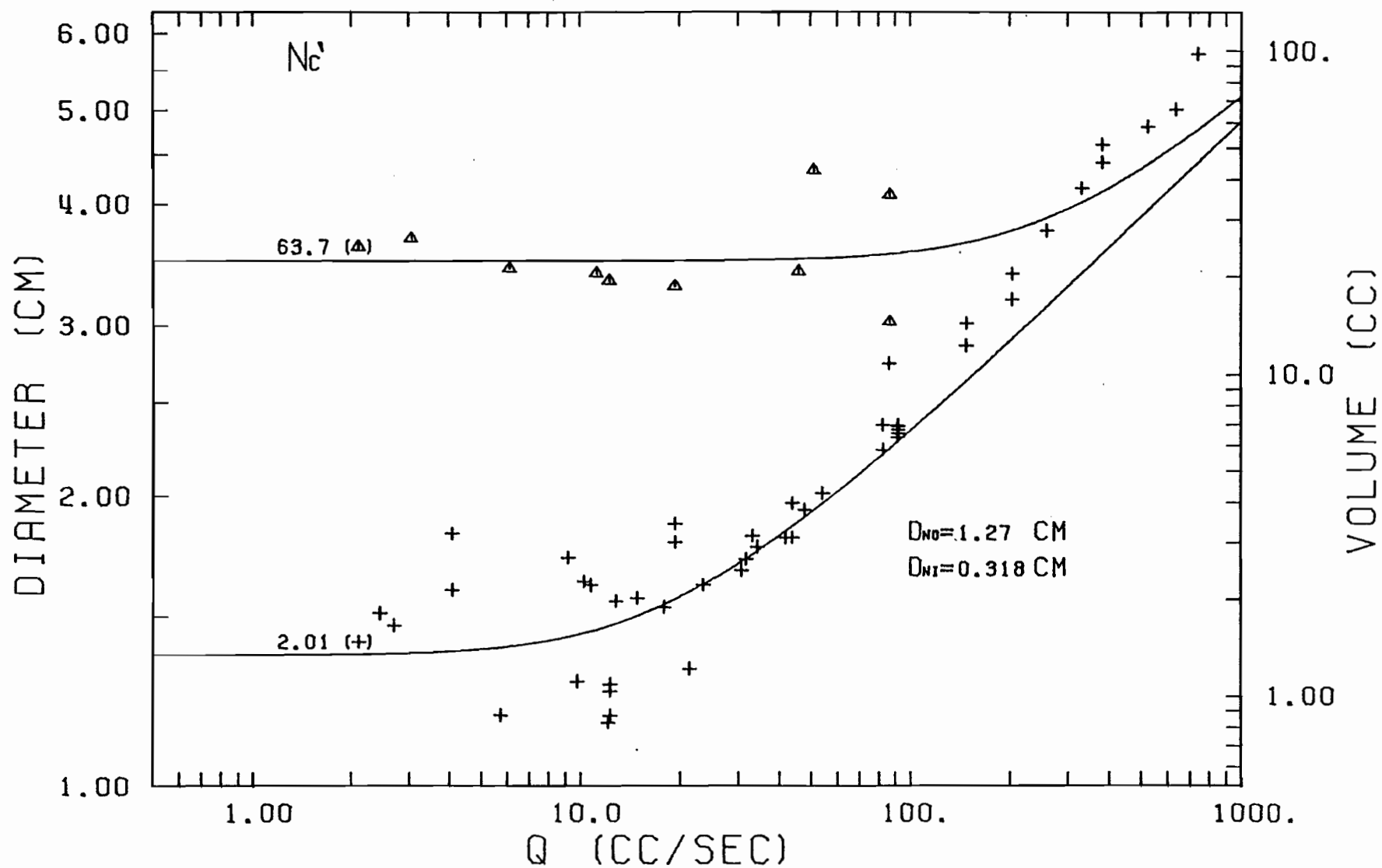


FIGURE 13. Bubble volume and equivalent diameter as a function of flow rate, at 1523 K, for an outside nozzle diameter of 1.27 cm and inside diameter of 0.318 cm.

0.635 cm, was used in order to duplicate the conditions of Mori et al. (Figure 14). Unfortunately, geometrical constraints precluded capacitance numbers less than 8. Nevertheless the bubbles for gas flows up to $100 \text{ cm}^3 \text{ s}^{-1}$ were smaller than in the previous figures and were in reasonable agreement with the curve predicting a square root dependency on the outside diameter. At higher flow rates the bubbles became much larger. The significance of these results is discussed later.

Nozzle Orientation

Nozzle orientation was also investigated and the results are summarized in Figure 15, for a constant chamber volume and inside and outside nozzle diameters. As can be observed, the bubble volumes for upward-and sideways-facing nozzles were almost the same. In contrast to this, the downward-facing nozzles produced bubbles about 10 times smaller in volume, and seemed to behave as though the capacitance number were less than or equal to one. It therefore seems likely that the mechanism of bubble formation is somewhat different as discussed later. It should be noted that Mori and co-workers^{3,4,21} used only upward-facing nozzles, while the present work was conducted mainly with sideways-facing nozzles.

Surface Tension Effects

The results presented in the previous graphs were all obtained in baths in which the sulphur content varied between 8 and 120 ppm (Table I). The surface tension of high carbon melts at 1523 K was estimated from the relationship^{22,23}

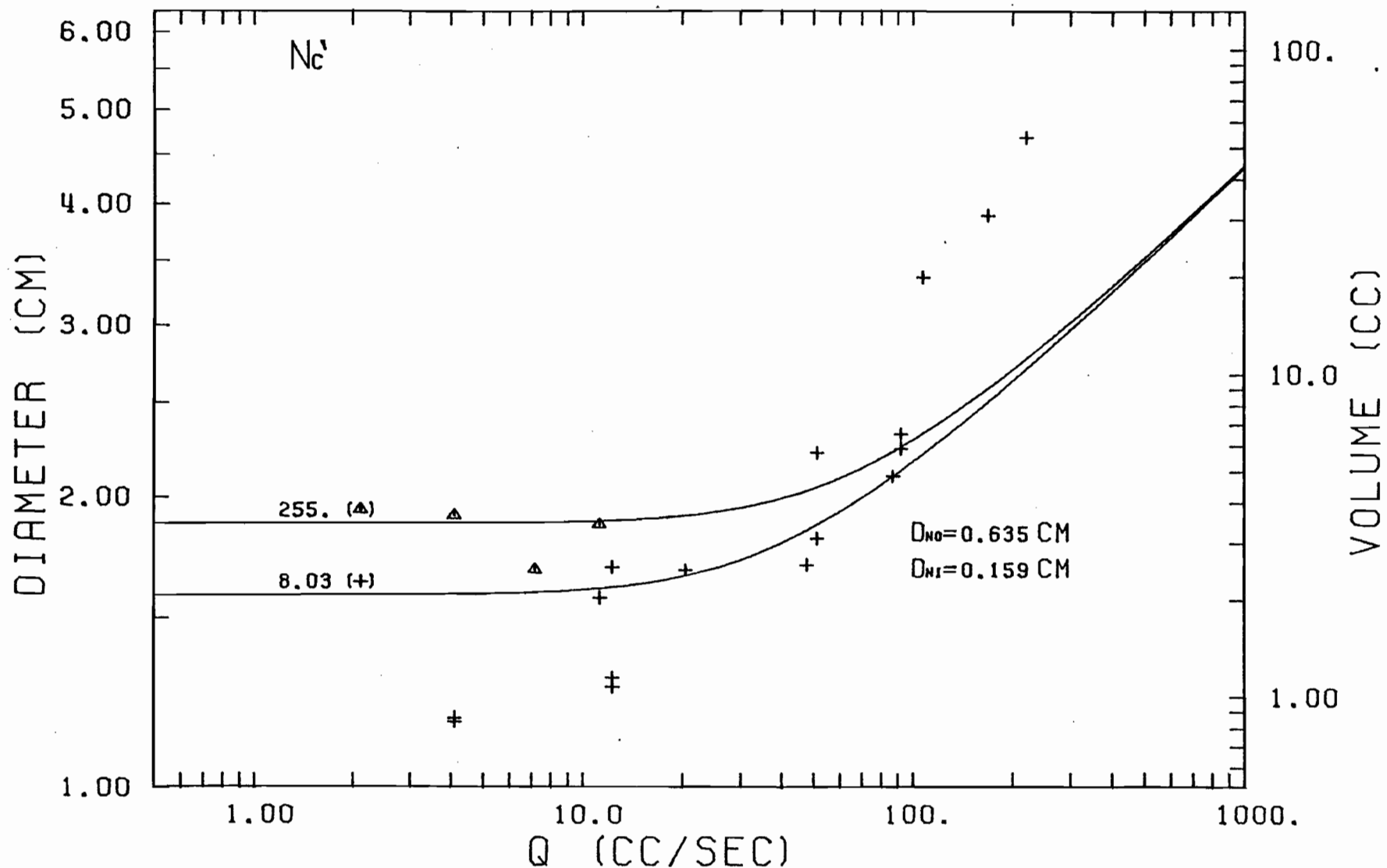


FIGURE 14. Bubble volume and equivalent diameter as a function of flow rate, at 1523 K, for an outside nozzle diameter of 0.635 cm and inside diameter of 0.159 cm.

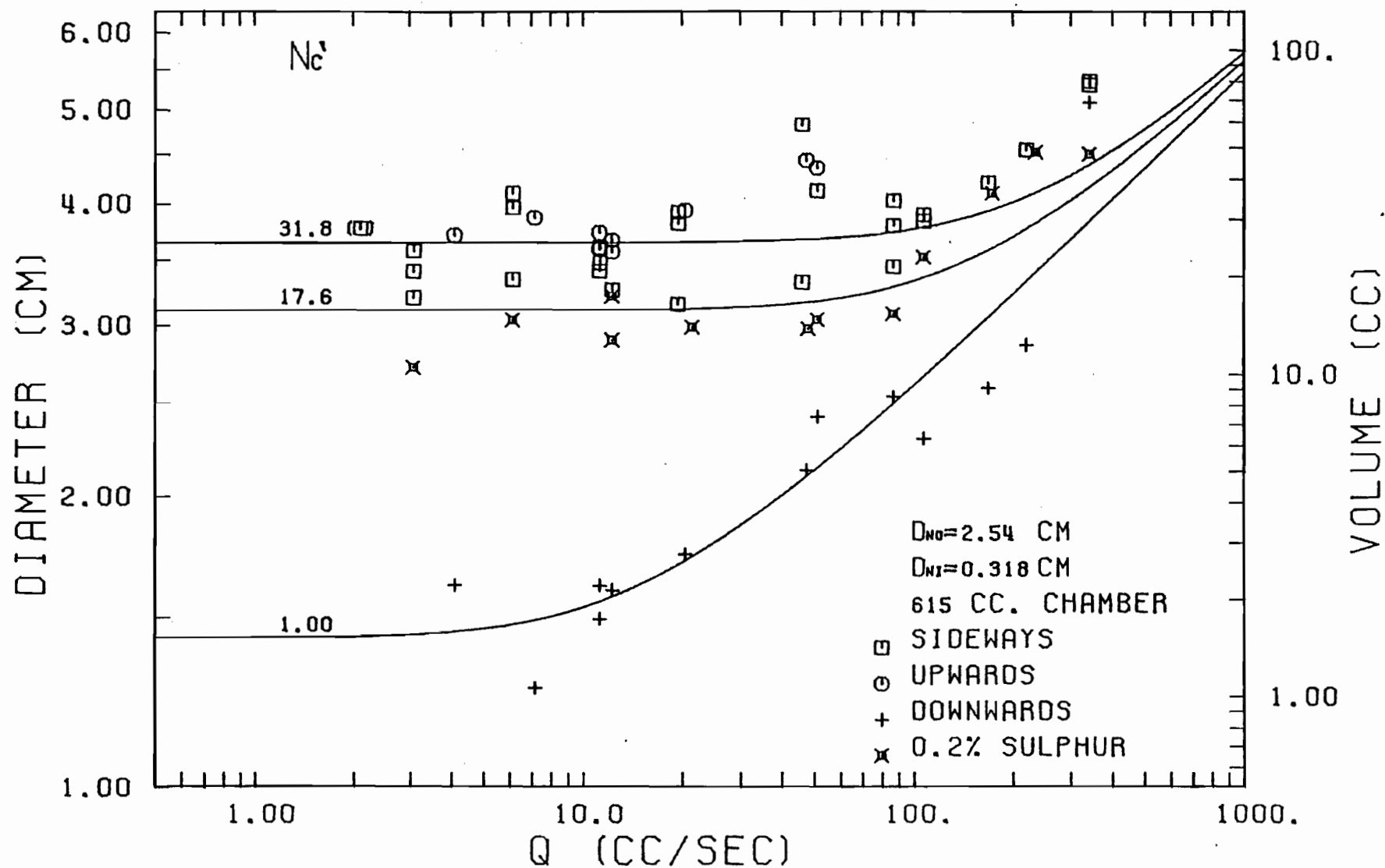


FIGURE 15. Bubble volume and equivalent diameter as a function of flow rate, at 1523 K, for an outside nozzle diameter of 2.54 cm, an inside diameter of 0.318 cm and a chamber volume of 615 cm³. The nozzle orientation is varied as indicated and for 1 set of data the sulphur content was 0.2%.

$$\sigma = 1732 - 163 \ln(1 + (1220.\% C - 2650.)\% S) \text{ dyne.cm}^{-1} \quad (21)$$

The range of the estimated surface tensions (1550 to 1180 dyne.cm⁻¹), was not wide enough to detect any statistical difference in bubble size. However, the addition of the ferrous sulphide in run 8 (Table I) lowered the predicted surface tension to 680 dyne.cm⁻¹. The bubble volumes then produced (Figure 15) were reduced in the same ratio as was the surface tension, as predicted by Equation (2). (The bubbles behaved as though the capacitance had been reduced to 17.6.)

Discussion of X-Ray Results

Because of the poor resolution of the X-ray equipment for this specific purpose, a mass balance between the gas flow rate and the product of the visually observed bubble volumes and frequencies could only account for 50% of the flow rate. Therefore a quantitative X-ray study was not possible. Nevertheless, most bubbles could be quite clearly seen on the nozzle, particularly on the movies. In Figure 16A, the bubble appeared to form at the outer diameter of the nozzle. This was direct confirmation of the validity of Equation (2), which describes the results of Sano and Mori^{3,4} and the present ones in iron. However, it was more usual to observe the bubbles to be positioned on the upper portion of the nozzle, as shown in Figure 16B. It appeared that the edge of the nozzle did not provide a significant restraint to the bubble. These bubbles were at least 1 cm³ in volume, for which the buoyancy forces were large enough to push the bubble around the corner, and hence to exceed the second limit of the Gibbs' Inequality.⁷ However, the overall force balance (mainly between buoyancy and surface tension, ignoring

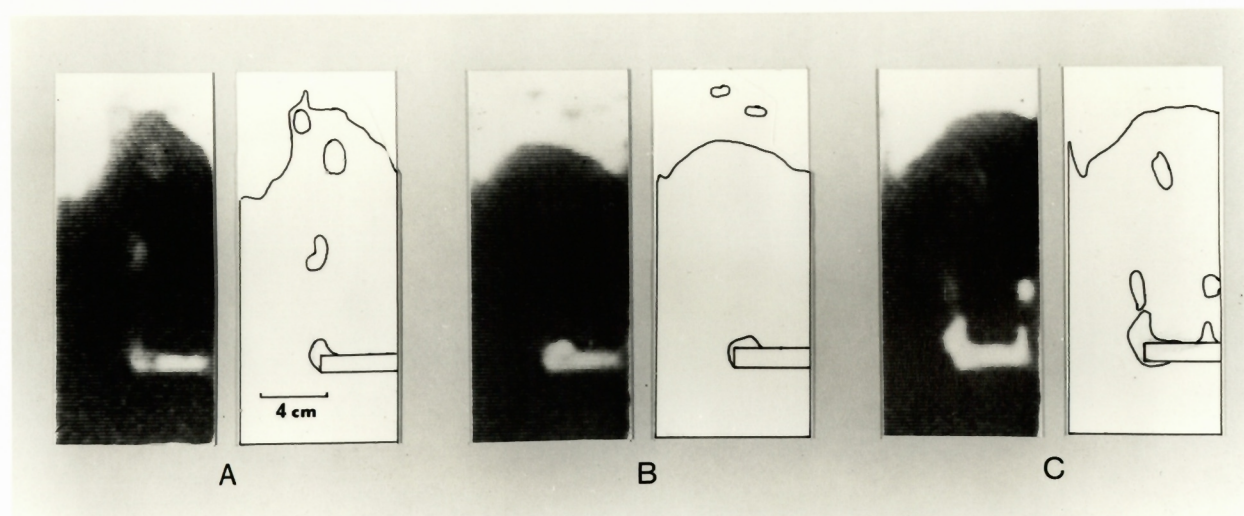


FIGURE 16. X-ray photographs of gas injection into the indium-gallium melt, accompanied by tracings for the sake of clarity. Note the horizontal nozzle with attached bubbles and the free surface of the melt. (A) shows bubble formation at the outer diameter of the nozzle. The gas flow rate was $22 \text{ cm}^3\text{s}^{-1}$, and the X-ray unit was operated at 100 kV and 2 mA. (B) shows bubble formation on the upper part of the nozzle under the same conditions as (A). (C) shows movement of the bubbles back along the top of the nozzle. The gas flow rate was $63 \text{ cm}^3\text{s}^{-1}$, and the power was 100 kV at 2 mA.

inertial effects) would have held the bubble on the nozzle until V_{bm} was reached. The line of contact was only slightly larger than the circumference of the nozzle.

At somewhat higher flow rates, for example, $63 \text{ cm}^3\text{s}^{-1}$, it was observed that the bubbles would often adhere to and move back horizontally along the top of the nozzle, instead of rising vertically from the end face. This is shown in Figure 16C. Again, the non-wettability of the nozzle material was likely responsible for this phenomenon. The motion of the liquid at these higher flow rates may have been the cause of bubble movement along the top of the nozzle. Oryall and Brimacombe²⁴ used an electrical probe to measure gas distribution and bubble frequency in a jet of air injected horizontally into a mercury bath at high flow rate. They found that the gas penetrated well behind the nozzles, in marked contrast to aqueous systems in which the gas was projected much further forward into the melt. This observation could be explained by the adhesion and movement of some of the bubbles back along the nozzle before release.

Sources of Experimental Error

No statistical difference between results collected under identical conditions could be determined. Similarly, there was no difference between bubble sizes at nozzle depths of 7.6 and 19.8 cm when small chamber volumes were used.

The efficacy of the frequency measurement method was tested in water, where one spike on the strip-chart paper was seen to correspond to the release of a bubble. This was observed up to approximately 10 bubbles/second. At low flow rates in pig iron, a vibration

could be felt by hand on the bar and seen on the paper an instant before the bubble broke through the surface. This was further proof that the vibrations were produced by bubble release.

The most puzzling aspect of the present work was the considerable amount of random error in the results, particularly for the small chamber volume work. It was unlikely that errors in measuring the flow rate were responsible for this because the flow meters were calibrated. The absolute error could not have been greater than $\pm 3\%$. On the other hand, the frequency measurements could not be subjected to independent verification at higher frequencies. Furthermore, above a flow rate of $100 \text{ cm}^3 \text{ s}^{-1}$ the bubbling became irregular, but representative traces were obtained. Typically 40 bubbles were counted, and if two bubbles had been missed the percentage error would have been 5%. Coupling this with the error in flow rate would have yielded at most a $\pm 8\%$ error in volume. However, one can see that the scatter at higher flow rates, particularly with small chamber volumes, can be $\pm 50\%$. There was generally less random error ($\sim \pm 25\%$) in the results obtained at lower flow rates. At the highest flow rates there was severe turbulence and splashing of metal. Ignoring inertial effects, one can show that changes in ferrostatic pressure were sufficient to release a bubble. For a typical case, the pressure due to surface tension was about $1.6 \times 10^4 \text{ dyne/cm}^2$ (Equation (7)), or equivalent to a 2.4 cm change in head. As fluctuations in the bath surface greater than this were observed, this could have accounted for some of the random error. Davidson and Amick¹³ determined that the measured bubble volumes were doubled if the bubbles coalesced at the orifice. This was also a possibility in the present work.

The large amount of random error could also have been due to the fact that the bubbles probably spread back along the top of the nozzles, as they did in the indium-gallium alloy. The pattern of bubble release was quite random in this latter work, and this would have affected the size of the bubbles. Sano and Mori did not report this random error with their smaller upward-facing nozzles, and also were able to determine the dependence of the frequency on the outer diameter.

While most measurements were obtained with the induction power on, several were taken with it off. The difference in volume was only $\pm 10\%$, which demonstrated the small effect induction stirring had on bubble formation.

The melt temperature was closely controlled to 1523 ± 15 K to prevent precipitation of graphite. Although the results presently reported were obtained above the liquidus temperature, a cooler bath characteristically produced much smaller bubbles and was noticeably more viscous. Such behaviour has interesting implications for gas injection processes carried out at or below the liquidus. This would apply to most blast furnace hot metal desulphurization practices.

The experimental flow rates and bubble volumes have all been quoted at the bath temperature, 1523 K. However, a simple estimate of the heating rate in the lance and nozzle, using convective heat transfer coefficients²⁵, showed that this was accurate up to $80 \text{ cm}^3 \text{ s}^{-1}$ at 1523 K. Therefore at flow rates higher than this, the actual bubble volume released was smaller than reported. Heat transfer to the bubble during formation would have tended to counteract this trend.

Capacitance Effects

The effect of capacitance can be visualized more clearly in Figure 17 which is a "cross-plot" of the average bubble sizes in the constant volume regions (the flow rate-independent regimes of Figures 9 to 14) against N'_C . For capacitances less than one, the bubble size should have been independent of capacitance. Furthermore, the bubble volume should have been predicted by Equation (2), and experimental results were in reasonable agreement with this. However, one must note that bubbles having one-half the volume were also reported. They were not doublets described in Figure 3 because they occurred at low flow rate and were smaller than the singles. Their mode of formation was uncertain, but it may be that the preferential spreading to the upper half of the nozzle, as observed in the X-ray work, caused the bubbles to be released from the upper half of the nozzle. Further, the bubbles from a 5.08 cm outside diameter nozzle were smaller than predicted. This latter observation indicated that the bubbles did not form at the outer diameter for nozzles much larger than 2.54 cm for small capacitances. This delineates the transition from nozzles to orifices, which occurs when the outside diameter has no further effect. (A nozzle is a tube projecting into the liquid and has an outside diameter, whereas an orifice is simply an opening in a large plate.)

For larger capacitances, the data in Figure 17 exhibited two types of behaviour. The lowest curve represents Sano and Mori's⁴ equations for a non-wetting system ((12), (13) and (14)). They appear to apply for the smallest orifice, which was in fact chosen to verify Sano and Mori's results. At $N'_C = 8$, doublet formation was observed, which was not reported by Sano and Mori.

The larger orifices behaved differently, producing much larger bubbles, which were for the most part "pairs". The dependence on N'_c was not quite as strong as in the other case. The dependency was established to be:

$$\frac{V_b}{V_{bm}} = N'_c{}^{0.816} \quad (22)$$

by statistical regression. One can see that the regression fits the data well, despite the considerable random scatter. The regression was highly significant, having low standard errors of the regression coefficient and of the estimate (0.009 and 0.159, respectively) and a high F-statistic (10200.) for the 142 points used in the regression.

Most of the bubbles in the large capacitance regime were pairs, however at low flow rates they were sometimes single bubbles. The flow rate at which this transition was observed from the traces appears beside each point in Figure 17. The only significant trend was that at larger capacitances and bubble volumes the transition occurred at lower flow rates. This method was not very satisfactory because the trace of the second bubble could have been indistinguishable from that of the first one, and because above $100 \text{ cm}^3 \text{ s}^{-1}$ the spikes of the traces became irregular.

The two distinctive behaviours of the bubbles at high capacitances in Figure 17 can be understood by considering Figure 18 which is the same type of diagram. In this case, representative data from four studies were plotted. For the water studies^{2,13} the capacitance was defined in Equation (11), while for the metallic studies Equations (15) and (16) were used. The results of Tadaki and Maeda² closely

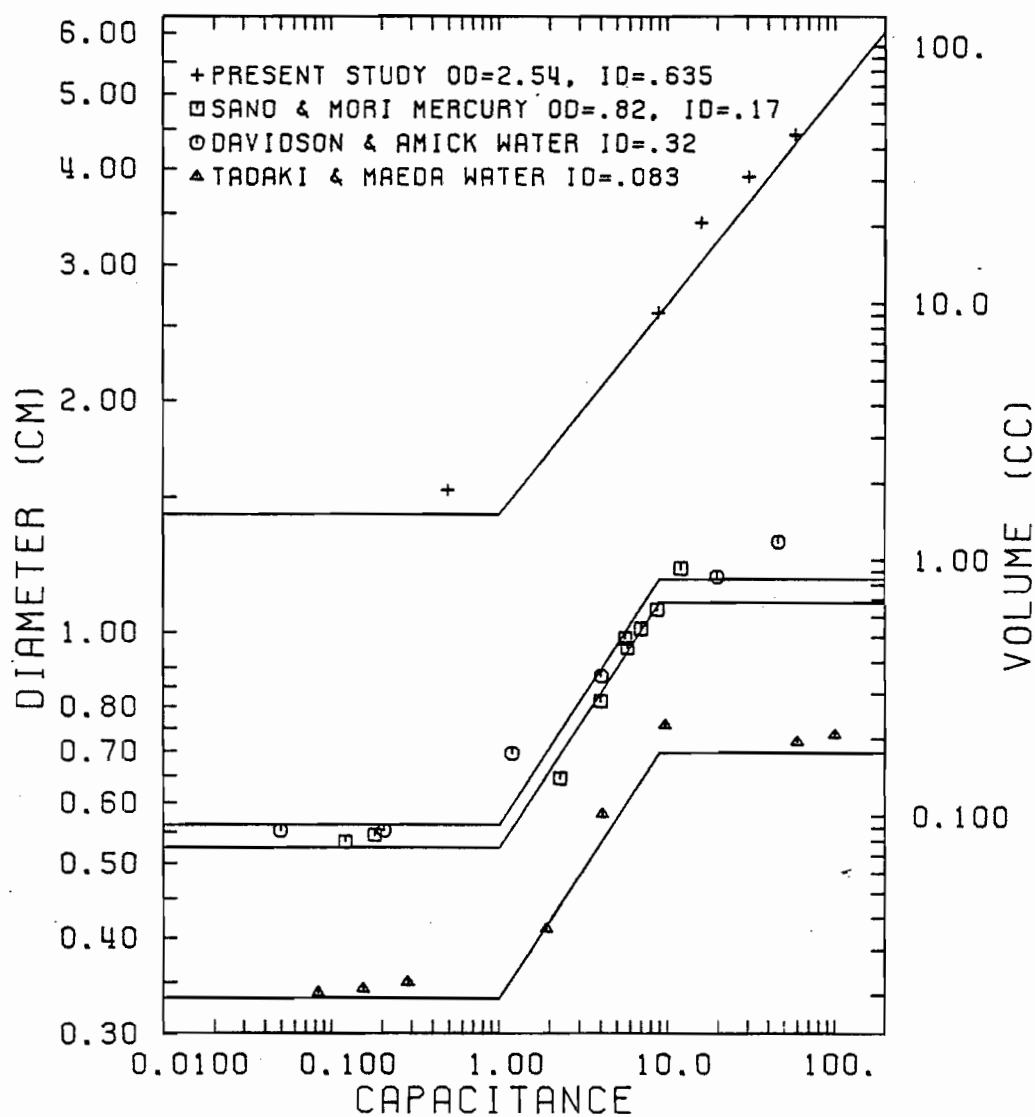


FIGURE 18. Bubble volume and equivalent diameter as a function of capacitance for the present study and others (References 2, 4 and 13). The capacitances were calculated by Equations (11) and (16) for the water and metallic studies, respectively.

followed the predicted lines (which they developed); however, Davidson and Amick¹³ found that the bubble size continued to increase with capacitances greater than 9. At a capacitance of 46 the bubble volume was 1.18 cm^3 , some 72% larger than predicted by the curve. This discrepancy could be attributed directly to the experimental technique of bubble counting. Tadaki and Maeda² used a photographic technique in which they measured the diameter of each bubble, even if they were pairs. On the other hand, Davidson and Amick¹³ also photographed bubbles but they considered the total volume of a pair. Consequently, the pair volume would continue to increase, even though that of each individual bubble might not have. This latter method was equivalent to the present method and also to that of Sano and Mori.⁴ However, the latter authors did not exceed a capacitance of 12.

Several factors may have accounted for the exponent of the capacitance number being 0.816 rather than unity. Firstly, the pressure change in the antechamber during bubble release may not have been completely isothermal and instantaneous. As demonstrated in the theory section, adiabatic expansion would have resulted in smaller bubbles. Graphically, it would have reduced the bubble volumes by a factor of γ in Figure 17. Further, one can speculate that small bubbles are formed isothermally, while larger ones tend to form under more adiabatic conditions.

Additionally, if the contact angle had been greater than that assumed for Equation (16), (90°), then the actual bubble sizes would have been smaller than predicted by this equation.

Finally, if there had been some gas remaining on the nozzle following release, this would have decreased the observed bubble sizes

below those predicted. Conversely, if liquid had penetrated back into the nozzle, the bubbles would have been larger than predicted.

Mechanism of Bubble Formation

On the basis of the experimental results, it is possible to suggest the consecutive steps of bubble formation at nozzles in liquid metals.

Let us consider first of all a sideways-pointing nozzle of reasonably large dimensions ($0.5 \lesssim D_{no} \lesssim 2.0$ cm), at low gas flow rate (Figure 19A). Initially, the bubble forms on the inner diameter, increasing in size towards a hemisphere. However, the equilibrium contact angle between the bubble and the nozzle face is reached before a hemisphere is formed (unless $\theta_0 \leq 90^\circ$). This corresponds to the second limit of the Gibbs' Inequality at the inner edge, so the bubble must spread across the nozzle face for continued growth.* As the volume is increased, the bubble spreads with the equilibrium contact angle or the advancing contact angle if contact angle hysteresis⁶ occurs. When the bubble reaches the outer diameter it spreads around the corner as shown in Figure 19A, because the buoyancy forces are more significant than the constraints imposed by the Gibbs' Inequality. (Presumably, for smaller nozzles and bubbles, the Gibbs' Inequality would operate as it did in the previous study of drops.⁸) The line of contact between the bubble and the nozzle at release is similar to the circumference of the nozzle, as was observed in the X-ray work, so that the criterion

* Sano and Mori^{3,4} recognized this upper limit on bubble volume and pressure at the inner diameter in their development of N'_C , the capacitance number.

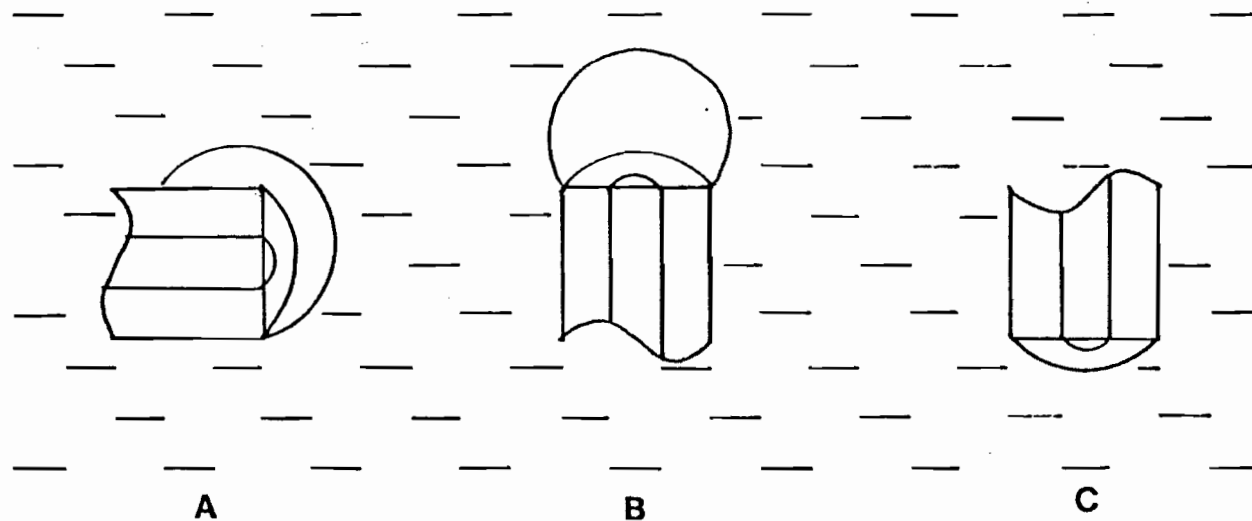


FIGURE 19. Schematic representation of the consecutive steps of bubble formation at nozzles with the three principal orientations in a liquid metal at low gas flow rate. See text for the explanation.

for bubble release is still reasonably well predicted by Equation (2).

For an upward-facing nozzle (Figure 19B), under the same conditions, the same initial steps are envisioned. However, when the bubble reaches the outside diameter, it continues to grow by changing the observed contact angle, in accordance with the Gibbs' Inequality. It does not spread down the nozzle since the considerable buoyancy forces oppose such movement. Generally, the buoyancy of the bubble causes release (Equation (2)) before the second limit of the Gibbs' Inequality is reached (Equation (4)). The buoyancy forces tend to elongate the bubbles in the vertical direction in contrast to the spheres depicted in Figure 19B.

On downward-facing nozzles, the bubbles also spread to the outer diameter (Figure 19C) with the equilibrium contact angle. For these relatively large bubbles, the buoyancy forces are greater than the constraining forces, so that the bubbles escape up the side of the nozzle when they reach the outer diameter. The contact angle for the present iron-carbon alloy is probably between 90° and 130° .^{26,27} From Equation (4), volumes of bubbles with these contact angles on 2.54 cm nozzles are 4.29 and 1.61 cm³, respectively. The experimentally observed bubble volumes for such nozzles were approximately 2 cm³ (Figure 15). Since the contact angle is close to 90° , it is not clear whether the release criterion is the hemisphere volume, or that obtained from Equation (4). Nevertheless, this provides a reasonable explanation for why bubbles at downward-facing nozzles are so much smaller.

Now considering upward- and sideways-facing nozzles of different sizes as shown in Figure 20, the same reasoning can be applied. For very

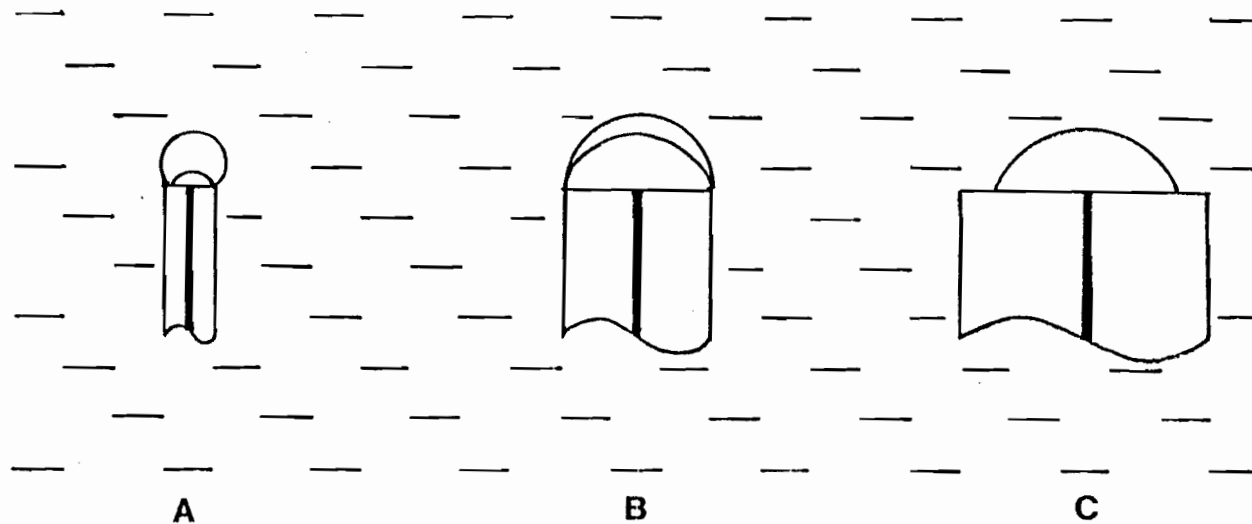


FIGURE 20. Schematic representation of bubble formation at nozzles of various size in a liquid metal. The bubble volumes from Equations (2) and (4) are shown. See text for further explanation.

small nozzles, illustrated in Figure 20A, V_{bm} is much greater than that of Equation (4) for the equilibrium contact angle, so the bubbles grow until buoyancy is satisfied. As the diameter is increased, the difference between these two volumes decreases (Figure 20B). At even larger diameters, buoyancy forces overcome the bubble before it reaches the outer diameter (Figure 20C). This transition diameter can be found by equating Equations (2) and (4) (if buoyancy shape distortions are neglected). For the probable limits of the contact angle, 90° and 130° , the transition should occur between 1.51 and 2.46 cm, respectively. With small chamber volumes, it was found that bubbles at 2.54 and 5.08 cm diameter nozzles were the same size (Figure 17), which is close to the theoretical transition diameter. As mentioned earlier, this represents the transition from nozzles to orifices. For larger chamber volumes ($N'_c > 1$), this effect must be considered in conjunction with the surge of gas that is compressed during formation. This makes the bubbles much larger.

At higher flow rates, the force balance is more complicated and is generally evaluated as a function of time, so that the solutions are often not analytical. From the present work, however, there does appear to be a general transition from nozzles to orifices in the constant frequency regime. Although Sano and Mori^{3,4,21} found that the constant frequency bubble volume was proportional to $D_{no}^{\frac{1}{2}}$ for their small nozzles, (and this was confirmed with the smallest diameter in the present work, 0.635 cm), there appeared to be no discernable effect of D_{no} for larger nozzles. The large experimental random error in this regime could have been either the cause or the effect of this lack of

dependency. The apparent transition occurred between 0.6 and 1.3 cm in the constant frequency regime. It may be that there is insufficient time for the bubbles to reach large diameters. Alternatively, contact angle hysteresis⁶ may be important, and this would reduce the advancing contact angle, so that the interface would not reach the outer diameter.

Comparison with Previous Work

Mersmann²⁸ developed a semi-empirical equation for bubbles formed under constant flow ($N_c < 1$) conditions. Sano and Mori⁴ combined this equation with Equation (13) to obtain:

$$D_e = \left[\frac{3\sigma D_{no}}{\rho g} N_c^m + \left(\frac{9\sigma^2 D_{no}}{\rho^2 g^2} N_c^{2m} + \frac{KQ^2 D_{no}}{g} \right)^{1/2} \right]^{1/3} \quad (23)$$

where $m = 1$. K is an empirical constant which has a value of 10 that was derived from Equation (20). Thus at high flow rates the last term predominates and the equation approaches Equation (20). At the lower flow rates, the first two terms are most important, and Equation (23) reduces to Equation (13). Equation (23) with $m = 1$ was used in the presentation of Sano and Mori's work as well as in the present work for 0.635 cm outside diameter nozzles. For all the other results of the present work, it was found that 0.816 was a more appropriate value of m , as described above. The last term has no dependency on capacitance, because it was derived for constant flow conditions. Nevertheless, there is a substantial effect of chamber volume on the constant frequency obtained at higher flow rates in water^{14,17}. This is also observed in the present work, in that at large capacitances with large flow rates the results are consistently under-predicted. Better cor-

relations are not available even in aqueous systems because of the complication of "pairs" and "double pairs".

In Figure 21, the results of the present study are compared with typical results obtained by other investigators in metallic systems. The graph spans 5 orders of magnitude of flow rate and 3-1/2 of bubble volume. As one can see, the results of Sano and Mori⁴ lie considerably below the results of the present study. Their nozzles were much smaller, which not only decreases the constant volume size, but shifts the "constant frequency" results to the lower right. At low flow rates their results are consistently higher than predicted by Equation (21), while at higher flow rates they are below the curve. They did not report the occurrence of doublets or pairs. It is not possible to compare directly the results of Andreini et al.²⁹ for copper, lead and tin with those of the present study, since these authors reported neither chamber volumes nor outside diameters.

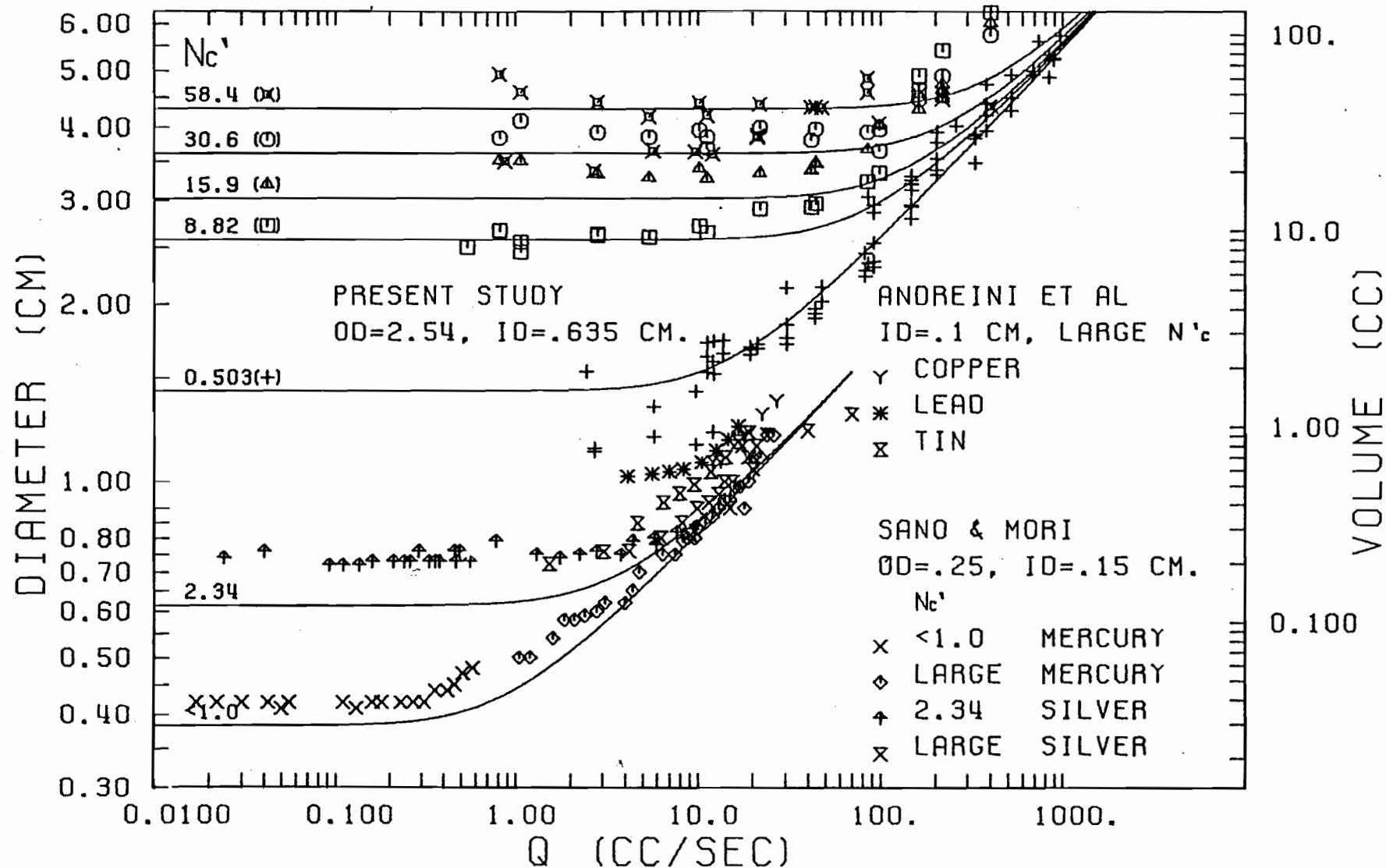


FIGURE 21. Bubble volume and equivalent diameter as a function of flow rate, at the bath temperature in metallic systems. Equation (23) was used with $m = 1$ and 0.816 for the work of Sano and Mori⁴ and the present work, respectively.

CONCLUSIONS

It is believed that the bubble volume-flow rate correlations presented are valid for all non-wetting, liquid metal systems, as long as the magnitudes of experimental parameters (such as flow rate and chamber volume) do not exceed the present ones. It must also be recognized that doublets or pairs may be formed, and that the chamber volume is most important in this regard. In industrial pyrometallurgical operations, chamber volumes are often quite large, so as to keep the control valves out of the hot zone. This, together with the non-wetting phenomenon leading to bubble formation at the outer nozzle diameter, tends to make the bubbles very large. The net result is quite different from the case of aqueous systems, in which small bubbles are easily obtained at low flow rates. Water models are quite often used to visualize bubble sizes or bubble-induced flow patterns in metallurgical systems; hence results of this nature must be carefully interpreted, in light of the present results. These large bubble sizes should be recognized as a design problem for any metallurgical bubbling system in which the efficiency relies upon good gas-metal contact and small bubble volumes.

NOMENCLATURE

<u>Symbol</u>	<u>Significance</u>
c	velocity of sound in the gas phase, cm.s^{-1}
C_p	specific heat of the gas at constant pressure, $\text{J.kg}^{-1}.\text{K}^{-1}$
C_v	specific heat of the gas at constant volume, $\text{J.kg}^{-1}.\text{K}^{-1}$
D_e	equivalent spherical diameter of a bubble, cm
D_{ni}	inside diameter of a nozzle, cm
D_{no}	outside diameter of a nozzle, cm
f	frequency of bubble formation, s^{-1}
g	gravitational acceleration, $981 \text{ cm}^2.\text{s}^{-1}$
h	height of the bath over the nozzle, cm
K	dimensionless empirical constant in Equation (23)
m	exponent in Equation (23)
N_c, N'_c, N_c^a	dimensionless capacitance numbers defined by Equations (11), (15), and (17), respectively
P	pressure, dyne.cm^{-2}
P_s	static pressure at the nozzle, dyne.cm^{-2}
Q	volumetric gas flow rate at bath temperature, $\text{cm}^3.\text{s}^{-1}$
s	distance between the bubble centre and the orifice, cm
T	temperature, K
T_s	bath temperature, K
T_{V_c}	temperature in the antechamber, K
V_b	volume of the bubble at the bath temperature, cm^3
V_{bm}	bubble volume defined by Equation (1) or (2), cm^3
V_c	volume of the antechamber, cm^3

<u>Symbol</u>	<u>Significance</u>
γ	ratio of specific heats, C_p/C_v
θ	apparent contact angle
θ_o	equilibrium contact angle measured in the liquid
ρ	density of the liquid, 7.0 g.cm^{-3} for pig iron
ρ_g	density of the gas at the bath temperature, g.cm^{-3}
σ	surface tension of the liquid, dyne/cm
ϕ	supplement of contact angle ($180^\circ - \theta_o$)

REFERENCES

1. R.J. Benzing and J.E. Myers: Ind. & Eng. Chem., 1955, Vol. 47, pp. 2087-90.
2. T. Tadaki and S. Maeda: Kagaku Kogaku (Abridged edition), 1963, Vol. 1, No.1, pp.55-60.
3. M. Sano and K. Mori: Tetsu-to-Hagane, 1974, Vol. 60, No.3, pp.348-60.
4. M. Sano and K. Mori: Trans. J.I.M. (Japan), 1976, Vol. 17, pp.344-52.
5. C.K. McKenzie: M. Eng. Thesis, McGill University, Montreal, 1975.
6. A.W. Adamson: Physical Chemistry of Surfaces, 2nd ed., John Wiley & Sons, N.Y., 1967, pp.352-69.
7. J.W. Gibbs: Scientific Papers, 1906, Vol. 1, p.326, Dover Reprint, Dover, N.Y., 1961.
8. J.F. Oliver, C. Huh and S.G. Mason: Journal of Colloid and Interface Science, 1977, Vol. 59, No.3, pp.568-81.
9. J.F. Davidson and B.O.G. Schuler: Trans. Instn. Chem. Engrs., 1960, Vol. 38, pp.335-42.
10. R. Kumar and N.R. Kuloor: Adv. Chem. Eng., 1970, Vol. 8, pp.255-368.
11. K. Ruff: Chem. Ing. Techn., 1972, Vol. 44, pp.1360-66.
12. I. Leibson, E.G. Holcomb, A.G. Cacosso and J.J. Jacmic: A.I.Ch.E.J., 1956, Vol. 2, pp.296-306.
13. L. Davidson and E.H. Amick: A.I.Ch.E.J., 1956, Vol. 2, pp.337-42.
14. D.J. McCann and R.G.H. Prince: Chem.Eng.Sci., 1969, Vol. 24, pp.801-14.
15. R.R. Hughes, A.E. Handlos, H.E. Evans and R.L. Maycock: Chem. Eng. Prog., 1955, Vol. 51, pp.557-63.
16. R.S. Brodkey: The Phenomena of Fluid Motions, pp.544-54, Addison-Wesley Publishing Co., Reading, Mass., 1967.
17. A. Kupferberg and G.J. Jameson: Trans. Instn. Chem. Engrs., 1969, Vol. 47, pp.T241-50.

18. D.J. McCann and R.G.H. Prince: Chem. Eng. Sci., 1971, Vol. 26, pp.1505-12.
19. K.G. Davis: CANMET, Ottawa, private communication.
20. J.F. Elliott, M. Gliesser and V. Ramakrishnan: Thermochemistry for Steelmaking II, Addison-Wesley Press, Reading, Mass., 1963, pp.498-99.
21. M. Sano, Y. Fujita and K. Mori: Met. Trans. B, 1976, Vol. 7B, pp.300-01.
22. G.R. Belton: Met. Trans. B, 1976, Vol. 7B, pp.35-42.
23. J.P. Morris and R.C. Buehl: Trans. A.I.M.E., 1950, Vol. 188, pp.317-22.
24. G.N. Oryall and J.K. Brimacombe: Met. Trans. B, 1976, Vol. 7B, pp.391-403.
25. R.H. Perry and C.H. Chilton, ed.: Chemical Engineers' Handbook, 5th Ed., McGraw-Hill Book Co., New York, 1973, pp.10-12 to 10-16.
26. E. Selcuk and D.H. Kirkwood: J.I.S.I., 1973, Vol. 211, pp.134-40.
27. R.H. McSwain, C.E. Bates and W.D. Scott: A.F.S. Cast Metals Research Journal, Dec. 1974, pp.181-90.
28. A. Mersmann: VDI-Forschungsheft 491, 1962, Vol. 28, pp.1-39.
29. R.J. Andreini, J.S. Foster and R.W. Callen: Met. Trans. B, 1977, Vol. 8B, pp.625-31.

LIST OF FIGURES AND TABLE

- Figure 1 Schematic representation of bubble formation in aqueous wetting and metallic non-wetting systems.
- Figure 2 The effect of an edge on an approaching gas/liquid interface having an equilibrium contact angle θ_0 and an observed one of θ , after References 7 and 8.
- Figure 3 A comparison of doublet and pair formation with traces of bubbles photographed at high speed, after References 2, 13, 14 and 18.
- Figure 4 A schematic diagram of the high temperature experimental apparatus.
- Figure 5 Schematic representation of X-ray cinematographic apparatus.
- Figure 6 Strip-chart traces of bubbles, "tapped" by hand, nozzle outside diameter, 1.27 cm; inside diameter, 0.635 cm; chamber volume, 23 cm³; chart speed, 5 cm s⁻¹; μ V/vertical division, 1000.
 A: flow rate, 2.78 cm³s⁻¹; f, 1.65 s⁻¹, bubble volume, 1.68 cm³
 B: flow rate, 2.45 cm³s⁻¹; f, 2.71 s⁻¹, bubble volume, 0.904 cm³
- Figure 7 Strip-chart traces of bubbles, obtained electronically.
 A: nozzle outside diameter, 5.08 cm; inside diameter, 0.635 cm; chamber volume, 23 cm³; flow rate, 40 cm³s⁻¹; chart speed, 20 cm s⁻¹; μ V/vertical division, 200; f, 11.9; bubble volume, 3.36 cm³
 B: nozzle outside diameter, 1.27 cm; inside diameter, 0.635 cm; chamber volume, 23 cm³; flow rate, 40 cm³s⁻¹; chart speed, 20 cm s⁻¹; μ V/vertical division, 20; f, 13.7 s⁻¹; bubble volume, 2.92 cm³
- Figure 8 Strip-chart traces of bubbles, obtained electronically, nozzle outside diameter, 2.54 cm; inside diameter, 0.635 cm; chamber volume, 342 cm³; chart speed, 5 cm s⁻¹; μ V/vertical division, 100.
 A: flow rate, 2.78 cm³s⁻¹; f, 0.294 s⁻¹; bubble volume, 9.45 cm³
 B: flow rate, 5.51 cm³s⁻¹; f, 0.586 s⁻¹; bubble volume, 9.40 cm³

Note: Bubble marked with "X" is a pair.

- Figure 9 Bubble volume and equivalent diameter as a function of flow rate, at 1523 K, for an outside nozzle diameter of 5.08 cm and inside diameter of 0.635 cm.
- Figure 10 Bubble volume and equivalent diameter as a function of flow rate, at 1523 K, for an outside nozzle diameter of 2.54 cm and inside diameter of 0.635 cm.
- Figure 11 Bubble volume and equivalent diameter as a function of flow rate, at 1523 K, for an outside nozzle diameter of 2.54 cm and inside diameter of 0.318 cm.
- Figure 12 Bubble volume and equivalent diameter as a function of flow rate, at 1523 K, for an outside nozzle diameter of 1.27 cm and inside diameter of 0.635 cm.
- Figure 13 Bubble volume and equivalent diameter as a function of flow rate, at 1523 K, for an outside nozzle diameter of 1.27 cm and inside diameter of 0.318 cm.
- Figure 14 Bubble volume and equivalent diameter as a function of flow rate, at 1523 K, for an outside nozzle diameter of 0.635 cm and inside diameter of 0.159 cm.
- Figure 15 Bubble volume and equivalent diameter as a function of flow rate, at 1523 K, for an outside nozzle diameter of 2.54 cm, an inside diameter of 0.318 cm and a chamber volume of 615 cm³. The nozzle orientation is varied as indicated and for 1 set of data the sulphur content was 0.2%.
- Figure 16 X-ray photographs of gas injection into the indium-gallium melt, accompanied by tracings for the sake of clarity. Note the horizontal nozzle with attached bubbles and the free surface of the melt. (A) shows bubble formation at the outer diameter of the nozzle. The gas flow rate was 22 cm³s⁻¹, and the X-ray unit was operated at 100 kV and 2 mA. (B) shows bubble formation on the upper part of the nozzle under the same conditions as (A). (C) shows movement of the bubbles back along the top of the nozzle. The gas flow rate was 63 cm³s⁻¹, and the power was 100 kV at 2 mA.
- Figure 17 Bubble volume and equivalent diameter as a function of capacitance for bubbles in the constant volume regime with various nozzle diameters, as indicated. The numbers associated with each data point refer to the flow rate, cc/sec at 1523 K, at which the transition from single to pair bubbling was observed.

- Figure 18 Bubble volume and equivalent diameter as a function of capacitance for the present study and others (References 2, 4 and 13). The capacitances were calculated by Equations (11) and (16) for the water and metallic studies, respectively.
- Figure 19 Schematic representation of the consecutive steps of bubble formation at nozzles with the three principal orientations in a liquid metal at low gas flow rate. See text for the explanation.
- Figure 20 Schematic representation of bubble formation at nozzles of various size in a liquid metal. The bubble volumes from Equations (2) and (4) are shown. See text for further explanation.
- Figure 21 Bubble volume and equivalent diameter as a function of flow rate, at the bath temperature in metallic systems. Equation (23) was used with $m = 1$ and 0.816 for the work of Sano and Mori⁴ and the present work, respectively.
- Table I Chemical Analyses of the Pig Iron Baths

PART II

MAGNESIUM DESULPHURIZATION OF IRON-CARBON MELTS

ABSTRACT

The object of this study was to determine the kinetic mechanism of magnesium desulphurization of blast furnace iron, a process which has been used for several years. A magnesium vaporizer was used to inject magnesium into 60 kg baths of carbon-saturated iron at 1523 K. The frequency of bubble formation and thus bubble size was measured. The bubbles were initially at least 10 cm^3 and dissolved with a mass transfer coefficient of $4.6 \pm 3.4 \times 10^{-3} \text{ cm s}^{-1}$. In the range of sulphur levels studied (0.0002 to 0.2%), the desulphurization occurred primarily in the bulk of the liquid by a second order (with respect to dissolved sulphur and magnesium) heterogeneous reaction. However, the back reaction became significant at the lower sulphur levels, and the solubility product, $\% \text{ Mg} \cdot \% \text{ S}$ was found to be 8×10^{-6} which complements equilibrium data. A mechanism involving random collisions of magnesium and sulphur in the liquid with subsequent precipitation on inclusions is postulated.

INTRODUCTION

As stated in the Introduction to this Thesis, Part II is concerned with the rate and mechanism of magnesium desulphurization of iron. The following Previous Work section contains the literature pertinent to the explanation of the present experimental work. (Other previous work on magnesium desulphurization is contained in Appendix A.)

On first reading, it may not be readily apparent why sections on such diverse phenomena as mass transfer to bubbles, homogeneous nucleation and heterogeneous deoxidation have been included. Briefly, magnesium vapour was injected into the iron and the results indicated that the magnesium dissolved from the bubbles. It appeared that most of the desulphurization did not occur at the bubble interfaces. There are then the possibilities of homogeneous nucleation of MgS in the liquid iron, or the nucleation of MgS on other small inclusions in the melt. These situations are quite similar to the deoxidation of liquid steel in which elements such as aluminum, silicon and manganese are added to the bath to reduce the dissolved oxygen content.

PREVIOUS WORK

Thermodynamics

Magnesium solubility in iron

The equilibrium solubility of magnesium in iron-carbon alloys has been determined by several investigators.¹⁻⁴ They all found that the magnesium dissolved according to Henry's Law, and that the equilibrium can be represented by:

$$\text{Mg}_{(v)} \rightleftharpoons \underline{\text{Mg}}(\%) \quad K_1 = \frac{\% \text{Mg}}{P_{\text{Mg}}} \quad (1)$$

The results have been previously discussed⁵ and are reproduced in Appendix B. For the present experimental conditions (4.4% C, 0.1% Si at 1523 K), K_1 is 0.7% Mg.atm⁻¹.^{*} Carbon enhances the solubility, raising it to 0.8% Mg.atm⁻¹ at 4.7% C, while 1% silicon depresses the solubility to 0.6% Mg.atm⁻¹ at 1523 K. A 50 K increase in temperature decreases the solubility to 0.5% Mg.atm⁻¹. The estimated accuracy of these values is $\pm 0.1\%$ Mg.atm⁻¹.

Desulphurization

Spear and Parlee⁴ also investigated the desulphurization of carbon-saturated iron at 1533 K with magnesium vapour:

* All compositions expressed in % are on a weight basis. The S.I. unit of pressure is the Pascal, equal to 0.987×10^{-5} atmospheres. The other non-S.I. units used in this Part are the minute (60 seconds), the hour (3600 seconds) and the metric tonne (1 megagram).



where the standard states are pure MgS, pure magnesium vapour at 1 atm. and carbon-saturated iron at 1533 K. Infinitely dilute solutions in the weight percent scale are the reference states. Under their experimental conditions the dissolved magnesium was much greater than the sulphur content, as shown in Figure 1. In fact, the magnesium reduced the sulphur activity coefficient, f_s , so much that the equilibrium sulphur content increased with increasing magnesium content. Following their analysis, the apparent equilibrium constant is:

$$K_2' = P_{\text{Mg}} \cdot \%S \quad (3)$$

and

$$h_s = f_s \cdot \%S \quad (4)$$

Combination of the three previous equations and expansion using interaction parameters yields

$$\log K_2 = \log K_2' + e_s^S \%S + e_s^{\text{Mg}} \%Mg \quad (5)$$

Both e_s^S and $\%S$ are small and may be neglected. The present author performed a regression analysis of $\log K_2'$ against $\%Mg$ on their data to obtain

$$\log K_2 = -4.19 \pm 0.18 \quad (1 \text{ standard error of estimate}) \quad (6)$$

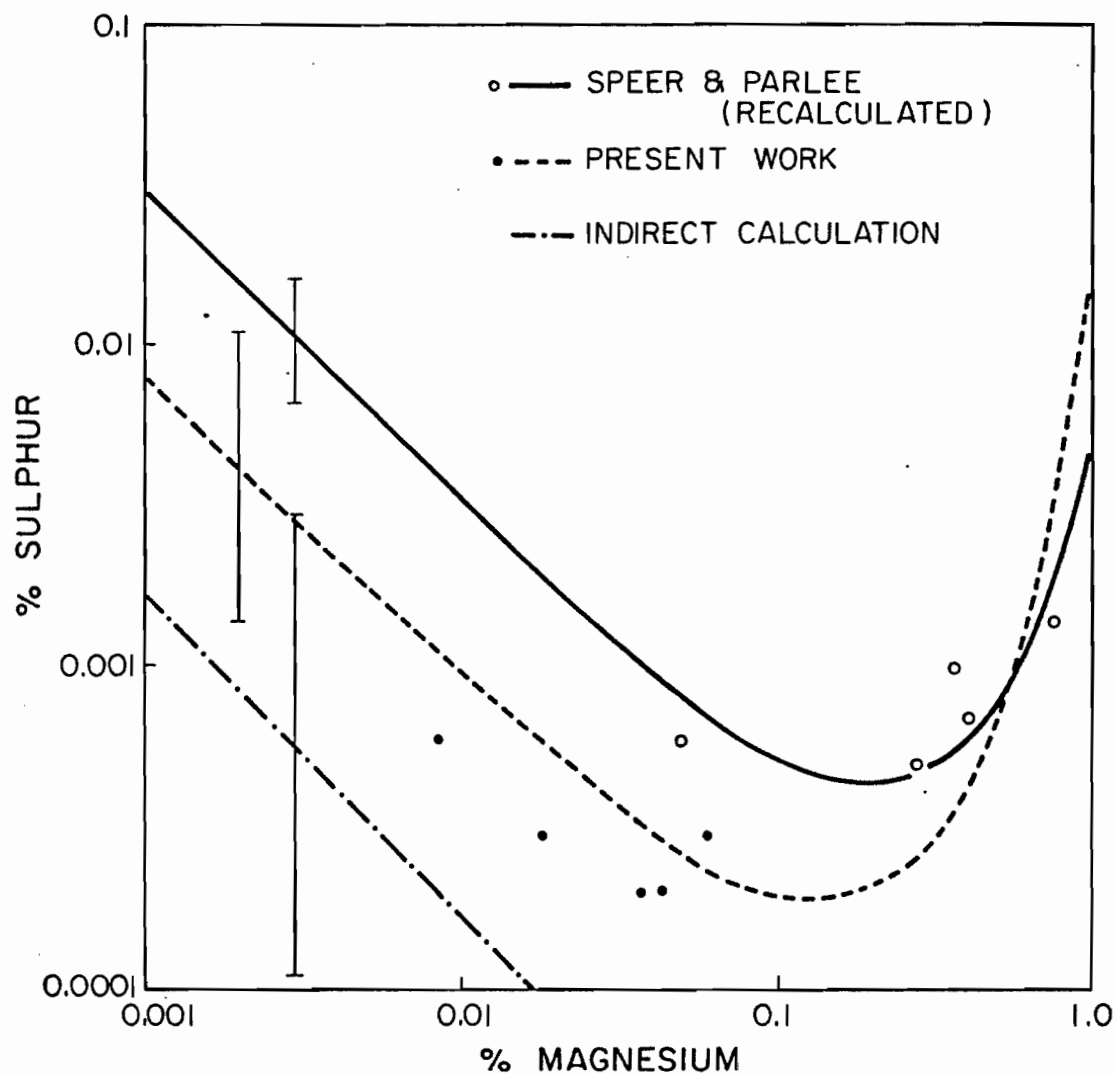


FIGURE 1. Thermodynamics of desulphurization with magnesium of carbon-saturated iron at 1523 K. Speer and Parlee's⁴ data is shown with the recalculated curve as described in the text. The present data was taken from Figure 11. The indirect calculation is described in the text. The error bars represent ± 1 standard error of estimate.

and

$$e_s^{\text{Mg}} = -1.82 \pm 0.34 \quad (7)$$

The present author also repeated Speer and Parlee's analogous calculations for the equilibrium

$$\text{MgS} \rightleftharpoons \underline{\text{Mg}}(\%) + \underline{\text{S}}(\%) \quad K_3 = h_{\text{Mg}} \cdot h_{\text{S}} \quad (8)$$

to obtain

$$\log K_3 = -4.50 \pm 0.19 \quad (1 \text{ standard error of estimate}) \quad (9)$$

Speer and Parlee quoted a value of 6.42×10^{-5} for K_3 , whereas the present regressions on their data yielded 3.16×10^{-5} for K_3 and 6.43×10^{-5} for K_2 . This discrepancy was probably due to a typographical error on their part.

A somewhat different, indirect method can be used to calculate K_2 and K_3 . Equation (2) is actually the combination of two other equilibria which have been determined independently:^{6,7}

$$\text{MgS} \rightleftharpoons \text{Mg}(\text{v}) + \frac{1}{2} \text{S}_2(\text{g}) \quad K_4 = P_{\text{Mg}} \cdot P_{\text{S}_2}^{\frac{1}{2}} \quad (10)$$

$$\frac{1}{2} \text{S}_2 \rightleftharpoons \underline{\text{S}}(\%) \quad K_5 = \% \text{S} \cdot P_{\text{S}_2}^{-\frac{1}{2}} \quad (11)$$

$$\text{Thus,} \quad \log K_2 = -5.61 \pm 0.72 \quad (12)$$

Combining this with Equation (1) yields

$$\log K_3 = -5.76 \pm 0.72 \quad (13)$$

The K_3 values are compared in Figure 1. The recalculation of Speer and Parlee's work is to be preferred over the indirect calculations because of the smaller error limits and because of the agreement with the experiments performed in the iron-carbon system.

Mass Transfer and Reactions

The overall processes of dissolution or chemical reaction at heterogeneous interfaces are usually considered to consist of several consecutive steps: transport to the reaction interface, adsorption of reactants on the interface, the reaction or dissolution step, desorption of the products and finally transport away from the interface. Any combination of these steps could control the overall rate.⁸ Each of these steps is considered separately in the following review for situations similar to the present case of magnesium dissolution and the formation of magnesium sulphide. The conditions for homogeneous nucleation are also considered.

Liquid phase control

The mass transfer coefficients of rising bubbles are usually defined in terms of the equivalent area of a spherical bubble of the same volume; thus the transfer rate is

$$\dot{N}_i = k_{LE} A (C_i^* - C_i^B) \quad (14)$$

These concentrations are the ones at the interface and in the bulk, respectively. The theoretical and experimental determination of mass transfer coefficients has been extensively investigated in low temperature systems.⁹ (See Appendix C.) However, the present discussion will be limited to spherical cap bubbles with open wakes, the shape assumed by bubbles larger than approximately 4 cm^3 in water and liquid metals.¹⁰ By assuming potential flow over the front or upper surface of the bubble, the theoretical value of the mass transfer coefficient for the front has been well established to be:¹¹⁻¹⁴

$$k_{LF} = 0.951 g^{\frac{1}{4}} D_L^{\frac{1}{2}} D_E^{-\frac{1}{4}} \quad (15)$$

Higbie's¹⁵ penetration theory has also been applied to spherical cap bubbles to obtain approximate mass transfer coefficients.^{13,16} Generally, the mass transfer coefficient from penetration theory is:

$$k_L = 2 \left(\frac{D_L}{\pi t_{Ex}} \right)^{\frac{1}{2}} \quad (16)$$

where the exposure time, t_{Ex} is determined by the specific conditions of the interface. In this case¹³

$$\begin{aligned} t_{Ex} &= \frac{\text{length of the bubble spherical surface}}{\text{mean velocity over the bubble}} \\ &= 0.0716 D_E^{\frac{1}{2}} \end{aligned} \quad (17)$$

Thus the mass transfer coefficient is

$$k_{LF} = 0.716 g^{\frac{1}{4}} D_L^{\frac{1}{2}} D_E^{-\frac{1}{4}} \quad (18)$$

Transfer from the rear of the bubble is not as well understood. Weber¹⁴ used the penetration theory to relate the observed rate at which wake vortices are shed to the mass transfer rate from the rear:

$$k_{LR} = 0.290 g^{\frac{1}{4}} D_L^{\frac{1}{2}} D_E^{-\frac{1}{4}} \quad (19)$$

Since complete renewal was assumed at each shedding, this would represent the upper limit to transfer from the rear.

In aqueous systems, it has been shown that surface-active agents reduce mass transfer rates for spherical cap bubbles.^{12,17} This is usually ascribed to immobilization of the bubble interface, rather than to a reduction in effective surface area.¹³ The slower interfacial velocities result in less solute penetration, and lower transfer rates. Weber¹⁴ has developed a theoretical mass transfer coefficient for a spherical cap bubble with various amounts of surfactant dissolved in the liquid. The concentration of surfactant is related to the reduction in surface tension which delineates the extent of the stagnant region. For a totally stagnant front the mass transfer coefficient is:

$$k_{LF} = 0.7 g^{\frac{1}{4}} D_L^{\frac{1}{2}} D_E^{-\frac{1}{4}} Sc^{-\frac{1}{6}} \quad (20)$$

This model agrees reasonably well with experimental results where polyvinyl alcohol was added to water.¹⁴

The only metallic system that has been carefully investigated is oxygen dissolution into silver.¹⁸⁻²⁰ Oxygen is extremely surface active in silver²¹, thus the entire bubble surface would be expected to be immobilized. However, the measured mass transfer coefficients fall between mobile (Equation (15)) and immobile cases (Equation (20)). Sano et al.^{20,22} also found that when the bubble became smaller the rate dropped drastically. This is frequently observed in aqueous systems because small bubbles are more easily immobilized. For a further discussion of surfactants, refer to the section on adsorption.

Magnesium was found to evaporate from the bath surface. If the rate were liquid-phase controlled, it would be dependent on the rate of bath surface renewal. Machlin²³ applied the penetration theory (Equation (16)) to mass transfer from an inductively-stirred crucible, where the contact time is the radius of the crucible, R_c , divided by the average surface velocity, U . The mass transfer coefficient is then

$$k_L = 2 \left(\frac{D_L U}{R_c} \right)^{\frac{1}{2}} \quad (21)$$

The surface velocity can be either measured directly or calculated by solving the turbulent, electromagnetically-driven fluid-flow equations. Both methods have been used previously for the present experimental conditions.^{5,24,25} The calculated mass transfer coefficients are in good agreement with the experimental ones.

Gas phase control

It is convenient to consider gas phase resistance as an extra resistance to liquid phase control;²⁶ thus the overall transfer rate is given by:

$$\dot{N}'' = k_{LOV}(C_L^G - C_L^L) \quad (22)$$

$$= \left(1 + \frac{K_H k_L}{k_G}\right)^{-1} k_L (C_L^G - C_L^L) \quad (23)$$

The concentration in the gas phase is converted to the equivalent liquid concentration C_L^G by

$$K_H = C_L/C_G \quad (24)$$

for a gas which obeys Henry's Law. There have been no experimental investigations to confirm these relations or to determine a gas phase mass transfer coefficient.²⁷ However, the coefficient can be estimated by assuming that the circulation within the bubble is the same as the liquid-phase circulation:²⁸

$$\frac{k_L}{k_G} = \left(\frac{D_L}{D_G}\right)^{\frac{1}{2}} \quad (25)$$

Adsorption

It has been found from surface tension measurements that oxygen, sulphur, selenium and tellurium are very surface active in liquid iron.²⁹ Furthermore, the saturation coverages and activation

energies are close to those corresponding to compounds such as FeO and FeS forming on the surface.²⁹ The fractional surface coverage, θ_i , is well described by Langmuir's Adsorption isotherm³⁰

$$K_i = \frac{\theta_i}{(1 - \theta_i)a_i} \quad (26)$$

This indicates that these elements are chemisorbed, as opposed to being physically adsorbed. (See Table 1.)

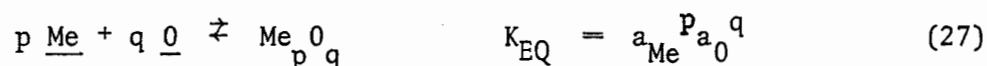
It has also been shown that the surface-active elements hinder the dissolution of nitrogen in proportion to the surface coverage θ_i , at high surface coverages in inductively-stirred crucibles.³⁰ Because these elements are so strongly adsorbed and are very difficult to eliminate completely, there is little data for surface coverages less than 0.3. However, at these levels, the rates are well described by the liquid phase transport of Machlin's model (Equation (21)), whereas they should only be 70% of this value if the sites are blocked. In aqueous systems, surfactants are considered to immobilize the bubble interfaces.^{13,14} This reduces the theoretically derived mass transfer rates by factors of between 2 and 10 from the penetration theory (see Appendix C). However, few experimental results confirm this, and in fact there is generally a great deal of difference among the work of various investigators, as well as among various surfactants.²² This apparent random behaviour of surfactants in aqueous systems, as opposed to the more uniform behaviour of oxygen, sulphur, selenium and tellurium in metallic systems, may be due to differences in the intrinsic nature of the adsorption bond.

TABLE I
COMPARISONS OF PHYSICAL AND CHEMICAL ADSORPTION
(AFTER ADAMSON³¹)

Aspect	Physical	Chemical
Bonding	Van Der Waal's	Chemical
Heat of adsorption	Similar to heat of condensation	Similar to heat of reaction
Activation energy	$\lesssim 5 \text{ kJ} \cdot \text{mol}^{-1}$	$\gtrsim 5 \text{ kJ} \cdot \text{mol}^{-1}$
Thickness of layer	Can be many atoms	1 atom
Reversibility	Reversible	Desorption is slow; often activated
Temperature Restriction	Only important below the critical temperature of the adsorbate	None

Homogeneous nucleation

The thermodynamic and kinetic conditions for homogeneous nucleation have been investigated both theoretically and experimentally, but there are many uncertainties and the analysis is only approximate.³² For a typical deoxidation-type reaction:



the product is insoluble in the iron and must precipitate. For homogeneous nucleation, the free energy required for the creation of the new interfacial area of the nucleus must come from the reaction free energy. For a nucleus of radius r_I the free energy change is:³²

$$\Delta G = -\frac{4}{3}\pi r_I^3 C_M RT \ln \frac{K_S}{K_{\text{EQ}}} + 4\pi r_I^2 \sigma_{\text{LS}} \quad (28)$$

where K_S/K_{EQ} is the amount of supersaturation. This function passes through a maximum at a critical radius r_{IC} where the supersaturation is given by:

$$\ln\left(\frac{K_S}{K_{\text{EQ}}}\right) = \frac{2\sigma_{\text{LS}}}{RTC_M r_{\text{IC}}} \quad (29)$$

This is also known as the Kelvin Equation.

The critical energy to reach this nucleus is

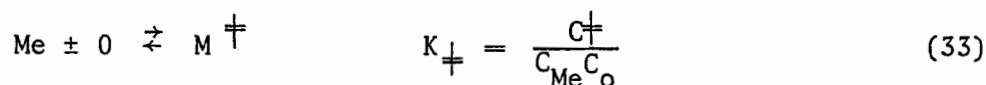
$$\Delta G_{\text{max}} = \frac{16\pi \sigma_{\text{LS}}^3}{3(C_M RT \ln \frac{K_S}{K_{\text{EQ}}})^2} \quad (30)$$

For larger nuclei there are no restrictions on growth, so that the rate of nucleation is governed by the rate at which sub-critical nuclei are formed. Essentially this is the rate at which the reacting molecules or atoms collide, and the Kinetic Theory of Gases can be applied to the rate of nucleation in a gas or a liquid at infinite dilution:^{8,32}

$$I = \left(\frac{\delta_{\text{Me}} + \delta_{\text{o}}}{2}\right)^2 \left(\frac{8\pi(M_{\text{Me}} + M_{\text{o}})RT}{M_{\text{Me}}M_{\text{o}}}\right)^{\frac{1}{2}} P_{\text{R}} n_{\text{Me}} n_{\text{o}} \exp\left(-\frac{\Delta G_{\text{max}}}{k_{\text{B}}T}\right) \quad (31)$$

$$= 10^{-10} P_{\text{R}} n_{\text{Me}} n_{\text{o}} \exp\left(-\frac{\Delta G_{\text{max}}}{k_{\text{B}}T}\right) \text{ nuclei cm}^{-3} \text{s}^{-1} \quad (32)$$

where the activation energy necessary for a successful collision is ΔG_{max} and P_{R} is the steric or probability factor for proper orientation of reactants during collision. For two reacting atoms ($p = q = 1$) the steric factor should be unity. This can be demonstrated by the Theory of Absolute Reaction Rates.³² Here it is assumed that the activated complex is in equilibrium with the reactants:



and that the complex decays according to a particular vibration frequency ν , which can be numerically evaluated using approximate values of the molecular partition functions.⁸

$$I = \nu C_{\ddagger} \quad (34)$$

$$= \frac{k_{\text{B}}T}{h} \frac{F_{\ddagger}}{F_{\text{Me}} F_{\text{o}}} \exp(-\Delta G_{\text{max}}/hT) C_{\text{Me}} C_{\text{o}} \quad (35)$$

$$= 10^{-9} \exp(-\Delta G_{\max}/k_B T) n_{\text{Me}} n_{\text{O nuclei}} \text{ cm}^{-3} \text{ s}^{-1} \quad (36)$$

Considering the nature of the approximations, the agreement between Equations (32) and (36) is good.

Since the rate is an exponential function of the supersaturation, arbitrary values of I can be specified.³² Turkdogan³³ assumed that

$$I = 10^{27} \exp(-\Delta G_{\max}/k_B T) \quad (37)$$

and that I of 10^3 was sufficient for homogeneous nucleation. Substituting Equation (30) into (37) and rearranging, yields:

$$\ln\left(\frac{K_S}{K_{\text{EQ}}}\right) = \frac{1}{C_M RT} \left(\frac{16\pi \sigma_{\text{LS}}^3}{3k_B T \ln\left(\frac{10^{27}}{10^3}\right)} \right)^{\frac{1}{2}} \quad (38)$$

This function is plotted in Figure 2, along with the available deoxidation product nucleation data. Equation (29) is also shown for a critical radius of $2 \times 10^{-8} \text{ cm}$, which Von Bogdandy et al.^{34,35} considered to fit their data for the nucleation of ZrO_2 and Al_2O_3 from liquid steel melts. As one can see in Figure 2, homogeneous nucleation in liquid steel is not very well understood. This may in part be due to inaccuracy in the experimental results; the equilibrium constants, surface energies and critical supersaturations were all obtained from independent experiments which are difficult to perform.

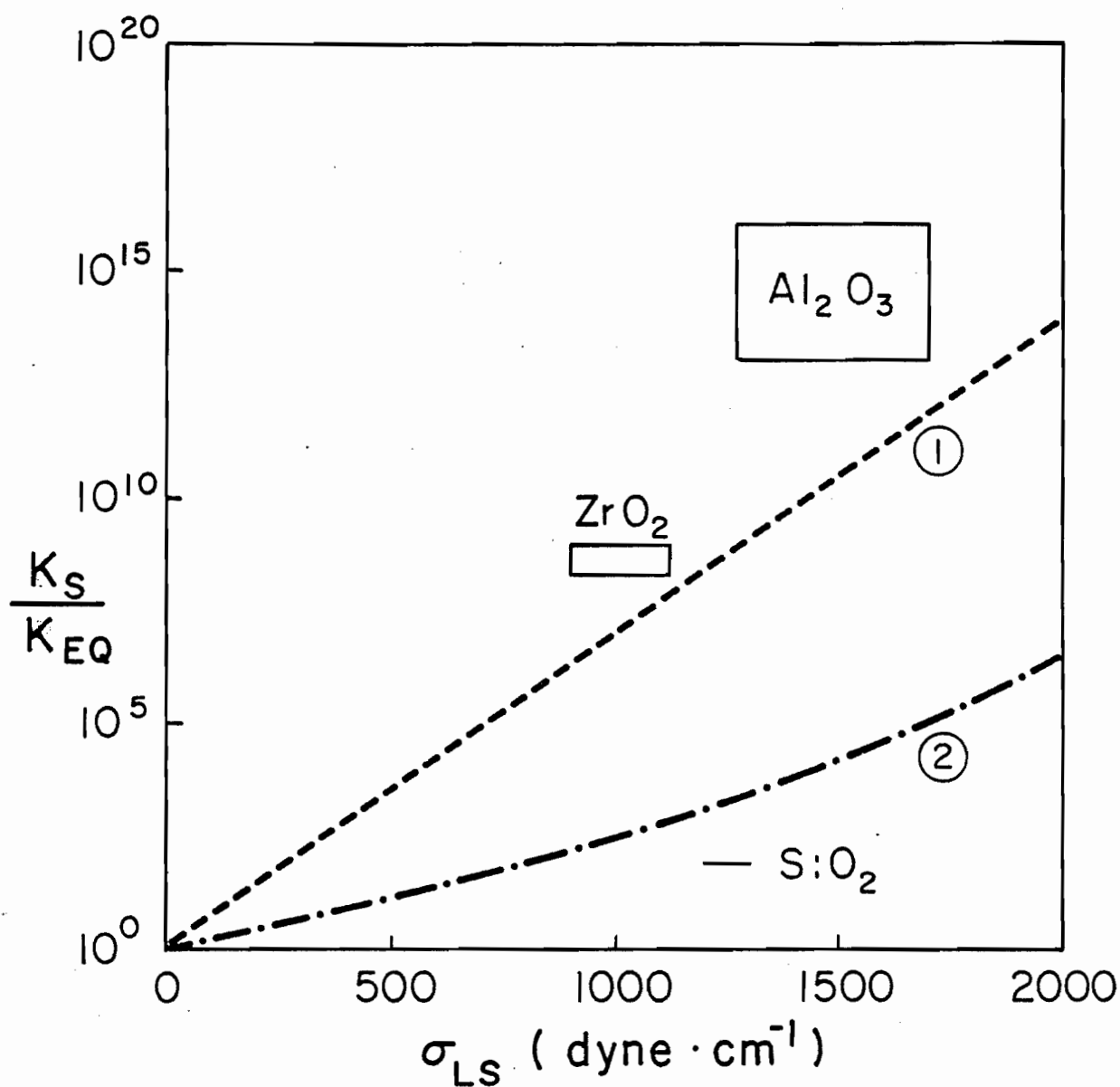


FIGURE 2. Supersaturation necessary for homogeneous nucleation. Line 1 represents Equation (29) and Line 2 represents Equation (38) with $T = 1523$ K and $C_M = 0.04$ mole cm^{-3} . The surface energies for SiO_2 , ZrO_2 and Al_2O_3 come from References 36, 37 and 38, respectively, while the critical supersaturations were taken from References 39, 34 and 35, respectively.

Heterogeneous deoxidation

Desulphurization is very similar to deoxidation of steel, the latter phenomenon having been extensively studied. The actual deoxidation reaction that occurs at heterogeneous sites is thought to be very fast, so that the rate is controlled by transport of the least abundant or slowest-moving reactant to these sites.³³ Turkdogan³³ developed a model for the unsteady-state diffusion of this reactant (usually oxygen) to evenly distributed inclusions in the melt (which are postulated to form as a result of homogeneous nucleation in regions of local supersaturation which occur shortly after the deoxidizer is added). The average diffusion radius for each of the n particles per cm^3 is:

$$r_o = \left(\frac{3}{4\pi n}\right)^{1/3} \quad (39)$$

It is assumed that the radius of an inclusion, r_I , is much smaller than r_o , so that the solution is independent of r_I . The solution is well approximated by:

$$\ln\left(\frac{C - C_{EQ}}{C_o - C_{EQ}}\right) = -2.558 \frac{D_L t}{r_o^2} \left(\frac{C_o - C_{EQ}}{C_M}\right)^{1/3} \quad (40)$$

where C_{EQ} is the equilibrium oxygen concentration at the interface, C_o is the starting concentration and C_M is the concentration within the deoxidizer. This model is said to apply under stagnant conditions or to small inclusions rising with Stokesian velocities. Its applicability has not been confirmed, but the model did explain the slow approach to equilibrium that was observed during deoxidation with rare earths in

laboratory experiments.⁴⁰

The steady-state solution of Wert and Zener⁴¹ can also be used under stagnant conditions. In their model, the initial particle radius is zero, but grows as the precipitation proceeds. The particle radius at complete reaction is:

$$r_{IF} = \left(\frac{C_o - C_{EQ}}{C_M - C_{EQ}} \right)^{1/3} r_o \quad (41)$$

The solution for the fractional precipitation is:

$$\ln \left(\frac{C - C_{EX}}{C_o - C_{EX}} \right) = - \left[\frac{2D_L t (C_o - C_{EQ})}{r_{IF}^2 (C_M - C_{EQ})} \right]^{3/2} \quad (42)$$

An estimate of the effects of forced convection can be gained from the Ranz-Marshall relation for mass transfer for solid spheres.⁴²

$$Sh = 2 + 0.6 Re^{1/2} Sc^{1/3} \quad (43)$$

In the absence of convection, the dimensionless mass transfer coefficient takes the value 2, and k_L becomes D_L/r_I which is simply the solution for radial diffusion obtained by Wert and Zener.⁴¹ For inclusion several micrometres in size, the Reynolds Number is less than 10^{-4} and the Schmidt Number is of the order of 10^2 , so that convection has a negligible effect on the transfer rates. By assuming a constant particle radius, the integrated form of the rate equation can be simply obtained:

$$\ln \left(\frac{C - C_{EX}}{C_o - C_{EX}} \right) = - 4\pi r_I^2 n k_L t \quad (44)$$

The value of r_I can be taken as $r_{IF}/2$, or taken from the radius observed by metallography. The three models are compared in Figure 3 for typical experimental conditions. The agreement is good considering the diversity of the assumptions.

From a review of the literature, Turkdogan⁴³ came to several general conclusions on the kinetics of deoxidation: The number of nuclei, n , as a result of homogeneous nucleation, is at least 10^6 cm^{-3} at the time of a deoxidizer addition. With such a large number of nuclei, the diffusion-controlled deoxidation is complete in a matter of seconds, and thus the rate is controlled by the rate of rise of the inclusions. Deoxidation inclusions range in size from 1 to 40 μm , and are observed to be eliminated more quickly than Stokes Law predicts. However, growth by collision cannot account for the high rates of deoxidation. In an effort to explain this discrepancy, it is postulated that parts of the melt may be depleted of nuclei and inclusions. In laboratory experiments, with 5 cm deep inductively-stirred melts, oxide inclusions float out in 3 to 10 minutes. Generally float-out due to induction stirring is faster than that from natural convection.

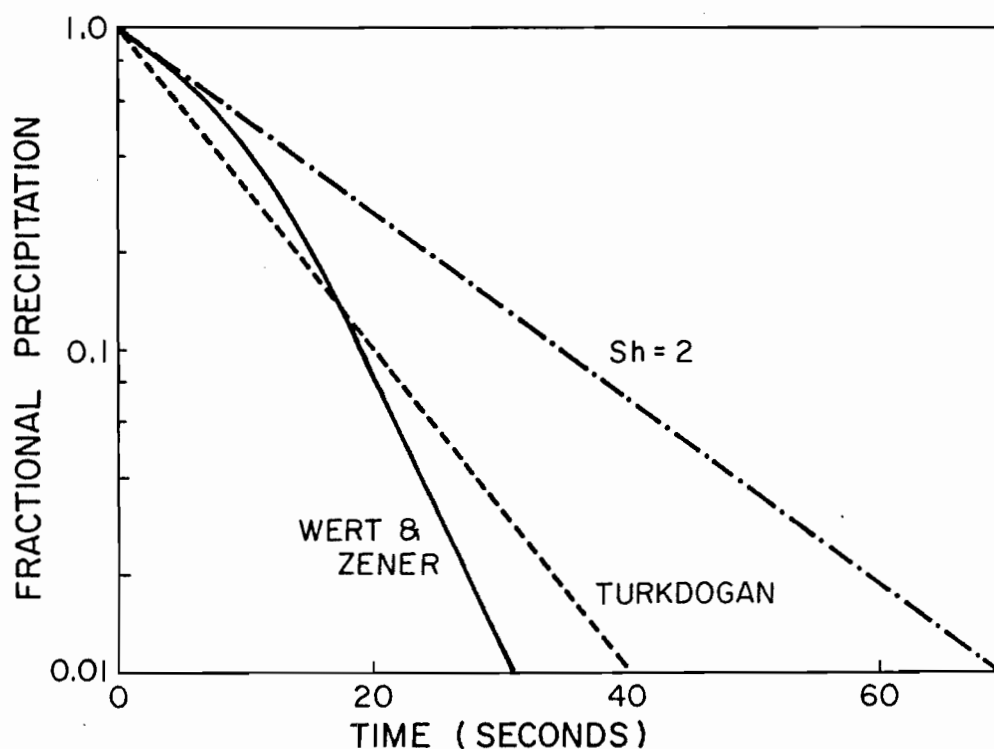


FIGURE 3. A comparison of the diffusion models of precipitation. The fractional precipitation is given by $\frac{C - C_{EQ}}{C_M - C_{EQ}}$. For these particular curves, C_M , C_0 and C_{EQ} are 0.05 , 10^{-5} and 10^{-6} mole cm^{-3} , respectively. The number of inclusions was assumed to be 10^6 cm^{-3} , thus r_{IF} is calculated to be $3.5 \times 10^{-4} \text{ cm}$. These numbers are typical of the present experimental situation for precipitation of MgS on inclusions.

APPARATUS AND PROCEDURE

Apparatus

In order to overcome the explosive vaporization of magnesium when it is plunged into molten iron, a vaporizer was constructed to provide a uniform flow of magnesium, so that the mass transfer rates could be studied. It was basically an improvement on the apparatus previously reported,^{5,24} in which pure magnesium was propelled by its own vapor pressure into the melt. A carrier gas could also be used to transport the magnesium with the present apparatus.

The apparatus is shown in Figure 4. A reflector furnace (Research Inc., Model 4068-24-10), having 24 1 kW lamps was used to maintain the retort at temperature, and to provide the heat for vaporization.. Because there was no insulation in this furnace (only water-cooled reflectors behind each lamp), the response was very rapid, and the power could be precisely controlled. The temperature controller (Research Inc., Model 624A) could provide either a constant temperature or a constant amount of power, depending on the mode of operation. An oxygen/methane burner was used to heat the lower part of the retort to prevent magnesium condensation. The burner was aimed tangentially through a cement-and-steel shroud, so that the combusting gases would swirl upward around the retort without melting it.

For the experiments conducted with argon carrier gas, the argon flow was metered by a calibrated needle valve operated at a 345 kPa pressure drop to ensure constant argon flow. The upper portion of the retort, adjacent to the valve, had a 1.9 cm internal diameter to

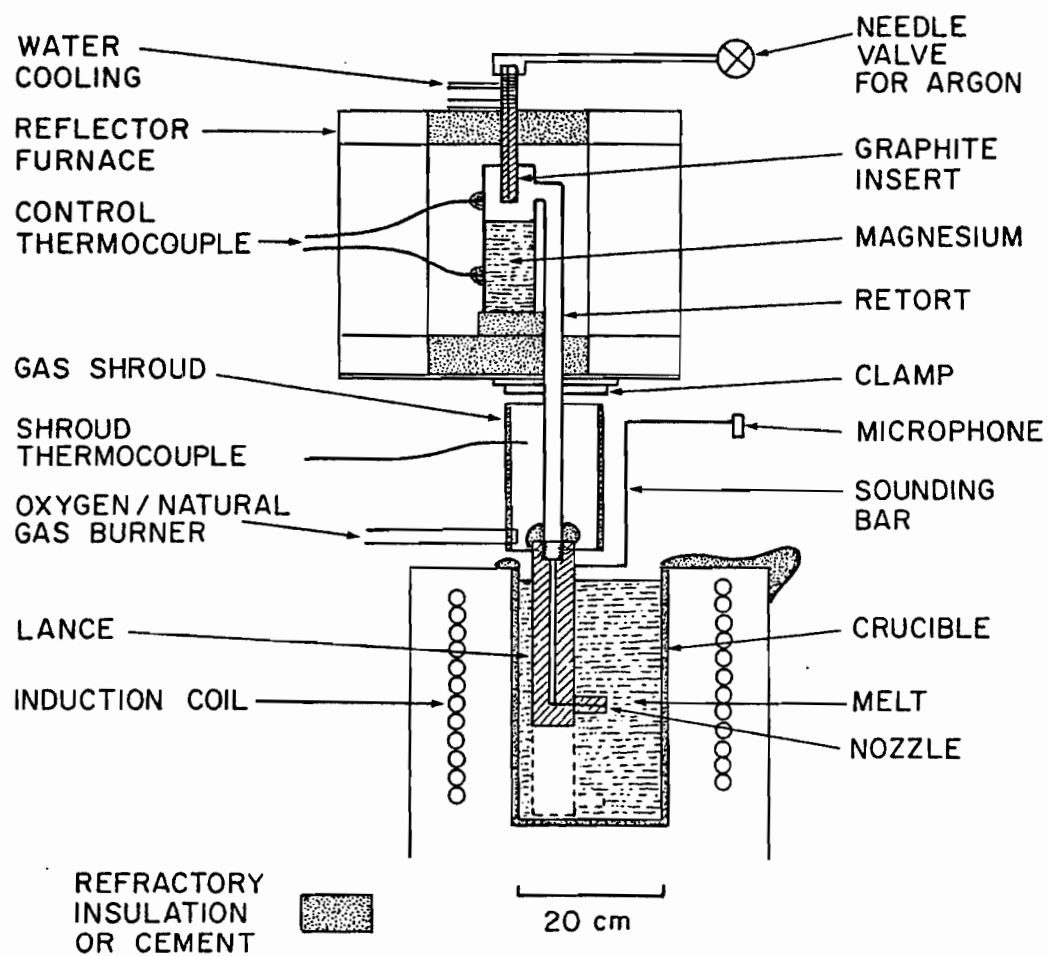


FIGURE 4. Schematic cross-section of the magnesium vaporizer and induction furnace, to scale.

facilitate loading. Consequently, a disposable graphite insert having a 3 mm bore was used to minimize magnesium condensation in the cold zone. The end of the insert from which the argon flowed was within 1 cm of the magnesium melt surface. For the pure magnesium runs a solid insert was used.

The retort was constructed from 310 Stainless Steel, having minimum wall thickness of 6 mm. This alloy provided the best compromise between high temperature strength and magnesium corrosion resistance, on the one hand, and the availability of appropriate shapes, on the other. Corrosion of the welds was a common reason for the failure of a run.

The lance assemblies were machined from fine grain, high purity graphite. The lance was screwed onto the retort, and the junction was covered with refractory cement to shield it from the burner flame. The nozzle tip had an outer diameter of 2.54 cm and an inner diameter of 0.318 cm. A steel bar was screwed into the lance, and a contact microphone was attached to the other end of the bar. The microphone was used to detect the vibrations caused by the release of a bubble from the nozzle. The details of the frequency transducer and recording system were previously reported.⁴⁴

A 150 kVA, 3 kHz Induction Furnace was used to melt and hold the iron at temperature. Alumina crucibles with a 19.8 cm internal diameter and 35.6 cm height were used.

Procedure

The retort was filled with 400 to 500 g of magnesium. After assembly of the furnace, the retort was flushed with argon. The retort

was heated to approximately 1300 K, and the shroud was heated to its operating temperature (1470 K). Meanwhile, the iron was melted from pigs with an excess of high purity graphite, to ensure carbon saturation. The pigs generally contained 7 to 50 ppm sulphur, so FeS was plunged into the bath in graphite bells to increase the starting sulphur level. After this treatment, the lance was lowered into the melt.

For Runs 1 and 2, pure magnesium was injected by operating the reflector furnace in the constant power mode. The power was increased so that the retort temperature approached the boiling point of magnesium at the ferrostatic pressure (1393 K, some 13 K over the normal boiling point). Then the power was increased very slowly until the magnesium started to flow. Using the heat of vaporization (128 kJ.mole^{-1})⁶ one can calculate that power fluctuations of 0.1 kW will change the rate of vaporization by $100 \text{ cm}^3\text{s}^{-1}$. The furnace was operating at approximately 20 kW, so it was susceptible to fluctuations of this magnitude. However, for these runs the flow rate appeared to be stable as judged by the agitation of the bath surface. Attempts to operate at flow rates less than $200 \text{ cm}^3\text{s}^{-1}$ failed for this reason.

To attain lower flow rates, argon was used as a carrier gas. This mode of operation was much simpler to control. The temperature controller was set for 1350 K ($P_{\text{Mg}} = 0.8 \text{ atm}$), and the argon flow was commenced.

During the injection period, the bath temperature was monitored with Pt/Pt-Rh thermocouples and maintained at $1523 \pm 15 \text{ K}$. Pin samples were aspirated into quartz tubes, and water-quenched within 5 seconds. The frequency of bubble formation was recorded as often as a sample was taken.

The injection was terminated if the bubbling appeared irregular, or after 1 hour. The melts were held at temperature for an additional hour. The weight loss of the retort during the run was used to calculate the average flow rate of magnesium.

Chemical Analysis

The pin samples were very brittle, and were crushed in a vice. At least 10 pieces were taken at random from the sound portions of the samples. Standard atomic absorption spectrometric methods were used for magnesium, calcium, manganese and silicon analyses. Sulphur and carbon analyses were performed on Leco IR32 and WR12 analyzers, respectively.

RESULTS

The magnesium and sulphur contents obtained in each run were plotted as a function of time. The first of these plots, Figure 5, shows the progress of magnesium dissolution and desulphurization for Run 1 in which there was 7 ppm S and 20 ppm Mg initially. The magnesium content rose uniformly to approximately one-tenth of the saturation level. The sulphur content fell rapidly to 2 ppm, and remained constant thereafter. This was characteristic of runs with less than 50 ppm sulphur. (See Appendix D.) The magnesium declined in the holding period, whereas there was no drop in sulphur content. The predictions were derived from the model developed below.

The highest sulphur level was 0.19% S at the start of Run 11 (Figure 6). In this case the sulphur declined linearly with time. The magnesium content rose from 0.002% to only 0.004% in 12 minutes, and then was reasonably constant until the end of the bubbling. The magnesium content fell in the holding period, whereas the sulphur did not. One can see that almost all of the magnesium was used in desulphurization, and very little in increasing the magnesium content of the bath, whereas the reverse was true for the low-sulphur runs.

The initial sulphur content of Run 12 (Figure 7) was 0.055% S which is in the range of industrial levels. The behaviour is similar in form to that of Run 11.

The flow rate in Run 15 was much higher (Table II). As one can see in Figure 8, the sulphur level dropped linearly with time until 0.004% S was reached, and eventually reached 0.002% S. The magnesium

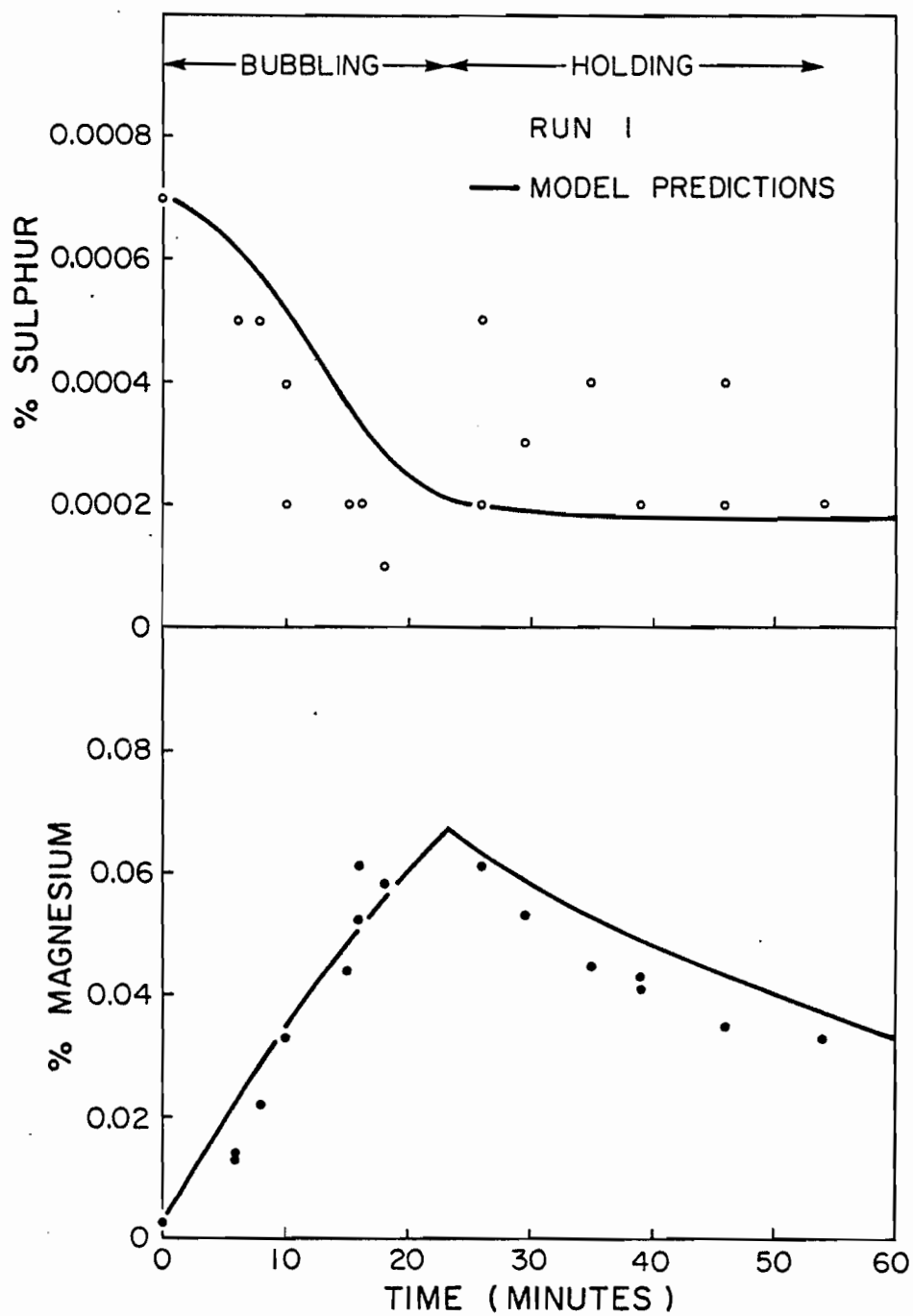


FIGURE 5. Magnesium and sulphur contents as a function of time for Run 1. The curves represent the results of the computer model.

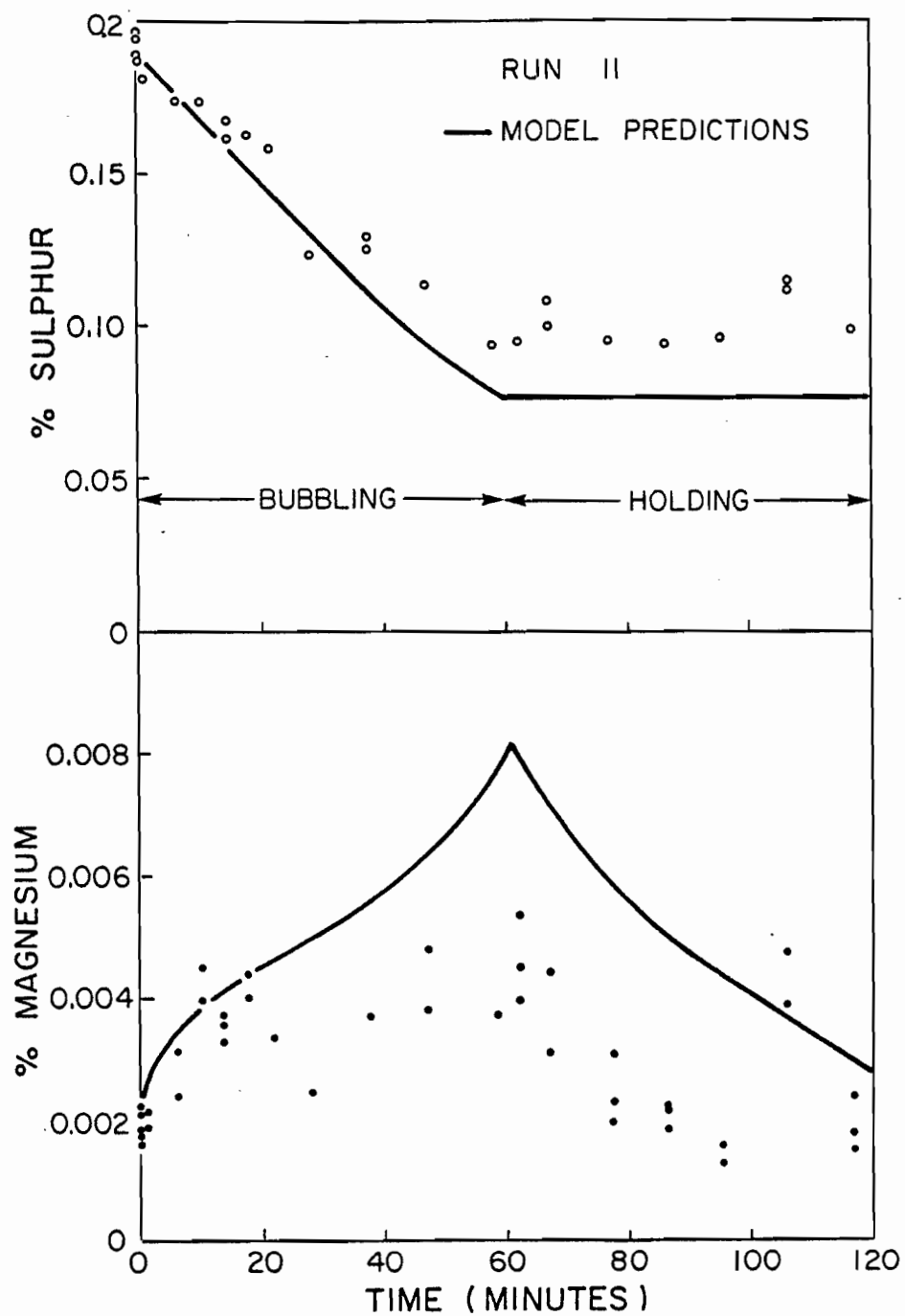


FIGURE 6. Magnesium and sulphur contents as a function of time for Run 11. The curves represent the results of the computer model.

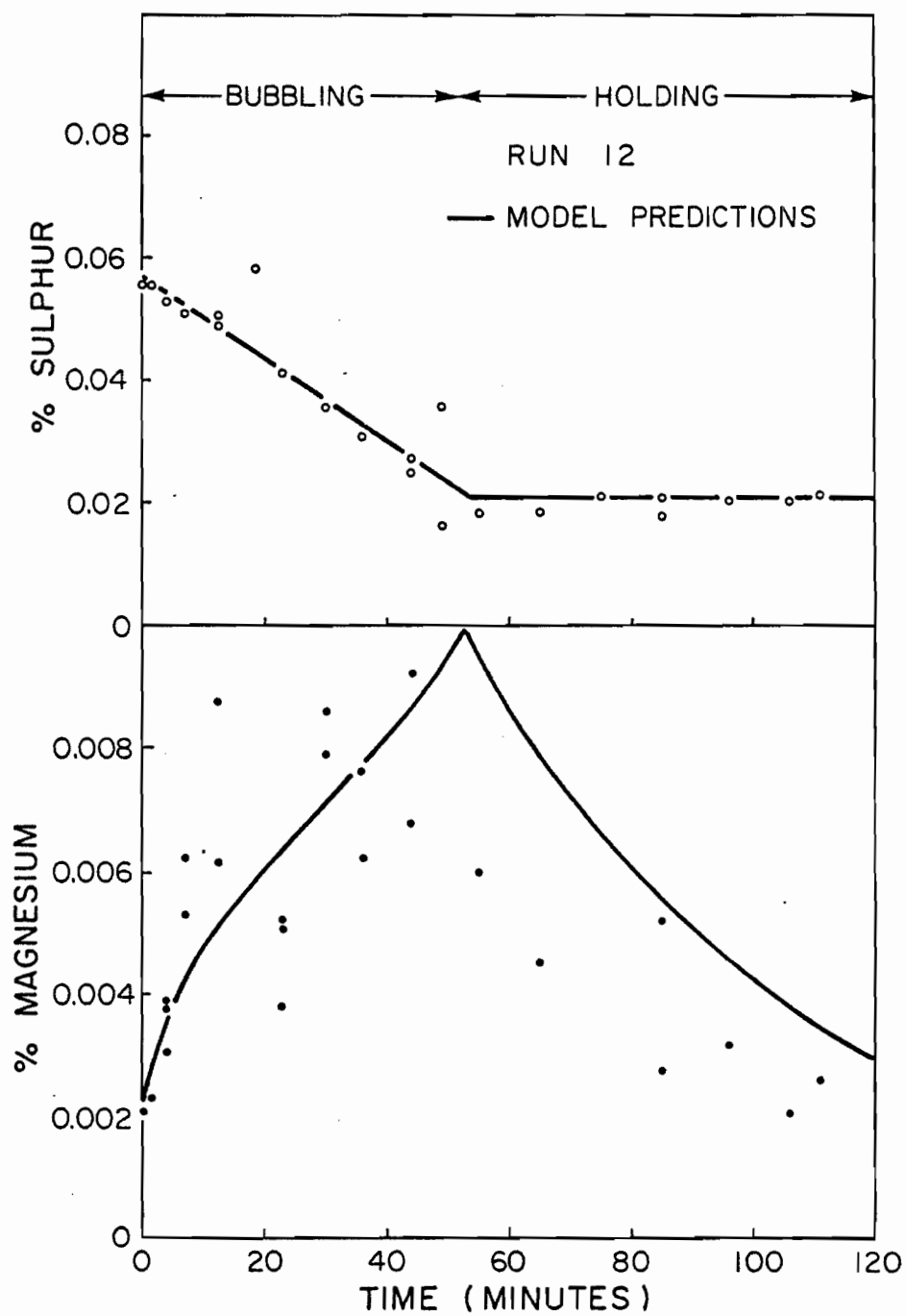


FIGURE 7. Magnesium and sulphur contents as a function of time for Run 12. The curves represent the results of the computer model.

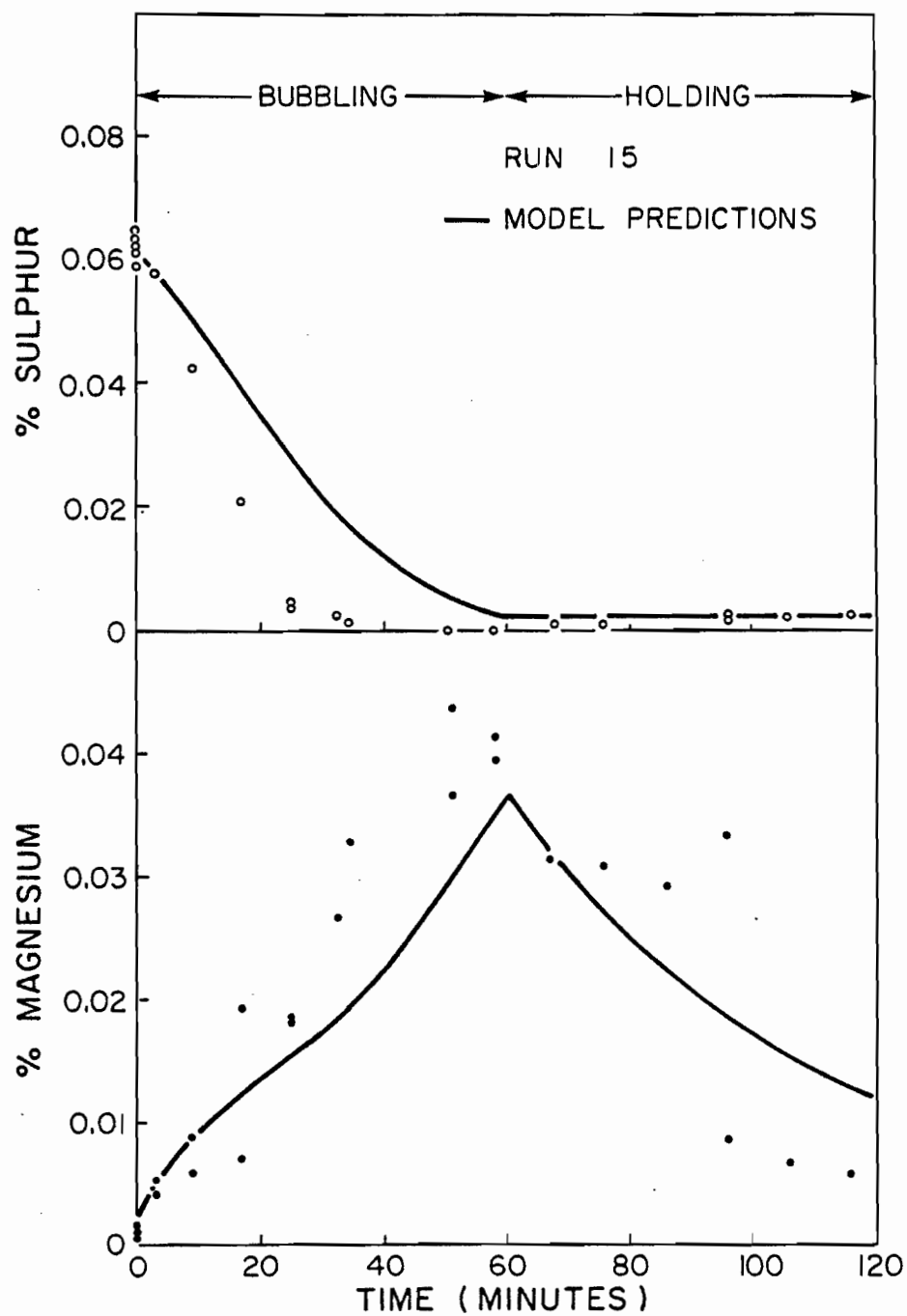


FIGURE 8. Magnesium and sulphur contents as a function of time for Run 15. The curves represent the results of the computer model.

dissolution appeared to start slowly, and then to proceed more quickly to 0.04% Mg. This also showed that magnesium did not dissolve rapidly until the sulphur level was low.

The experimental conditions and the basic results are contained in Table II. Splashing of iron from the crucible was only a significant problem at higher flow rates, where one can see that there was some loss of metal, W_{Fe} , and decrease in the ferrostatic head over the nozzle, h . The flow rates were calculated from the weight loss of the retort, and from the calibrated flow rate of argon.

The desulphurization efficiency is defined as:

$$DSE = 0.76 \Delta \%S / \%Mg_{IN} \quad (45)$$

which only considers magnesium which is involved in direct desulphurization. The magnesium recovery:

$$MR = (\Delta \%Mg + 0.76 \Delta \%S) / \%Mg_{in} \quad (46)$$

also considers magnesium which is dissolved.⁴⁵ From Table II one can see that at low sulphur levels the DSE was low, but at higher sulphur levels it was a major contribution to the total magnesium recovery.

At least 20 bubbles were counted at least 10 times throughout the course of the bubbling. The average of the bubble frequencies for each run is shown in Table II.

Supplementary chemical analysis revealed that there was little other change in the bath chemistry during the runs. The average values are reported in Table III.

TABLE II
EXPERIMENTAL CONDITIONS AND BASIC RESULTS

Run	$W_{Fe} (kg)$		$h (cm)$		Injected Mg(g)	Injection Time (min)	$Q (cm^3 \cdot s^{-1})$		P_{Mg} (atm)	% Mg		% S		Eff(%)		$f_B (s^{-1})$	
	Before	After	Before	After			Mg	Total		Start	End	Start	End	MR	DSE	Measured	Calculated
1	62.2	54.1	13.4	10.2	111.	23.0	381.	381.	1.	0.0020	0.0725	0.0007	0.0002	37.1	0.2	11.8	10.8
2	62.2	54.1	13.4	10.2	89.	32.0	219.	219.	1.	0.0022	0.0800	0.0035	0.0002	52.5	1.6	10.0	10.2
7	64.9	60.9	15.9	14.0	81.	60.0	106.	125.	0.845	0.0020	0.0450	0.0036	0.0002	35.4	2.0	15.6	8.96
11	64.9	60.9	16.5	14.6	66.	59.5	87.6	107.	0.819	0.0020	0.0045	0.1900	0.0950	71.2	68.8	17.4	7.99
12	64.9	64.9	12.7	12.7	31.	52.0	47.0	53.1	0.885	0.0020	0.0090	0.0560	0.0200	72.0	57.3	6.62	5.38
13	64.9	64.9	11.4	11.4	32.	44.0	57.4	76.8	0.747	0.0019	0.0033	0.0560	0.0385	29.8	27.0	14.3	6.80
14	64.9	64.9	10.2	10.2	50.	60.0	60.6	80.0	0.757	0.0018	0.0050	0.0540	0.0225	35.2	31.1	2.11	6.78
15	63.6	59.5	10.8	8.89	140.	60.0	184.	256.	0.720	0.0018	0.0420	0.0624	0.0018	37.9	20.2	10.1	9.87
16	63.6	63.6	23.5	23.5	40.7	60.0	53.6	73.0	0.734	0.0015	0.0041	0.0640	0.0410	31.4	27.3	13.0	6.70

TABLE III
SUPPLEMENTARY CHEMICAL ANALYSIS

<u>Element</u>	<u>% (95% Confidence)</u>
C	4.47 ± 0.25
Si	0.17 ± 0.01
Mn	0.0032 ± 0.0004
Ca	0.0056 ± 0.0003

DISCUSSION

Calculations

The first point to be made is that there was very little magnesium sulphide in the bath at any time. The magnesium and sulphur analyses yielded the total concentration of the analyte, regardless of whether it was present as a compound (such as MgS) or dissolved in the iron matrix. However, one can see that for the high-sulphur runs, the magnesium levels were much lower than the sulphur contents, indicating that little of the sulphur was combined with magnesium. In the holding periods, as discussed below, the decay of magnesium content was the same for all runs regardless of sulphur level. This demonstrated that the decay was due to the vaporization of magnesium, and not to the float-out of inclusions, which has been previously observed to be very fast.⁴³ Total inclusion counts in Runs 15 and 16 revealed approximately 3×10^6 inclusions $\cdot \text{cm}^{-3}$ of $0.8 \mu\text{m}$ diameter which represents at most 0.0003% MgS. As this was an order of magnitude below the total magnesium analysis, it is therefore reasonable to assume that the results of the sulphur and magnesium analyses were essentially the dissolved values.

In the following sections the possible mechanisms of dissolution and desulphurization are discussed and evaluated.

Transport To and From Bubbles

In order to calculate the apparent mass transfer coefficients for magnesium and sulphur at any instant, one must know the total interfacial bubble area in the bath. This was approximated by:

$$A'' = \left(\frac{A_o + A_F}{2} \right) t_R f_B + \frac{A_o}{2} \quad (47)$$

where A_o and A_F were the equivalent areas of an individual bubble at release from the nozzle and at the bath surface, respectively. The product of the rising time, t_R , and the frequency of bubble formation, f_B , is the number of bubbles in the bath at any instant. The second term is the average area of a forming bubble. (Step-by-step calculations are contained in Appendix D.)

Most of the bubble frequencies were close to those predicted by the work with pure argon bubbles,⁴⁴ as shown in Table II. It was difficult to obtain good bubble traces all the time because the vaporizer could not be stopped to adjust the frequency transducer apparatus, as was done in the previous study. Therefore the correlations from the pure argon work⁴⁴ were used to calculate the bubble sizes:

$$D_E = \left[\frac{3\sigma_{GL} D_{no}}{\rho g} N_c'^{0.816} + \left(\frac{9\sigma_{GL}^2 D_{no}^2}{\rho^2 g^2} N_c'^{1.632} + \frac{10 Q^2 D_{no}^2}{g} \right)^{1/2} \right]^{1/3} \quad \text{.....(48)}$$

$$\text{where } N_c' = \frac{4\rho g T_L}{\pi D_{no} D_{ni} P_L} \int_0^{V_c} \frac{dV_c}{T_{V_c}} \quad (49)$$

N_c' is the capacitance group which accounts for the compressibility of the gas in the retort. It was calculated from the freeboard in the retort and was corrected for the temperature variations. Its numerical value varied between 5.4 and 7.8. At the present flow rates the last term predominated, and the bubble size was insensitive to N_c' and σ_{GL} , the interfacial tension for which a value of 1300 dyne.cm⁻¹ was assumed.

The slopes of the magnesium and sulphur versus time curves were obtained graphically, from which the rate of accumulation of dissolved magnesium and the rate of desulphurization were calculated:

$$\dot{N}_{Mg} = \frac{\Delta \%Mg}{\Delta t} \frac{W_{Fe}}{2430} \quad (50)$$

$$\dot{N}_{MgS} = - \frac{\Delta \%S}{\Delta t} \frac{W_{Fe}}{3206} \quad (51)$$

The total rate of gas (argon and magnesium) injection was:

$$\dot{N}_T = Q \frac{P}{RT} \quad (52)$$

Assuming that the bubble pressure and temperature do not change significantly during its rise, and neglecting magnesium evaporation from the bath surface for the moment, the bubble volume at the bath surface was calculated by the principle of conservation of mass:

$$\frac{V_B^F}{V_B^O} = \frac{X_{Ar}^O}{X_{Ar}^F} = 1 - \frac{(\dot{N}_{Mg} + \dot{N}_{MgS})}{\dot{N}_T} \quad (53)$$

Assuming a uniform bubble size for each run, the equivalent areas and total areas were then calculated:

$$A_E = \pi D_E^2 \quad (54)$$

$$= \pi \left(\frac{6V_B}{\pi} \right)^{2/3} \quad (55)$$

The apparent fluxes of magnesium from the bubble, and sulphur to the bubble were then:

$$\dot{N}''_{\text{Mg}} = \dot{N}_{\text{Mg}}/A'' \quad (56)$$

and

$$\dot{N}''_{\text{MgS}} = \dot{N}_{\text{MgS}}/A'' \quad (57)$$

These quantities are plotted as a function of the sulphur content in Figure 9. It can be seen that at low sulphur levels at least 100 times more magnesium dissolved than desulphurized, whereas at the higher sulphur levels approximately 10 times more of it was used for desulphurization than dissolution. However, the total magnesium used was constant, at approximately 8×10^{-6} mole $\text{cm}^{-2}\text{s}^{-1}$.

The apparent magnesium and sulphur liquid phase mass transfer coefficients were:

$$k_{\text{LMg}} = \dot{N}''_{\text{Mg}} / (C_{\text{Mg}}^* - C_{\text{Mg}}^{\text{B}}) \quad (58)$$

and

$$k_{\text{LS}} = \dot{N}''_{\text{MgS}} / (C_{\text{S}} - C_{\text{S}}^*) \quad (59)$$

where C_{Mg}^* was the liquid composition that was in equilibrium with the average bubble composition. The coefficients are plotted in Figure 10 as a function of the sulphur content.

If the mechanism were simply countercurrent diffusion of magnesium and sulphur with MgS forming on the bubble surface, then the mass transfer coefficients for sulphur and magnesium would be identical over the entire range of sulphur*. However, this was not the case, and in fact the apparent sulphur coefficient was generally an order of magnitude greater than that of magnesium. The magnesium mass transfer

* Assuming $D_{\text{LMg}} = D_{\text{LS}}$

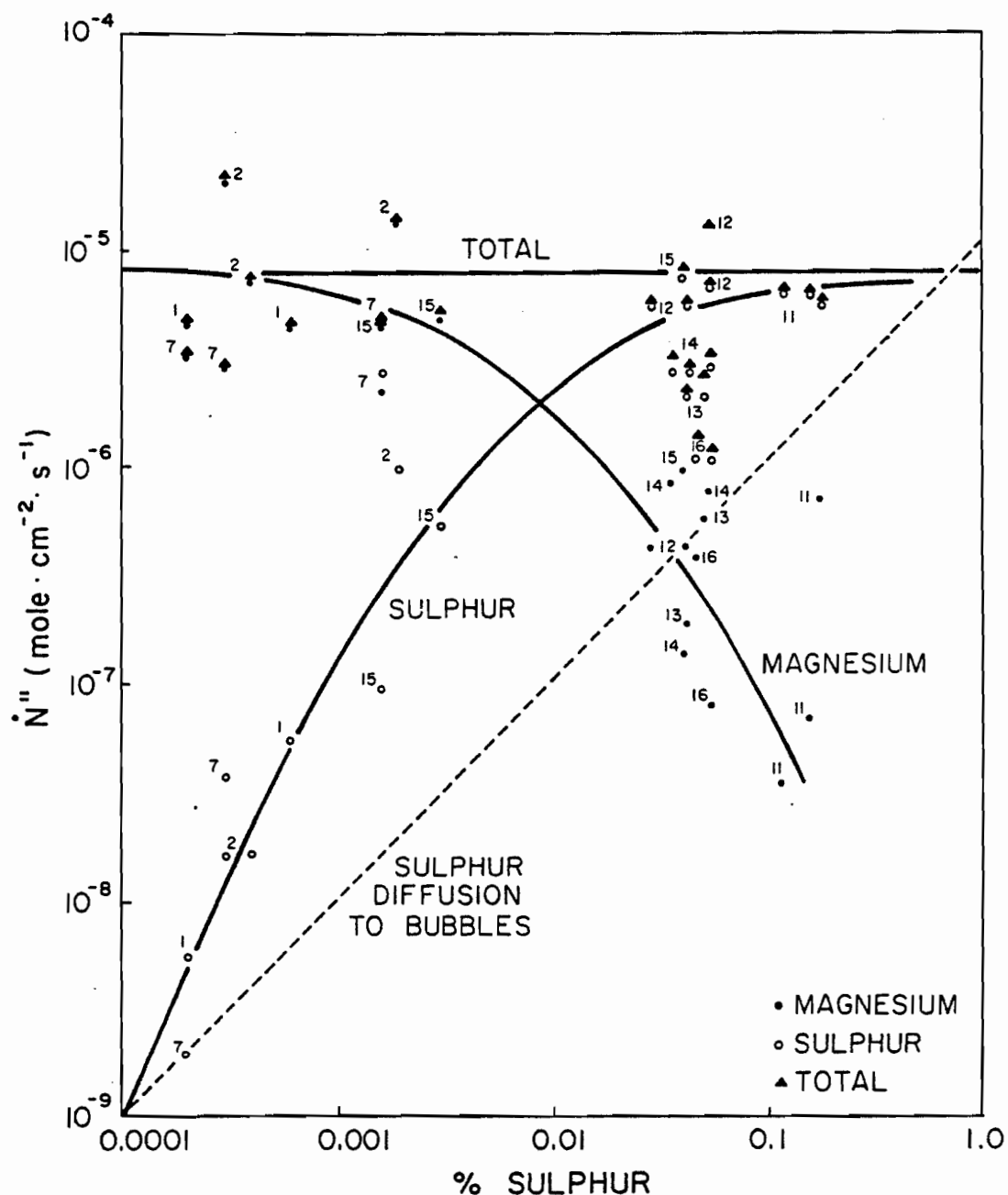


FIGURE 9. The apparent fluxes of sulphur, \dot{N}_{MgS}'' and magnesium, \dot{N}_{Mg}'' to and from the bubble interfaces, respectively, as a function of the sulphur level in the bath. The sum of \dot{N}_{MgS}'' and \dot{N}_{Mg}'' is denoted as the total flux of magnesium which originates from the bubbles. The numbers beside each point are the run numbers. The dotted line represents the amount of sulphur which can diffuse to the bubbles during their rise, as deduced in the text.

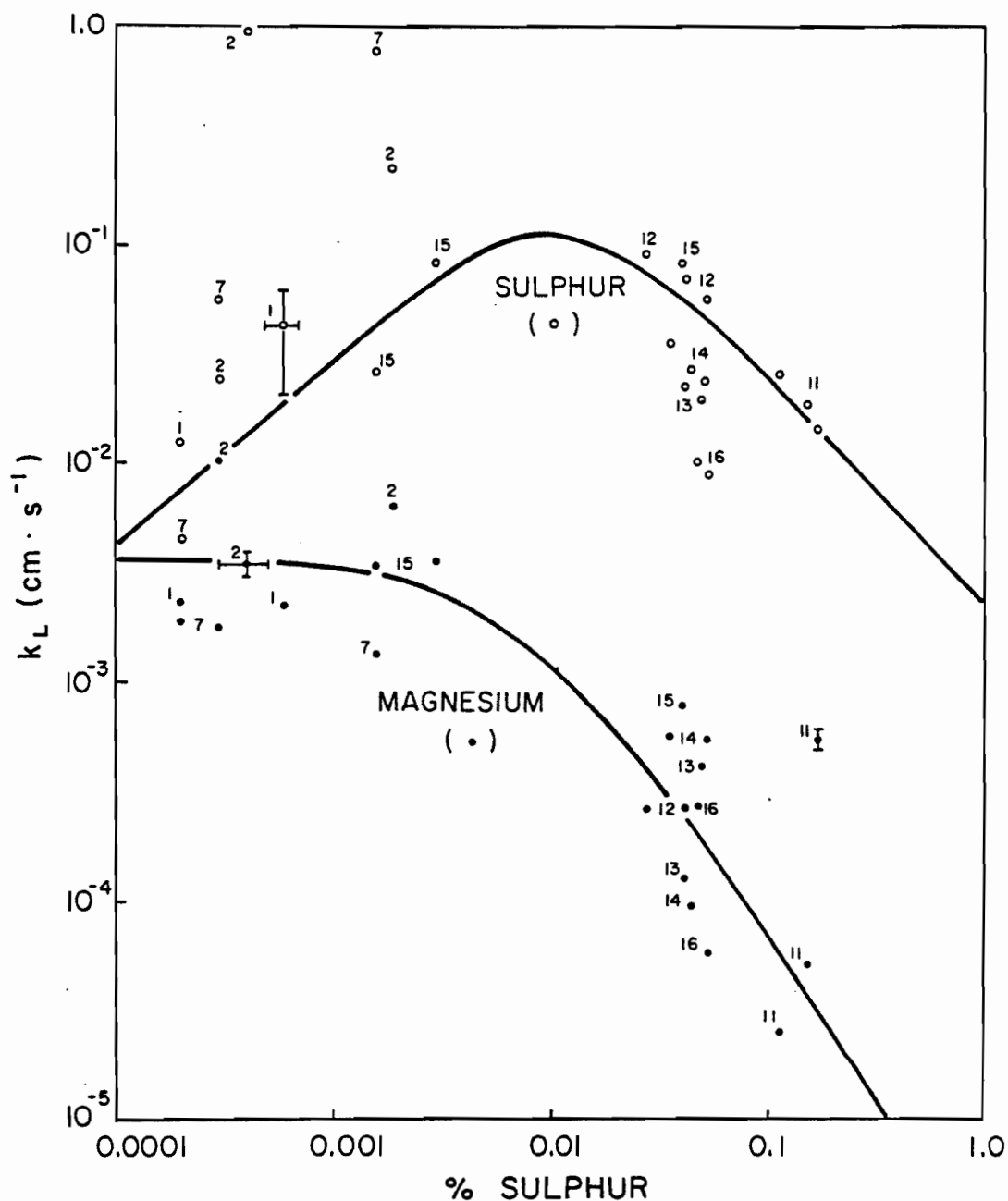


FIGURE 10. The apparent magnesium and sulphur mass transfer coefficients as a function of the sulphur level in the bath. The numbers beside each point are the run numbers. The error bars indicate the estimated error limits on the data. The curves merely show the trends in the data and have no theoretical significance.

coefficient was approximately 0.0035 cm s^{-1} at low sulphur levels, which was even below the value for immobile bubbles of 0.0133 cm s^{-1} (obtained from Equations (19) and (20) with estimates of 2.5 cm and $3 \times 10^{-5} \text{ cm}^2 \text{ s}^{-1}$ for D_E and D_{LMg} , respectively). The sulphur coefficient exceeded the mobile interface coefficient of 0.0214 cm s^{-1} (from Equations (15) and (19) for $D_{LS} = 1.5 \times 10^{-5} \text{ cm}^2 \text{ s}^{-1}$ 46,47).

Two sorts of enhancement of the sulphur coefficient have been postulated. The first is one of interfacial turbulence which has been demonstrated in a liquid metal system by Barton and Brimacombe⁴⁸. These investigators jetted pure oxygen onto an inductively-stirred bath of copper. A copper oxide patch formed directly under the lance, and they measured very high rates of surface movement, induced by the gradient of surface tension across the surface. The measured rate of oxygen transfer was 36 times that measured in silver (which does not spread), and was also greater than that predicted by Equation (21) for inductive stirring. The essential feature of this effect was that a surfactant concentration gradient was established along the interface. In the present situation, the surfactant (sulphur) was available to the entire bubble surface by diffusion through the boundary layer. Thus no significant surface tension gradients were envisioned.

The second mechanism for enhancement of sulphur transfer could have been MgS formation in the boundary layer, similar to the enhanced vaporization of iron in the presence of oxygen.⁴⁹ This problem has been solved^{50,51} for a gas dissolving through a planar interface and reacting instantaneously and irreversibly with another solute. For the present situation this amounted to unrestricted homogeneous nucleation

of MgS. The solution was easily adapted to bubbles by using the penetration theory, Equation (16). If one also assumes for simplicity that $D_{LMg} = D_{LS}$, then the solution in the absence of any sulphur is:

$$\dot{N}_{Mg}'' = 2C_{Mg}^* (D_L/\pi t_{EX})^{1/2} \quad (60)$$

which is the same as the penetration theory predicts. In the presence of sulphur, the magnesium flux is increased to:

$$\dot{N}_{Mg}'' = 2(C_{Mg}^* + C_S^B) (D_L/\pi t_{EX})^{1/2} \quad (61)$$

For the present conditions the enhancement of the magnesium flux would not have been very noticeable, since C_{Mg}^* was generally much greater than C_S^B . With no magnesium dissolution

$$\dot{N}_{MgS}'' = 2C_S^B (D_L/\pi t_{EX})^{1/2} \quad (62)$$

so that the enhanced k_{LS} arises from the difference between Equations (60) and (61). Therefore the enhanced mass transfer coefficient is:

$$k_{LS} = 4 (D_L/\pi t_{EX})^{1/2} \quad (63)$$

or approximately 0.04 cm s^{-1} , over the whole sulphur range. This was not the case as seen in Figure 10. Nor does this hypothesis explain why the magnesium transfer coefficient was so low.

The assumption of an instantaneous reaction is unrealistic, since MgS is a separate phase which has to be nucleated. Therefore one would expect that a critical supersaturation in the boundary layer must exist before any enhancement could occur. From examination of Figure 10, one can see that the sulphur coefficient increased, even from the lowest sulphur levels (0.0002% S). There cannot possibly be any supersaturation in this case, because conditions were below the equilibrium curve in Figure 1. It is concluded that enhancement of the sulphur rate by homogeneous nucleation in the boundary layer cannot explain the present results.

It appeared that the observed rate of desulphurization was too high to be explained by transport of sulphur to the bubble interface. From Figure 9, it can be seen that the total rate of magnesium utilization, that is, $\dot{N}''_{\text{Mg}} + \dot{N}''_{\text{MgS}}$ was reasonably constant over the entire sulphur range. This indicates that magnesium diffused into the liquid regardless of the sulphur level, and reacted with sulphur (either homogeneously or heterogeneously) away from the bubble. For simple countercurrent diffusion of magnesium and sulphur, the magnesium flux would always have been greater than that of sulphur because the driving force was so much greater: 0.7% Mg at the bubble surface compared to at most 0.19% S in the bulk. If sulphur had the same mass transfer coefficient as magnesium, then the portion of the desulphurization due to reaction at the bubble interface would have been:

$$\dot{N}'' = 0.0035 C_S \quad (64)$$

which is shown in Figure 9. This accounts for about one-tenth of the observed rate of desulphurization.

The magnesium mass transfer coefficient was 0.0035 or 0.0046 cm s^{-1} when evaporation from the bath surface was considered (see Appendix D). This value was close to 0.00621 cm s^{-1} for transfer over the front of an immobilized spherical-cap bubble (Equation (20)). When the rear transfer is included (Equation (19)), the total transfer coefficient should be 0.0133 cm s^{-1} ; however, this estimate is an upper limit to the transfer coefficient. Apparently, some phenomenon was responsible for reducing the transfer rate from that of a mobile interface to that of an immobile one.

The influence of sulphur or magnesium sulphide on the bubble interface is an unlikely possibility as the total transfer coefficient remained constant over the entire sulphur range. Oxygen was not present in large concentrations in the melt (less than 0.002% O)⁴⁴ and is therefore unlikely as well. Furthermore, magnesium reacts with oxygen and sulphur, so it could not have been a simple case of Langmuir adsorption. One can speculate that the magnesium vapour held the sulphur activity in equilibrium with it, at 0.5 ppm S (using K_3). The sulphur surface coverage θ_S , would then have been 0.09, using a value of 1972 for K_S ³⁰ in Equation (26). Magnesium reacts even more strongly with oxygen, so the oxygen coverage would have been much less under similar assumptions.

Magnesium has all the characteristics of a physical adsorbate (Table I); furthermore it has a high heat of condensation (128 kJ mole^{-1}), so strong physical adsorption may be postulated. There is one study⁵² which indicates that magnesium is surface active, even in the presence

of large sulphur concentrations. This suggests that there may be some excess of magnesium at the interface between the iron and the almost pure magnesium bubbles. The effect that physical adsorbates have on mass transfer in metallic systems is unknown, but it is possible that they could immobilize the interface as is the case with some surfactants in aqueous systems.

Gas Phase Control

As seen in Figure 9, there was no significant difference between Run 1, with pure magnesium and Run 7, with the addition of a carrier gas. However, the data from Run 2, also with pure magnesium, was somewhat higher. In fact, the highest point for Run 2, 2.1×10^{-5} mole $\text{cm}^{-2}\text{s}^{-1}$ at 0.0002% S is probably in error, since the calculations in Appendix D show that when evaporation from the surface is included, the amount of magnesium used was greater than that injected. The conclusion is that within the rather large limits of experimental error, there was no difference between runs with pure magnesium and ones with up to 30% dilution with argon.

Following the analysis presented in the previous work, K_H (Equation (24)) is 255 for magnesium dissolving in iron. Using estimates of $3.04 \text{ cm}^2\text{s}^{-1}$ for the diffusivity of magnesium in argon from the Chapman-Enskog Theory⁵³ and $3 \times 10^{-5} \text{ cm}^2\text{s}^{-1}$ for the diffusivity of magnesium in liquid iron⁵, Equation (25) can be used to estimate the ratio of mass transfer coefficients:

$$\frac{k_g}{k_L} = \left(\frac{D_G}{D_L}\right)^{1/2} = 318 \quad (65)$$

Using Equation (23) the overall or mixed mass transfer coefficient should then be

$$\begin{aligned} k_{LOV} &= \left(1 + \frac{255}{318}\right)^{-1} k_L \\ &= 0.555 k_L \end{aligned} \quad (66)$$

Thus, this analysis predicts that with just the smallest addition of argon, the mass transfer coefficient should drop by 45%. The assumption of rigid bubbles would further widen the gap between liquid and mixed control. Since the random error in the mass transfer coefficient (74%), was greater than this predicted reduction, it is not certain whether or not the argon had a controlling effect.

Homogeneous Nucleation

As the previous work indicates, the rate of homogeneous nucleation is an exponential function of the supersaturation. For the present experiments the rate of desulphurization was plotted in Figure 11 as a function of the % Mg . % S in the iron. One can see that the rate increased in proportion to % Mg . % S at the higher rates, but dropped drastically as $8 \times 10^{-6} (\%)^2$ was approached. This value is even slightly below the equilibrium K_3 value of $3.2 \times 10^{-5} (\%)^2$ recalculated from Speer and Parlee's⁴ data. Therefore, it appears that no supersaturation was required for desulphurization. At higher supersaturations, a regression on the data yielded:

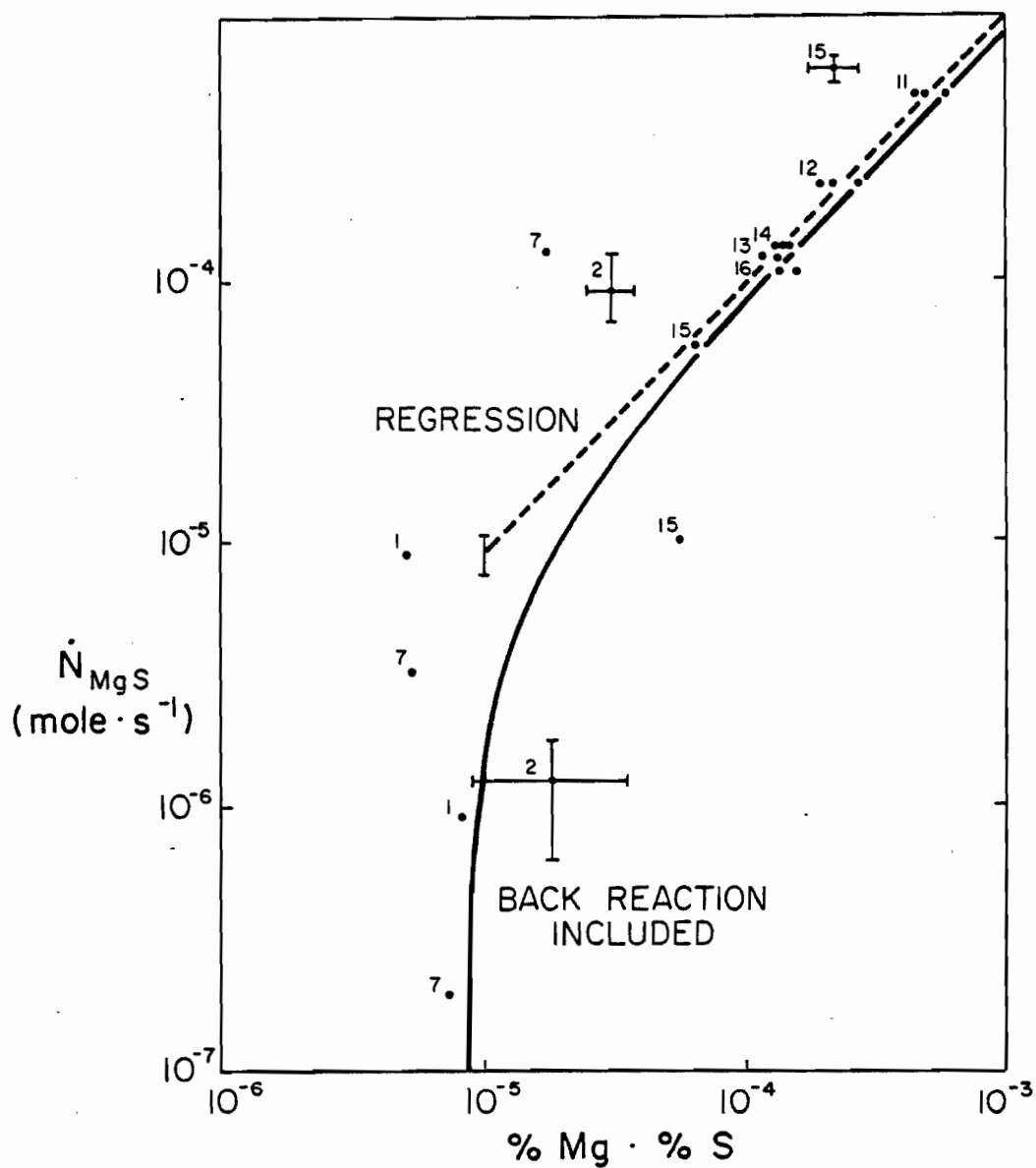


FIGURE 11. The rate of magnesium sulphide formation for the whole bath as a function of the product of the magnesium and sulphur contents in the bath. The numbers beside each point are the run numbers. The error bars indicate the estimated accuracy of the data. The dotted line represents the regression on the data (Equation (67)). The curved line represents Equation (79) fitted to the experimental data.

$$\dot{N}_{\text{MgS}} = 1.325 (\% \underline{\text{S}} \cdot \% \underline{\text{Mg}})^{1.036 + 0.072} \quad (67)$$

which is well approximated by:

$$\dot{N}_{\text{MgS}} = 0.92 (\% \underline{\text{S}} \cdot \% \underline{\text{Mg}}) \quad (68)$$

$$\text{Thus } \frac{dC_s}{dt} = \frac{\dot{N}_{\text{MgS}}}{V_T} = k C_{\text{Mg}} C_S \quad (69)$$

where k is the apparent second order rate constant, numerically equal to $17.1 \text{ cm}^3 \text{ mole}^{-1} \text{ s}^{-1}$. This linear behaviour was definitely not the exponential dependency expected from homogeneous nucleation theory. Therefore, this mechanism can be rejected.

Heterogeneous Desulphurization

If the reaction were simply controlled by diffusion to nucleation sites such as inclusions, then it should be first order with respect to the least abundant species. Accordingly, the rate of desulphurization was plotted as a function of % Mg and % S in Figure 12, and no such dependency was observed. Very approximately, one could say that

$$\begin{aligned} \dot{N}_{\text{MgS}} &= 0.05\% \underline{\text{Mg}} \\ &= 1.44 \times 10^{-4} C_i \end{aligned} \quad (70)$$

(However, the results of Run 11 do not support this contention.) The rate of diffusion in this inductively-stirred melt can be conservatively

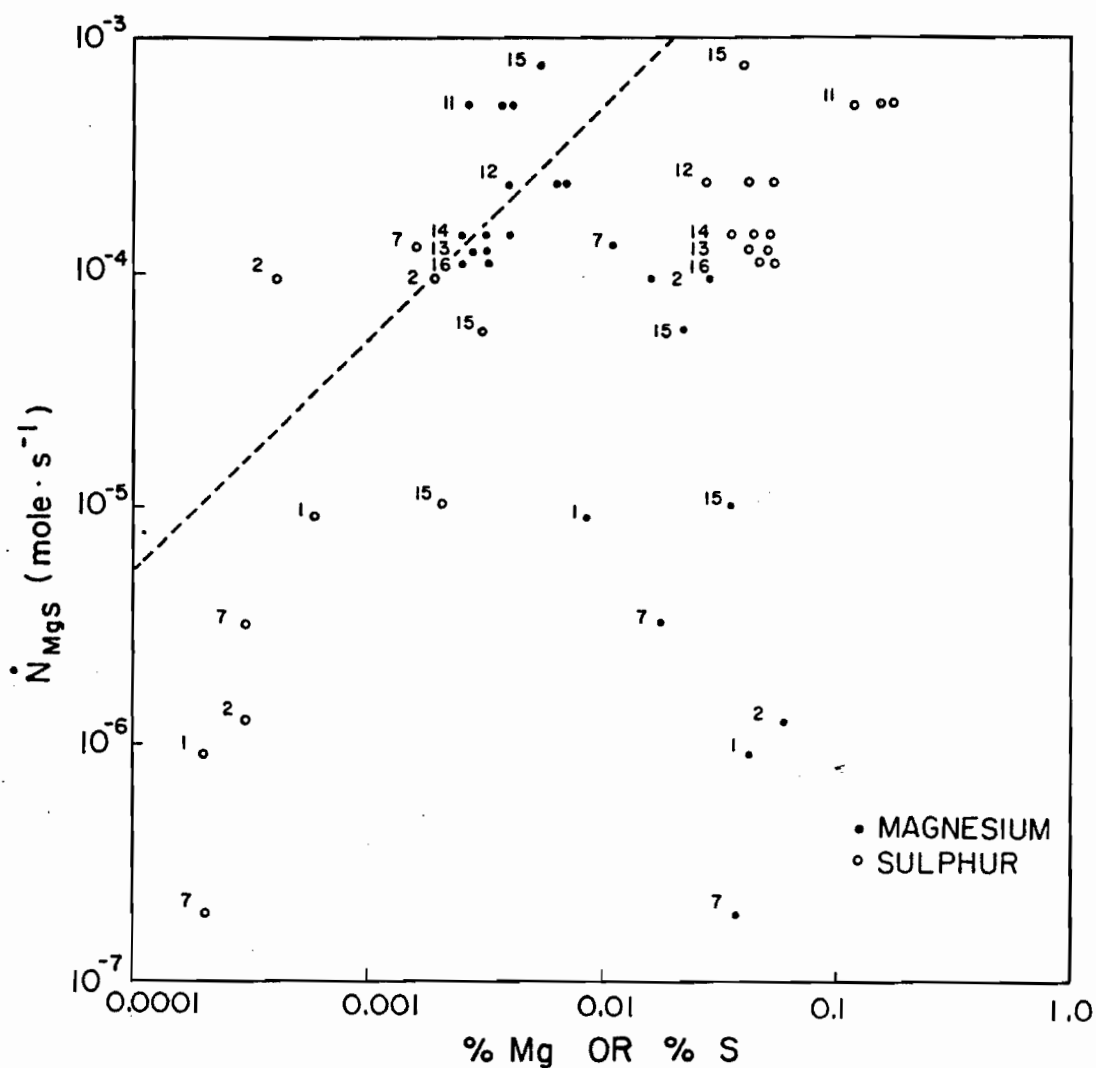


FIGURE 12. The rate of magnesium sulphide formation for the whole bath as a function of the dissolved magnesium and sulphur levels. The numbers beside each point are the run numbers. The dotted line represents an attempt to find a first-order dependency of the rate on the concentration of the least abundant species. See the text for the significance of this behaviour.

estimated by assuming only radial diffusion to the particles. From metallography, approximately 3×10^6 inclusions cm^{-3} of 0.8×10^{-4} cm diameter were counted for runs 15 and 16. Therefore, the diffusion-controlled precipitation rate would be:

$$\begin{aligned} \dot{N}_{\text{MgS}} &= 4\pi D_L V_T r_I n (C_i - C_{\text{EQ}}) \\ &= 388 (C_i - C_{\text{EQ}}) \end{aligned} \quad (71)$$

which is approximately 10^6 times faster than observed. Thus transport to the sites was not limiting.

Proposed Mechanism of Desulphurization

Since the desulphurization appeared to be a second-order reaction, and occurred more slowly than transport to the sites, one might suspect that some sort of chemical control governed the desulphurization kinetics. Further, it is clear from the above discussion that homogeneous nucleation could not have accounted for the experimental behaviour. The following model is now advanced to provide an interpretation of the results.

It is proposed that the magnesium and sulphur atoms, dissolved in the bath, must come into contact with one another by random collisions according to the Kinetic Theory of Gases or according to the Theory of Absolute Rates of Reaction. At such high temperatures, with such a strong free energy of formation, MgS "germs" should form. Germ is the term used in the homogeneous nucleation literature to describe a cluster

of atoms smaller than the critical nucleus.³² These germs would not gain enough free energy from the reaction to nucleate a new phase homogeneously. They would still be coherent in the iron matrix.

It was observed metallographically that there were a large number of inclusions in the bath ($3 \times 10^6 \text{ cm}^{-3}$), and that they were very small ($0.8 \mu\text{m}$). However, they are much larger than germs which are only 2 atoms in size. These inclusions are postulated to arise from the fact that about one-tenth of the desulphurization occurs at the bubble interface, as described earlier. If some of this MgS is stripped from each bubble as it rises, and MgS particles are continuously being eliminated from the bath by induction stirring, a steady-state number of inclusions could arise. It must be remembered that the observed inclusion count represents only 3 ppm MgS in the bath. It is postulated that the germs were eliminated by diffusion to the inclusions.

From the Theory of Absolute Rates of Reaction it is possible to calculate the "equilibrium" activity of this germ:



which has an equilibrium constant

$$K_\ddagger = \frac{a_\ddagger}{a_{\text{Mg}} a_{\text{S}}} \quad (73)$$

$$= \frac{F_\ddagger}{F_{\text{Mg}} F_{\text{S}}} e^{-E_0/RT} \quad (74)$$

$$= 60 e^{-e_0/RT} \text{ cm}^3 \text{ mole}^{-1} \quad (75)$$

The F 's are the molecular partition functions which have been approximated⁸ to evaluate K_{\ddagger} . As previously explained, the activation energy term can be neglected. The Theory of Absolute Rates says that the rate of reaction is then governed by one specific vibration by which the complex decays to the product. In the present situation, it cannot be this simple because a new phase must be nucleated. K_{\ddagger} is in effect a "kinetic" equilibrium constant which permits atoms to react when it is thermodynamically favourable. Thus the back reaction in Equation (72) would be expected to occur close to the thermodynamic equilibrium, K_3 . Therefore the activity of the germs would be:

$$a_{\ddagger} = K_{\ddagger}(a_{\text{Mg}}a_{\text{S}} - K_3) \quad (76)$$

$$= 60(a_{\text{Mg}}a_{\text{S}} - K_3) \text{ mole cm}^{-3} \quad (77)$$

The rate of diffusion to the sites is then given by Equation (44)

$$\frac{dC_{\text{S}}}{dt} = 4\pi D_{\text{L}}r_{\text{I}} n a_{\ddagger} \quad (78)$$

$$= 2.71(a_{\text{Mg}}a_{\text{S}} - K_3) \text{ mole cm}^{-3}\text{s}^{-1} \quad (79)$$

The calculated rate constant is then within an order of magnitude of the experimental value of $17.1 \text{ cm}^3 \text{ mole}^{-1}\text{s}^{-1}$. Considering the uncertainties associated with the Theory of Absolute Rates, the estimation of partition functions, the diffusivity of the germs and the number of sites, the agreement could be fortuitous. Nevertheless, the major

strength of this mechanism is that it provides an explanation for the observed second-order behaviour, by assuming that a "chemical" step is at equilibrium. This is then followed by a controlling, transport step. Generally, at such high temperatures, chemical reactions are thought to occur very rapidly, and thus can be considered as being at equilibrium, leaving transport to control the rate.⁵⁴

When Equation (79) is fitted to the data in Figure 10, the apparent value of $\log K_3 = -5.10 \pm 0.45$ (1 standard error of estimate) which is only slightly below the value recalculated from Speer and Parlee's data ($\log K_3 = -4.5 \pm 0.19$) shown in Figure 1. When both sets of data are incorporated, $\log K_3 = -5.05 \pm 0.31$ and $e_{\text{Mg}}^{\text{Mg}} + e_{\text{S}}^{\text{Mg}} = -3.23 \pm 0.41$, as shown in Figure 1.

Since these experiments were carried out on the hypereutectic liquidus of the iron-carbon system, graphite nuclei would have been present. However, it is difficult to consider them since their numbers and temperature sensitivity are unknown.

Model Predictions

The present mechanism was developed on the basis of instantaneous rates of dissolution and desulphurization at various times through the experiments. It is useful to confirm that the model can "predict" the course of the experiments. A computer simulation (Appendix E) was devised in which N_T moles of magnesium were injected (based on the volumetric flow rate) over a small time increment, Δt (generally 12 seconds). Magnesium was allowed to dissolve according to the experimentally determined mass transfer coefficient

$$N_{Mg} = k_L A'' (C_{Mg}^* - C_{Mg}) \Delta t \quad (80)$$

Also, during this time increment, desulphurization occurred according to

$$N_{MgS} = 17.1 V_T C_{Mg} C_S \Delta t \quad (81)$$

The number of moles of sulphur and magnesium were used to calculate the new bath composition, and the process was repeated. The magnesium recovery (MR) and desulphurization efficiency (DSE) were also calculated. The results of the simulations together with the experimental results are shown in Figures 5 to 8. The high initial rates of magnesium dissolution in the high-sulphur runs can be easily understood now: initially the $C_{Mg} C_S$ product was low, so that desulphurization was slow, and most of the magnesium dissolved. This increased the product, and the desulphurization proceeded more quickly, until most of the magnesium was consumed in desulphurization. This behaviour provided good evidence for the second-order reaction. It is also instructive to plot the "reaction paths"; that is, % Mg versus % S as shown in Figure 13. One can see the same phenomenon again, that is, that initially the curve was almost horizontal. Following the progression of the curve from left to right, it is clear that the greater the supersaturation, the greater the desulphurization and the more vertical the curve becomes. If the desulphurization is continued (as in Run 15), the sulphur becomes depleted, the % Mg . % S product falls and desulphurization slows down. At this point more magnesium is consumed in dissolution and the DSE drops.

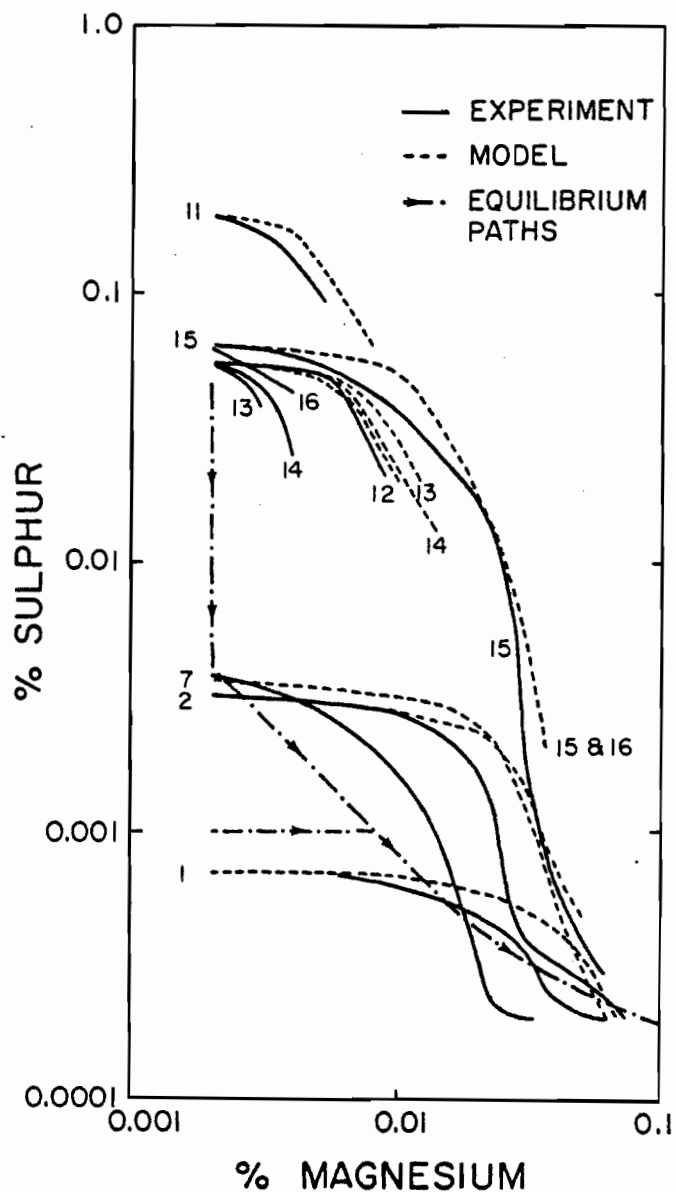


FIGURE 13. The progress of desulphurization plotted as a function of the magnesium content of the bath for each run. These are known as "reaction paths". The predictions based on the model are also shown with the corresponding run number. The "equilibrium reaction paths" are shown as well for two typical cases: one starting above the equilibrium line, and the other below the equilibrium.

The predicted and observed reaction paths are very different from the equilibrium paths, also shown in Figure 13, which assume instantaneous reaction. Above the equilibrium line, MgS precipitates and the path is vertical until the equilibrium line is reached. Then the reaction path moves along the equilibrium line. Starting below the equilibrium line, magnesium dissolves without any desulphurization, until the equilibrium line is reached, and then the path is along the equilibrium line. Equilibrium reaction paths actually correspond to infinitely high k values.

When magnesium evaporation and/or desulphurization at the bubble interface were incorporated into the model they were found to have little effect. In runs 13, 14 and 16, the simulations were not very good because the rate of magnesium dissolution was much below the predicted value. This was attributed to observed leaks in the retort. Mg_3N_2 and MgO nodules formed on the outside of the retort at the leak. Evidently, the weight compensation for this loss was insufficient. The desulphurization was still second-order in these runs as seen in Figure 11, despite the low rate of addition.

Holding Periods

As in the previous studies,^{5,24,25} the rate of magnesium evaporation (Figures 5-8) was described very well using a mass transfer coefficient of $0.00881 \text{ cm s}^{-1}$, from Machlin's equation (Equation (21)). The vaporized magnesium probably reacted with the atmosphere to form Mg_3N_2 or MgO. No loss of carbon, silicon, manganese or calcium was detected in the holding periods. The sulphur levels did not decrease

between the FeS plunges and the magnesium injection, or during most of the holding periods. (In Run 16, 0.002% S was lost over this period.) It is thought that the vapour pressure of the other elements in solution was low enough that they would have vaporized less rapidly than magnesium, and hence have been controlled by the rate of vaporization.⁵⁵

The fact that the sulphur levels did not decline in the holding periods was consistent with the present hypothesis for the mechanism of desulphurization. Since no magnesium bubbles were injected during the holding periods, there was no source of nucleation sites and consequently, there was no desulphurization, despite the fact that there was generally some MgS supersaturation above the K_3 equilibrium.

Experimental Error

The most difficult experimental aspect of this work was the vaporization of magnesium. A run was terminated or rejected if the bubbling appeared to be erratic. From previous work on pure argon bubbling,⁴⁴ this author was able to see the effect of flow rate on the agitation of the bath surface. It was difficult to detect visually changes in flow rate of less than $\pm 20\%$, this therefore being the random error in the magnesium flow rate during a run. The systematic error in the average flow rate was approximately $\pm 10\%$, stemming mainly from errors in weighing the retort.

As mentioned above it was difficult to obtain good traces of the bubble frequency with the present apparatus, so the bubble volume correlations from the argon work were used.⁴⁴ In that study, the random error in the present flow rate range was $\pm 50\%$ in frequency and therefore in bubble volume as well.

The error in the magnesium atomic absorption spectrometric analysis, judged by the repeatability of the standards, was approximately $\pm 15\%$, whereas duplicate analyses were generally within $\pm 10\%$. Sulphur analyses were accurate to $\pm 5\%$, the maximum deviation from U.S.A. National Bureau of Standards materials. However, for less than 100 ppm S, the accuracy of the Leco IR 32 analyzer was ± 3 ppm.

From these primary sources of error it was possible to determine the resulting errors in calculated values. A $\pm 50\%$ error in bubble volume would have resulted in a $\pm 65\%$ error in A'' , the total bubble area in the bath. Coupling this with the worst possible errors in other variables, the mass transfer coefficient, k_L would be accurate to only $\pm 100\%$ (including systematic errors). At 95% confidence, the average experimental mass transfer coefficient (including the evaporation correction) was $0.00458 \pm 0.00337 \text{ cm s}^{-1}$ which represented a $\pm 74\%$ random error.

The second order rate constant was found to be a "bulk" property; hence the major error was a random one from run to run at the high sulphur levels. At lower sulphur levels, the error in sulphur analysis became important, as shown by the large error bars in Figure 11. Consequently, only the higher sulphur values were used in the regression. The value of k was $17.1 \pm 6.7 \text{ cm}^3 \text{ mole}^{-1} \text{ s}^{-1}$ at 95% confidence.

The value of $\log K_3$ was simply the average value of $\% \text{ Mg} \cdot \% \text{ S}$, for N_{MgS} less than $10^{-5} \text{ mole s}^{-1}$ in Figure 11. Within one standard error of estimate, $\log K_3 = -5.10 \pm 0.45$. When Speer and Parlee's⁴ data is included $\log K_3 = -5.05 \pm 0.31$.

Industrial Implications

Hot metal from the blast furnace generally contains 0.01 to 0.06% S, and steel specifications generally require that the higher contents be reduced by external desulphurization. For hot metal containing approximately 1% Si at 1700 K, the equilibrium solubility (K_1) would be approximately $0.3\% \text{ Mg atm}^{-1}$, which is lower than in the present study. Most injection methods create bubbles that are at least 50% magnesium. For simple counter-current diffusion of magnesium and sulphur (with the same mass transfer coefficient) the ratio of the fluxes is denoted as:

$$\alpha = \frac{C_{\text{Mg}}^*}{C_{\text{S}}^{\text{B}}} = \frac{K_1 P_{\text{Mg}}}{0.76\% \text{ S}} \quad (82)$$

where 0.76 is the stoichiometric factor. One can see that α will generally be greater than 5, so that much more magnesium is expected to dissolve, than sulphur to diffuse to the bubble interface. This was the case in the present experiments. One can define another parameter β

$$\beta = \frac{-\Delta\% \text{ Mg}}{0.76\Delta\% \text{ S}} \quad (83)$$

which relates the observed drop in sulphur to the increase in magnesium. If the mechanism were simply counter-current diffusion with desulphurization occurring only at the interface, then α should equal β . As one can see in Table IV this is not the case, and desulphurization must occur in the liquid. Additionally, these β values show that considerable amounts of magnesium dissolve without directly desulphurizing the iron.

TABLE IV
COMPARISON WITH MAGNESIUM DESULPHURIZATION PRACTICE

Method	Bath wt (Kg)	Flow Rate $\text{cm}^3 \cdot \text{s}^{-1}$	Treat- ment Time (min)	% S		% Mg			α	β	MR %	DSE %	Apparent $k(\% \text{ Mg} \cdot \text{min})^{-1}$	Author
				Start	Finish	Start	Finish	Added						
MAG-COKE	10^5	10^7	8	.025	.006	-	.018	.124	25.	1.2	26.	12.	24.	Duquette <u>et al</u> ⁵⁶
Mg wire	250	10^5	8	.05	.01	.002	.02	.15	10.	0.6	32.3	20.2	25.	Ashton <u>et al</u> ⁴⁵
Mg vapour Run 12	65	53.	52.	.055	.02	.002	.009	.048	9.	0.3	71.	56.	3.	present

Few studies report magnesium residuals, and only the two^{45,56} in Table IV contain enough information to permit such calculations.

The larger-scale systems appear to behave in a similar manner to the present system, in that the desulphurization does not occur at the bubble interface. An estimate of the apparent second-order rate constant can be made by considering the rate equation

$$\frac{d\% S}{dt} = -k \% Mg \cdot \% S \quad (84)$$

In the large-scale experiments, the average final $\% Mg \cdot \% S$ was a constant: 10^{-4} and 2×10^{-4} for Duquette et al.⁵⁶ and Ashton et al.,⁴⁵ respectively. The rate constant was then the average rate of desulphurization divided by the concentrations of magnesium and sulphur along the reaction path line. These values are an order of magnitude greater than the present experimental one of $2.95(\% Mg \min)^{-1}$ as shown in Table IV. This discrepancy can be rationalized in terms of the proposed model, in which MgS embryos are formed by random collision and then diffuse to heterogeneous sites. The increased turbulence at higher flow rates could increase the number of MgS sites stripped from the bubble interface and/or increase the mass transfer to these sites.

Petrushka et al.^{57,58} have developed the "lime-mag" process for desulphurization. Powdered lime and magnesium are injected with a carrier gas. The increased efficiency of this process may be in part due to the lime providing extra nucleation sites, as well as itself reacting with sulphur. Lindborg and Torssell⁵⁹ have also suggested powder injection, but this was to enhance inclusion flotation.

Secondary desulphurization, that is, a further decrease in the sulphur level between the desulphurization station and the melt shop, has often been observed.⁵⁶ This has been attributed to the slow rise of MgS inclusions formed during treatment. It is also possible that the reaction continues on rising MgS inclusions or kish graphite. In Treadwell cars and ladles there is much less stirring, so that inclusions take much longer to rise than in small inductively-stirred crucibles.⁴³

The magnesium consumption required to reach various sulphur levels is shown in Figure 14. There is reasonable agreement among all the studies, when one considers the great range of reported flow rates and other conditions. This is because the magnesium recoveries are all of the same order of magnitude. The large increase in consumption below 0.01% S is a result of increased magnesium dissolution. This is consistent with the "cross-over" of dissolution and desulphurization fluxes at 0.01% S in Figure 9.

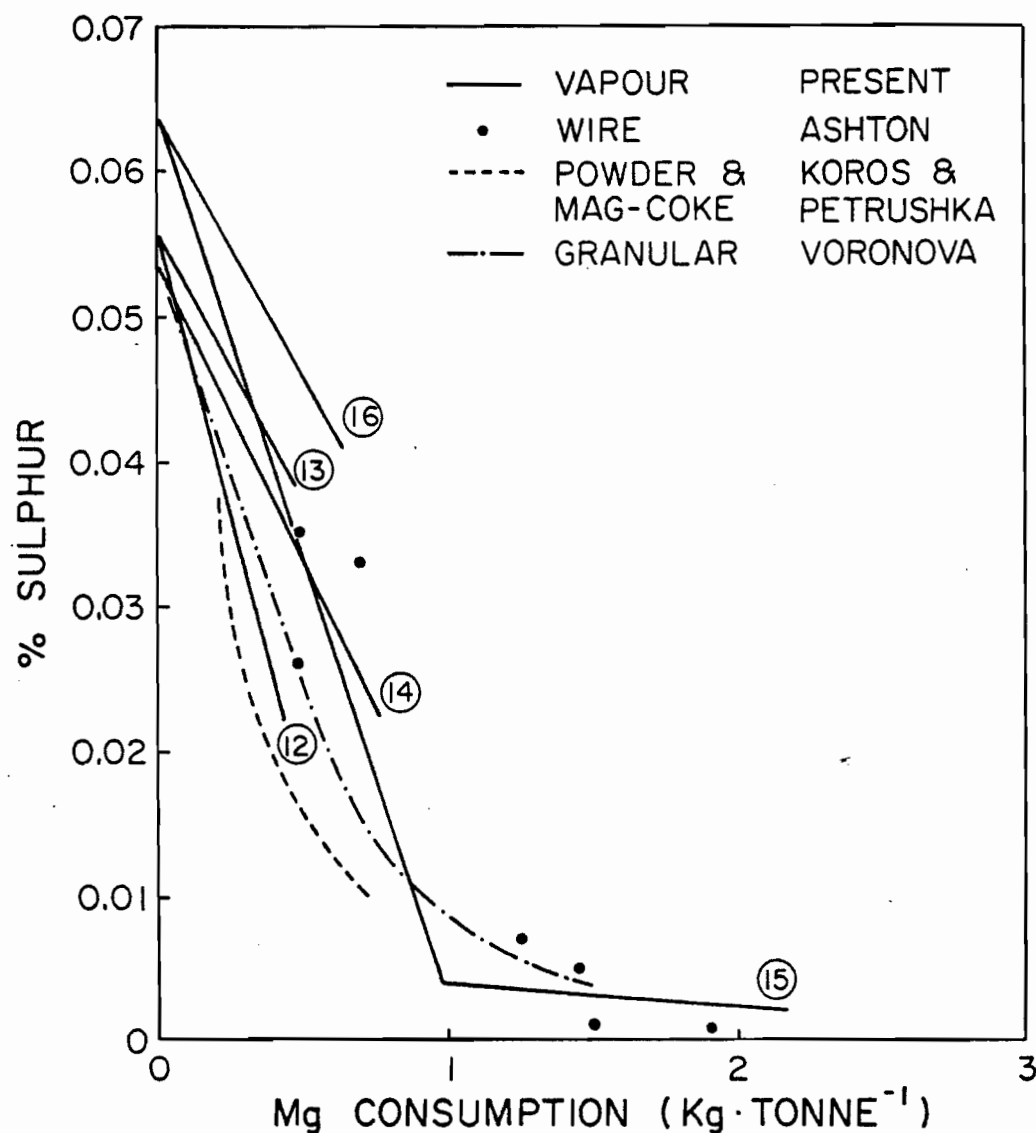


FIGURE 14. The amount of magnesium which must be added to the iron to achieve various sulphur levels, starting with 0.05 to 0.06% sulphur. The numbers indicate the run numbers from the present work. Representative data was taken from the other larger scale studies, References 45, 60 and 61, respectively.

CONCLUSIONS

From these experiments in which magnesium vapour was injected into iron-carbon melts, it has been found that the results of the sulphur and magnesium analyses of the bath were essentially the dissolved values. Very little of the magnesium or sulphur was present as MgS. The magnesium bubbles were quite large (at least 2.5 cm equivalent diameter and therefore spherical cap bubbles), and were found to dissolve with a liquid-phase mass transfer coefficient of $4.6 \pm 3.4 \times 10^{-3} \text{ cm s}^{-1}$. This value is much lower than expected for bubbles with mobile interfaces and only slightly lower than that for immobile ones. The exact cause, for example a surface-active agent, could not be positively identified. Theoretically, the effect of gas phase control should have been small. However, the rather large experimental error limits obscured any such effect which may have been present. The desulphurization reaction appeared to occur in the liquid by a second-order reaction:

$$\frac{d\% S}{dt} = k \left[(\% \text{ Mg}) \cdot (\% \text{ S}) - K_3 \right] \quad (85)$$

where k is $2.95 \pm 1.2 (\% \text{ Mg min})^{-1}$ and $\log K_3$ is -5.10 ± 0.45 . The latter value is in reasonable agreement with the equilibrium constant between dissolved magnesium and sulphur. A two step mechanism for desulphurization is proposed, whereby MgS embryos are formed by random collision in the melt. These subsequently diffuse to nucleation sites which are quickly eliminated from the melt. A constant supply of these sites is postulated to arise from the small amount of MgS which is formed

at the magnesium bubble interface. Analysis of available industrial data indicates circumstantial agreement with the present mechanism, although the industrial second-order rate constant exceeds the present one by an order of magnitude.

LIST OF SYMBOLS

a	activity
A_E	equivalent area of bubble
A_F	final equivalent area of bubble
A_O	initial equivalent area of bubble
A''	total equivalent area of bubbles in bath
C	molar concentration
C_{EQ}	equilibrium concentration at inclusion interface
C_M	concentration in inclusion
C_O	initial concentration
D_E	equivalent diameter of bubble
D_G	gas phase diffusivity
D_L	liquid phase diffusivity
D_{ni}	inner diameter of nozzle
D_{no}	outer diameter of nozzle
DSE	desulphurization efficiency defined by Equation 45
e_j^i	thermodynamic interaction parameter $\frac{\partial \log f_j}{\partial \% i}$
E_A	activation energy
f	wt% activity coefficient
f_B	frequency of bubble formation
F	molecular partition function
g	gravitational acceleration
h	height
h	Planck's Constant
h_i	Henrian wt% activity of component i
I	rate of nuclei formation

k	second order rate constant
k_B	Boltzmann's constant
k_G	gas phase mass transfer coefficient
k_L	liquid phase mass transfer coefficient
K_1, K_2, K_3, K_{EQ}	equilibrium constants
K_H	Henry's constant defined by Equation 24
M	molecular weight
MR	magnesium recovery defined by Equation 46
n	number of inclusions or embryos per unit volume
N_c'	capacitance group defined by Equation 49
N_O	Avogadro's Number
$\dot{N}_{Mg}, \dot{N}_{MgS}, \dot{N}_T$	molar rates (i.e. mole s^{-1}) of transfer defined by Equations 50, 51 and 52, respectively
$\dot{N}''_{Mg}, \dot{N}''_{MgS}$	molar fluxes (i.e. mole $cm^{-2}s^{-1}$) with respect of equivalent spherical bubble area
P	pressure
P_B	probability
Q	volumetric flow rate
r_I	radius of inclusion or embryo
r_{IF}	final radius of inclusion at complete reaction
r_o	average diffusion radius defined by
R	ideal gas constant
R_c	crucible radius
Re	Reynolds Number defined as $\frac{D_E U}{\nu}$
Sc	Schmidt Number defined as $\frac{\mu}{\rho D_L}$ for a liquid
Sh	Sherwood Number defined as $\frac{k_L D_E}{D_L}$ for a bubble in a liquid
t	time
t_{Ex}	exposure time

t_R	rising time of bubble
T	temperature
U	velocity
V_B	volume of bubble
V_C	volume of freeboard in magnesium retort
V_T	volume of bath
W_{Fe}	weight of bath
X	mole fraction

GREEK SYMBOLS

α	molar flux ratio defined by Equation 82
β	molar ratio of dissolution to desulphurization defined by Equation 83
δ	atomic diameter
σ	interfacial tension or energy
θ	surface coverage
ν	molecular vibration frequency
μ	viscosity

OTHER SUBSCRIPTS

c	critical
E	equivalent
EQ	equilibrium
G	gas
IN	injected

L	liquid phase property or state
LF	liquid phase transfer over the front of the bubble
LR	liquid phase transfer over the rear of the bubble
LOV	overall transport with liquid standard state
S	supersaturation

OTHER SUPERSSCRIPTS

B	bulk
F	final
G	gas phase
L	liquid phase
S	solid phase
*	interfacial
†	activated state or embryo

REFERENCES

1. P.K. Trojan and R.A. Flinn: Trans. A.S.M., 1961, Vol. 54, pp.549-66.
2. V.E. Scheil and H.L. Lukas: Giesserei techn.-wiss. Beihefte, 1965, Vol. 17, No.2, pp.61-64.
3. R. Moser: Giessereiforschung in English, 1969, Vol. 21, No.3, pp.130-39.
4. M.C. Speer and N.A.D. Parlee: A.F.S. Cast Metals Research Journal, Sept. 1972, pp.122-28.
5. G.A. Irons: M.Sc. Thesis, McGill University, 1975.
6. O. Kubaschewski, E.L. Evans, and C.B. Alcock: Metallurgical Thermochemistry, Fourth Edition, Pergamon Press, Oxford, 1967, pp.303-447.
7. J.P. Morris and R.C. Buehl: Trans. A.I.M.E., 1950, Vol. 188, pp.317-22.
8. G.W. Castellan: Physical Chemistry, Addison-Wesley Publishing Co., Reading, Ma., 1964, pp.631-50.
9. R. Clift, J.R. Grace and M.E. Weber: Bubbles, Drops and Particles, in press, Academic Press, N.Y.
10. J.R. Grace: Trans. Instn. Chem. Engrs., 1973, Vol. 51, pp.116-20.
11. A.C. Lochiel and P.H. Calderbank: Chem. Eng. Sci., 1964, Vol. 19, pp.471-84.
12. M.H.I. Baird and J.F. Davidson: Chem. Eng. Sci., 1962, Vol. 17, pp.87-93.
13. J.H.C. Coppus: Thesis, Eindhoven University of Technology, the Netherlands, 1977.
14. M.E. Weber: Chem. Eng. Sci., 1975, Vol. 30, pp.1507-10.
15. R. Higbie: Trans. A.I.Ch.E., 1935, Vol. 31, pp.365-87.
16. A.I. Johnson, F. Besik and A.E. Hamielec: Can. J. Chem. Eng., 1969, Vol. 47, p.559.
17. R.I.L. Guthrie and A.V. Bradshaw: Chem. Eng. Sci., 1973, Vol. 28, pp.191-203.

18. W.G. Davenport, A.V. Bradshaw and F.D. Richardson: J.I.S.I., 1967, Vol. 205, p.1034.
19. R.I.L. Guthrie and A.V. Bradshaw: Trans. A.I.M.E., 1969, Vol. 245, pp.2285-92.
20. K. Mori, M. Sano and H. Hoshino: Tetsu-to-Hagane, 1975, Vol. 61, No. 2, pp.185-94.
21. G. Bernard and C.H.P. Lupis: Met. Trans., 1971, Vol. 2, pp.2991-98.
22. K. Mori and M. Sano: Kinetics of Metallurgical Processes in Steelmaking, ed. W. Dahl et al., Verlag Stahleisen M.B.H., Dusseldorf, 1975, pp.492-512.
23. E.S. Machlin: Trans. A.I.M.E., 1960, Vol. 218, pp.314-26.
24. G.A. Irons and R.I.L. Guthrie: Can. Met. Quart., 1976, Vol. 15, No. 4, pp.325-32.
25. G.A. Irons et al.: Met. Trans. B, 1978, Vol. 9B, pp.151-54.
26. T. Deb Roy, N.H. El-Kaddah and D.G.C. Robertson: Met. Trans. B, 1977, Vol. 8B, pp.271-77.
27. F.D. Richardson: Physical Chemistry of Melts in Metallurgy Vol.2, Academic Press, N.Y., 1974, p.474.
28. A.V. Bradshaw and F.D. Richardson: Chemical Engineering in the Iron and Steel Industry, Institution of Chemical Engineers, 1970, p.130.
29. P. Kozakevitch: Surface Phenomena of Metals, Society of the Chemical Industry Monograph No. 28, London, 1968, pp.223-45.
30. G.R. Belton: Met. Trans. B, 1976, Vol. 7B, pp.35-42.
31. A.W. Adamson: Physical Chemistry of Surfaces, 2nd Ed., Interscience Publishers, N.Y., 1967, pp.565-68.
32. Ibid, pp.375-87.
33. E.T. Turkdogan: J.I.S.I., 1966, Vol. 204, pp.914-19.
34. L. von Bogdandy, W. Meyer and I.N. Stranski: Arch. Eisenh., 1961, Vol. 32, pp.451-60.
35. L. von Bogdandy, W. Meyer and I.N. Stranski: Arch. Eisenh., 1963, Vol. 34, pp.235-41.

36. M.L. Turpin and J.F. Elliott: J.I.S.I., 1966, Vol. 204, pp.217-25.
37. M. Humenik and W.D. Kingery: J. Am. Cer. Soc., 1954, Vol. 37, pp.18-23.
38. F.A. Halden and W.D. Kingery: J. Phys. Chem., 1955, Vol. 59, pp.557-59.
39. G.K. Sigworth and J.F. Elliott: Met. Trans., 1973, Vol. 4, pp.105-13.
40. E.T. Turkdogan: Sulphide Inclusions in Steel, ed. J.J. deBarbadillo and E.N. Snape, A.S.M., Metals Park, Ohio, 1974, pp.1-22.
41. C. Wert and C. Zener: J. Appl. Phys., 1950, Vol. 21, pp.5-8.
42. J. Szekely and N.J. Themelis: Rate Phenomena in Process Metallurgy, Wiley-Interscience, N.Y., 1971, p.611.
43. E.T. Turkdogan: J.I.S.I., 1972, Vol. 210, pp.21-36.
44. G.A. Irons and R.I.L. Guthrie: Met. Trans. B, 1978, Vol. 9B, pp.101-110.
45. M.C. Ashton et al.: Ironmaking and Steelmaking, 1975, No. 2, pp.111-14.
46. J. Kawa: Japan Inst. Metals, 1956, Vol. 20, p.514.
47. R.E. Grace and G. Derge: Trans. A.I.M.E., 1958, Vol. 212, p.331.
48. R.G. Barton and J.K. Brimacombe: Met. Trans. B, 1977, Vol. 8B, pp.417-27.
49. E.T. Turkdogan, P. Grieveson and L.S. Darken: J. Phys. Chem., 1963, Vol. 67, p.1647.
50. T.K. Sherwood and R.L. Pigford: Absorption and Extraction, McGraw-Hill, N.Y., 1952, pp.332-37.
51. R.B. Bird, W.E. Stewart and E.N. Lightfoot: Transport Phenomena, John Wiley & Sons, N.Y., 1960, pp.599-601.
52. K.I. Washchenko and A.P. Rudoy: Trans. A.F.S., 1962, pp.855-64.
53. R.B. Bird et al.: op. cit., pp.508-12.
54. F.D. Richardson: op. cit., pp.368-69.
55. R.D. Richardson: op. cit., pp.483-87.

56. W.H. Duquette, N.R. Griffing and T.W. Miller: Proceedings of the 29th Annual Meeting, Cherry Hill, N.J., May 6-8, 1973, International Magnesium Association, Dayton, Ohio.
57. P.J. Koros, R.G. Petrushka and R.G. Kerlin: I. & S.M., 1977, Vol. 4, No.6, pp.34-40.
58. P.J. Koros: U.S. Patent No.3,998,625, (1976).
59. U. Lindborg and K. Torssell: Trans. A.I.M.E., 1968, Vol. 242, pp.94-102.
60. P.J. Koros and R.G. Petrushka: Proceedings of the Symposium on External Desulphurization of Hot Metal, ed. W.-K. Lu, McMaster University, Hamilton, Canada, May 22-23, 1975.
61. N.A. Voronova: Russ. Casting Prod., pp.45-47, trans. from Liteinoe Proizvodstvo, 1974, No.2, pp.5-7.

LIST OF FIGURES

- Figure 1 Thermodynamics of desulphurization with magnesium of carbon-saturated iron at 1523 K. Speer and Parlee's⁴ data is shown with the recalculated curve as described in the text. The present data was taken from Figure 11. The indirect calculation is described in the text. The error bars represent ± 1 standard error of estimate.
- Figure 2 Supersaturation necessary for homogeneous nucleation. Line 1 represents Equation (29) and Line 2 represents Equation (38) with $T = 1523$ K and $C_M = 0.04$ mole cm^{-3} . The surface energies for SiO_2 , ZrO_2 and Al_2O_3 come from References 36, 37 and 38, respectively, while the critical supersaturations were taken from References 39, 34 and 35, respectively.
- Figure 3 A comparison of the diffusion models of precipitation. The fractional precipitation is given by $\frac{C - C_{\text{EQ}}}{(C_M - C_{\text{EQ}})}$. For these particular curves C_M , C_0 and C_{EQ} are 0.05, 10^{-5} and 10^{-6} mole cm^{-3} , respectively. The number of inclusions was assumed to be 10^6 cm^{-3} , thus r_{IF} is calculated to be $3.5 \times 10^{-4} \text{ cm}$. These numbers are typical of the present experimental situation for precipitation of MgS on inclusions.
- Figure 4 Schematic cross-section of the magnesium vaporizer and induction furnace, to scale.
- Figure 5 Magnesium and sulphur contents as a function of time for Run 1. The curves represent the results of the computer model.
- Figure 6 Magnesium and sulphur contents as a function of time for Run 11. The curves represent the results of the computer model.
- Figure 7 Magnesium and sulphur contents as a function of time for Run 12. The curves represent the results of the computer model.
- Figure 8 Magnesium and sulphur contents as a function of time for Run 15. The curves represent the results of the computer model.

- Figure 9 The apparent fluxes of sulphur, \dot{N}_{MgS} and magnesium, \dot{N}_{Mg} to and from the bubble interfaces, respectively, as a function of the sulphur level in the bath. The sum of \dot{N}_{MgS} and \dot{N}_{Mg} is denoted as the total flux of magnesium which originates from the bubbles. The numbers beside each point are the run numbers. The dotted line represents the amount of sulphur which can diffuse to the bubbles during their rise, as deduced in the text.
- Figure 10 The apparent magnesium and sulphur mass transfer coefficients as a function of the sulphur level in the bath. The numbers beside each point are the run numbers. The error bars indicate the estimated error limits on the data. The curves merely show the trends in the data and have no theoretical significance.
- Figure 11 The rate of magnesium sulphide formation for the whole bath as a function of the product of the magnesium and sulphur contents in the bath. The numbers beside each point are the run numbers. The error bars indicate the estimated accuracy of the data. The dotted line represents the regression on the data (Equation (67)). The curved line represents Equation (79) fitted to the experimental data.
- Figure 12 The rate of magnesium sulphide formation for the whole bath as a function of the dissolved magnesium and sulphur levels. The numbers beside each point are the run numbers. The dotted line represents an attempt to find a first-order dependency of the rate on the concentration of the least abundant species. See the text for the significance of this behaviour.
- Figure 13 The progress of desulphurization plotted as a function of the magnesium content of the bath for each run. These are known as "reaction paths". The predictions based on the model are also shown with the corresponding run number. The "equilibrium reaction paths" are shown as well for two typical cases: one starting above the equilibrium line, and the other below the equilibrium.
- Figure 14 The amount of magnesium which must be added to the iron to achieve various sulphur levels, starting with 0.05 to 0.06% sulphur. The numbers indicate the run numbers from the present work. Representative data was taken from the other larger scale studies, References 45, 60 and 61, respectively.

LIST OF TABLES

Table I	Comparisons of Physical and Chemical Adsorption, after Adamson. ³¹
Table II	Experimental Conditions and Basic Results
Table III	Supplementary Chemical Analysis
Table IV	Comparison with Magnesium Desulphurization Practice

CONCLUSIONS TO THE THESIS

GENERAL CONCLUSIONSPART I

From the work on the frequency of formation of pure argon bubbles in iron-carbon alloys, and the X-ray cinematography results in indium-gallium alloys, it was possible to identify several important aspects influencing the formation of bubbles in liquid metals.

1. The bubbles tended to spread from the inner diameter of a nozzle, across the face of the nozzle with an angle close to the equilibrium contact angle.
2. At low flow rate, the bubbles released when the buoyancy forces overcame the surface tension forces holding them to the nozzle. For small nozzles, this occurred when the bubble was at the outer diameter of the nozzle. For large nozzles (i.e., greater than 2.5 cm) the bubble did not reach the outer diameter before releasing.
3. At moderate flow rates, a constant frequency of bubble formation was established. The bubbles would release from the outer diameter for nozzles smaller than 1.3 cm outer diameter.
4. Bubbles released from downward facing nozzles were considerably smaller than those leaving from upward-or side-ways-facing nozzles. In the former case, the bubbles released as soon as they reached the outer diameter of the nozzle.

5. Large bubbles forming on sideways-facing nozzles were moved around to the top of the nozzle by buoyancy forces, and at moderate flow rates travelled along the top of the nozzle.
6. Because of the compressibility of the gas, the volume of the gas chamber behind the nozzle had a marked effect on the size of the bubbles. This is known in the literature as a capacitance effect, but in the present work its effect persisted to higher chamber volumes than was generally anticipated. At such large chamber volumes (i.e., greater than 600 cm^3), bursts of gas or bubble "pairs" were observed.

PART II

From the experiments on magnesium desulphurization of iron-carbon alloys it was demonstrated that:

1. The chemical analyses for magnesium and sulphur were essentially the dissolved values. Very little was combined as MgS .
2. Magnesium dissolved in the iron regardless of the sulphur level in the bath (up to at least 0.2% S).
3. The rate of mass transfer from the bubbles was considerably lower than that to freely circulating bubbles which may have been caused by a surfactant. Magnesium was suggested as the most likely surfactant.

4. Approximately 90% of the desulphurization took place in the liquid phase, although not by homogeneous nucleation of magnesium sulphide.
5. The rate of desulphurization appeared to follow the Law of Mass Action, in that it was second order with respect to dissolved magnesium and sulphur contents.
6. The rate of desulphurization dropped drastically at levels consistent with an independent study on the equilibrium between dissolved magnesium and sulphur.
7. A two-step model was proposed whereby magnesium and sulphur reacted in the liquid to form MgS embryos which did not have enough supersaturation to precipitate. They diffused to other MgS inclusions in the melt sheared from the bubble surfaces. The inclusions were constantly eliminated by induction stirring.

CLAIM TO ORIGINALITY

Several aspects of this Thesis constitute, in the Author's opinion, new and distinct contributions to knowledge. The major contributions are:

1. While it has been appreciated previously that a bubble spreads to the outside diameter of a nozzle in a liquid metal, this work demonstrates and explains the reason for the upper limit to this behaviour.
2. This is the first time X-ray cinematography has been applied to the study of bubble formation in liquid metals. This provides the first direct evidence that the bubbles spread to the outer diameter, as well as other phenomenological observations.
3. A novel mechanism of bubble formation in liquid metals is proposed on the basis of the experimental results.
4. This is the first time that a metallic desulphurizer (or deoxidizer, for that matter) has been added in a continuous and controlled manner into an iron melt to study the kinetics of the reaction.
5. The measurement of the bubble volumes, enabled the first determination of a mass transfer coefficient for large (spherical cap) bubbles rising through a ferrous alloy.
6. It is shown that magnesium desulphurization of iron is a second order heterogeneous reaction, which is a result not anticipated from the previous work in

the literature. Analysis of industrial data suggests that the same mechanism occurs on the large scale.

There are also several other innovations which pertain to the present experiment, and are not as universal in application:

7. A novel experimental method to obtain the frequency of bubble formation was developed to operate in intense audio- and radio-frequency noise generated by an induction furnace.
8. In the bubble formation work, the number and range of variables studied was much wider than in any other investigation of liquid metals, to date.
9. For the desulphurization experiments, a novel magnesium vaporizer was designed so that either pure magnesium or magnesium diluted with an inert carrier gas could be injected into an iron-carbon melt.
10. Since the desulphurization experiments were novel, the data was analyzed in an original manner, however this was mainly through a synthesis of concepts adapted from physical chemistry and transport phenomena.

APPENDICES

APPENDIX A

MAGNESIUM DESULPHURIZATION PRACTICE

Industrially, magnesium is injected into melts not only to desulphurize, but in some instances to produce ductile iron.¹ The major problem is one of obtaining proper contact between the magnesium and the iron. This is because magnesium is lighter than iron and tends to float out. Additionally, the violence of the vaporization also causes excessive splashing, fuming and low recoveries. The methods by which commercial operators have chosen to obviate these problems can be divided into two broad categories: mechanical systems and the use of magnesium compounds.

One mechanical method² employed a hollow tube, widened at the bottom, through which a magnesium ingot was lowered. The tube was lowered into the iron, and compressed air or inert gas was introduced at the top of the tube. The gas prevented magnesium vapour from rising in the tube. The operating details are compared with the other systems in Table A1.

In Table A1 ranges of operating conditions and results are reported. The magnesium recovery is defined as:⁹

$$MR = \frac{\Delta\% \text{ Mg} - 0.76 \Delta\% \text{ S}}{\% \text{ Mg}_{\text{IN}}} \quad (\text{A1})$$

where $\% \text{ Mg}_{\text{IN}}$ is the weight of magnesium injected as a percentage of the weight of iron. The magnesium recovery takes into account dissolved magnesium, along with the decrease in sulphur level. The

TABLE A1

Method	Wt. of Pig Iron (Tonne)	Magnesium Consumption Kg/Tonne	Sulphur Content		Efficiencies		Residual Magnesium (%)	Reference
			Before (%)	After (%)	MR (%)	DSE (%)		
hollow tubes containing Mg ingots	73.	0.4 -1.1	0.07 - .1	<.005- .2	50-75	~70	-	Levin <u>et al.</u> ²
autoclave	7.0	2.8 -2.9	-	-	25-65	-	0.03 -0.19	Vashchenko <u>et al.</u> ³
BOF-shaped reactor	1.-4.	1.2 -3.5	.1	0.005	40-70	~60	.021-2.2	Alt <u>et al.</u> ⁴
Mg injection with compressed air	7.5-8.0	0.4 -2.8	0.01 - .09	.003-.06	25-70	30-60	0.01 - .06	Voronova <u>et al.</u> ⁵
Mg/Al injection with N ₂	200	.25- .60	.015-.045	~0.01	-	10-50	-	Wood <u>et al.</u> ⁶
Mg/Ca ₂ injection with N ₂	200	.25- .60	.015-.045	~0.01	-	8-45	-	
Mg/Al injection with air	130-200	.15-0.7	.016-.108	.013-.067	-	8-15	-	Koros and Petrushka ⁷
'lime-mag' injection with N ₂	140-200	0.1 - .6	.02 - .05	.004-.038	-	60-90	-	Koros <u>et al.</u> ⁸
Mg wire with N ₂	.25	.6 -3.7	.035-.11	.005-.09	20-70	5-60	.002- .14	Ashton <u>et al.</u> ⁹
Mg coated with MgO	50-60	.37-1.1	.022-.125	.008-.013	-	20-80	-	Shestopalov <u>et al.</u> ¹¹
'MAG-COKE'	90	0.54-1.2	.016-.052	.002-.013	~73	~25	.002- .06	Duquette <u>et al.</u> ¹³

desulphurization efficiency, on the other hand, only gives credit for desulphurization:

$$\text{DSE} = \frac{-0.76 \Delta\% \text{ S}}{\% \text{ Mg}_{\text{IN}}} \quad (\text{A2})$$

Vashchenko et al.³ used an autoclave to increase the pressure above the bath to the point that no boiling occurred. They found this treatment effectively degassed the steel, but they did not study desulphurization.

Another mechanical method⁴ involved the use of a reactor shaped like a basic oxygen furnace. In one corner there was a compartment for lumps of magnesium, which when rotated into the operating position, was at the bottom of the iron bath. The iron was allowed to communicate with the magnesium through holes in the compartment walls.

The injection of magnesium powder with a carrier gas has been investigated by Voronova et al.⁵ The lance was made of steel, and air was injected through it at 2.5 atmospheres at rates between 0.9 and 2.5 kg tonne⁻¹ of hot metal.

Wood et al.⁶ injected magnesium/aluminum and magnesium/calcium powders into iron baths. Few experimental details were reported.

Koros and Petrushka⁷ also investigated magnesium/aluminum powder injection using argon as a carrier gas. More recently, they⁸ have developed the 'LIME-MAG' process in which lime and magnesium powder are injected.

Ashton et al.⁹ carried out pilot-scale work on magnesium wire injection with nitrogen carrier gas. Their results compared favorably with 'MAG-COKE'.

The Pont-A-Mousson process¹⁰ used refractory coatings to moderate the vaporization. Lumps of coated magnesium ingots, under a graphite bell, were submerged into the melt. Shestopalov et al.¹¹ also reported the use of a magnesia wash coating for magnesium ingots.

Millis et al.¹² were the first to produce ductile iron, which they accomplished with nickel/magnesium alloys. The alloys were designed to be denser than the iron so they would sink.

'MAG-COKE', a proprietary compound of coke impregnated with 43% magnesium has been widely used to desulphurize hot metal from the blast furnace. Duquette et al.¹³ provided data which were representative of the method. A graphite bell was fastened over a can of 'MAG-COKE', and the assembly was lowered into a Treadwell car. Twelve holes in the bell allowed the magnesium to escape into the bath. More recently, the price of this product has increased to the point that other methods such as pneumatic injection mentioned above are becoming more widespread. Calcium carbide is also replacing 'MAG-COKE' in some instances.⁸

As can be seen in Table A1, there is a great deal of variation with each process, and even more among them. Generally, the efficiencies were low when the initial or final sulphur was below 0.01% S or a large amount of magnesium was added. This was not unexpected, but it should be realized that a large part of this was due to the increased magnesium dissolution. For example, to desulphurize 90 Tonnes of hot metal containing 0.025% S with 'MAG-COKE' to 0.006% S requires 1 114 Kg can

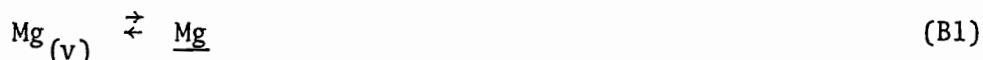
(0.55 Kg Mg/Tonne).¹³ The residual magnesium is 0.02% Mg, thus 1.4 times as much magnesium dissolved as was used in desulphurization.

REFERENCES

1. Cole, G.S.: A.F.S. Trans., Vol. 80, (1972), pp.335-48.
2. Levin, M.Z. et al.: Metallurgist U.S.S.R., pp.94-96, trans. from Metallurg., (1973), No.2, pp.10-12.
3. Vashchenko, K.I., Chernega, D.F. and Yarmolenko, V.K.: Russ. Casting Prod., July 1969, (7), pp.334-35.
4. Alt, A. et al.: A.F.S. Trans., Vol. 80, (1972), pp.167-72.
5. Voronova, N.A.: Russ. Casting Prod., pp.45-47, trans. from Liteinoe Proizvodstvo, (1974), No.2, pp.5-7.
6. Wood, J.K., Schoeberle, G.E. and Pugh, R.W.: "The External Desulphurization of Hot Metal - A Pneumatic Injection Technique", Proceedings of the Symposium on External Desulphurization of Hot Metal, McMaster University, Hamilton, Canada, May 22-23, 1975, ed. W.K. Lu.
7. Koros, P.J. and Petrushka, R.G.: "Materials for Hot Metal Injection", Proceedings of the Symposium on External Desulphurization of Hot Metal, McMaster University, Hamilton, Canada, May 22-23, 1975, ed. W.K. Lu.
8. Koros, P.J., Petrushka, R.G. and Kerlin, R.G.: I & SM, Vol. 4, No.6, (1977), pp.34-40.
9. Ashton, M.C. et al.: Ironmaking and Steelmaking, (1975), No.2, pp.111-14.
10. Masse, D. and Heine, H.J.: Foundry Management and Technology, Sept. 1974, pp.86,88,91.
11. Shestopalov, I.I., Glovatskii, A.B. and Krasavtsev, I.N.: Metallurgich i Gornorudnaya Promyshlennost, Vol. 10, No.1, (1969), pp.1-3.
12. Millis, K.D., Gagnebin, A.P. and Pilling, N.B.: U.S. Patent 2,485,760, Oct. 25, 1949.
13. Duquette, W.H., Griffing, N.R. and Miller, T.W.: 'Low Sulphur Steel from Mag-Coke Desulphurized Hot Metal', presented at the 29th Annual Meeting of the International Magnesium Association, Cherry Hill, N.J., May 6-8, 1973.

APPENDIX B
MAGNESIUM SOLUBILITY

The dissolution of magnesium vapour into a liquid iron matrix may be written as:



It has been confirmed¹⁻⁴ that magnesium obeys Henry's Law in cast irons, which means that

$$a_{\text{Mg}} = H \cdot X_{\text{Mg}} \quad (\text{B2})$$

where H is Henry's Constant.⁵ This law has been verified for a large number of dilute solutions⁶ and is the basis for Henrian activities.

The value of Henry's Constant for magnesium in cast iron must be determined experimentally and this was done by four investigators.¹⁻⁴ There were basically two experimental methods employed. The apparatus used by Trojan and Flinn² consisted of a sealed reaction chamber containing the cast iron melt covered with liquid magnesium. Inert gas pressure over the magnesium melt in excess of the magnesium vapour pressure at that temperature prevented boiling of magnesium. This method was only amenable to work at high magnesium pressures, because the temperature must be above the melting point of the ferrous phase.

The other method^{1,3,4} essentially involved a two-zone furnace; the hotter zone contained the cast iron and the cooler zone the magnesium

melt. These furnace designs then permitted independent variation of magnesium vapour pressure and cast iron temperature.

The results obtained are compared in Figure B1 for conditions closest in composition and temperature to the present work. Linear least squares regressions were employed when there were more than two points available at a particular carbon content from each investigator; otherwise lines were drawn through the origin. From examination of the curves one may see that Henry's Law is obeyed and that carbon enhances the solubility of magnesium. The results of Moser³ and Speer and Parlee¹ are in substantial agreement, whereas those of Scheil and Lucas⁴ and Trojan and Flinn² are somewhat lower. It was suggested by Moser³ that some proportion of the magnesium in the cast iron samples of Scheil and Lucas⁴ could have been lost by inadequate quenching. The sampling techniques of Trojan and Flinn², whereby the crucible was removed from the heating source before samples were aspirated, could also have induced error. For these reasons, and the fact that Moser³ and Speer and Parlee¹ had many more experimental points, their data will be used.

To discuss the solubility it is convenient to use Henry's Constant on the weight per cent scale, H' , which is the ordinate in Figure B1 at one atmosphere of magnesium pressure. (It is also the equilibrium constant for Equation (B1) in weight per cent.)

Speer and Parlee¹ performed their experiments at other temperatures and were able to develop temperature-dependent equations for H' and the effect of carbon on H' . Their equations for H' at 4.7 and 4.0% C, respectively, are

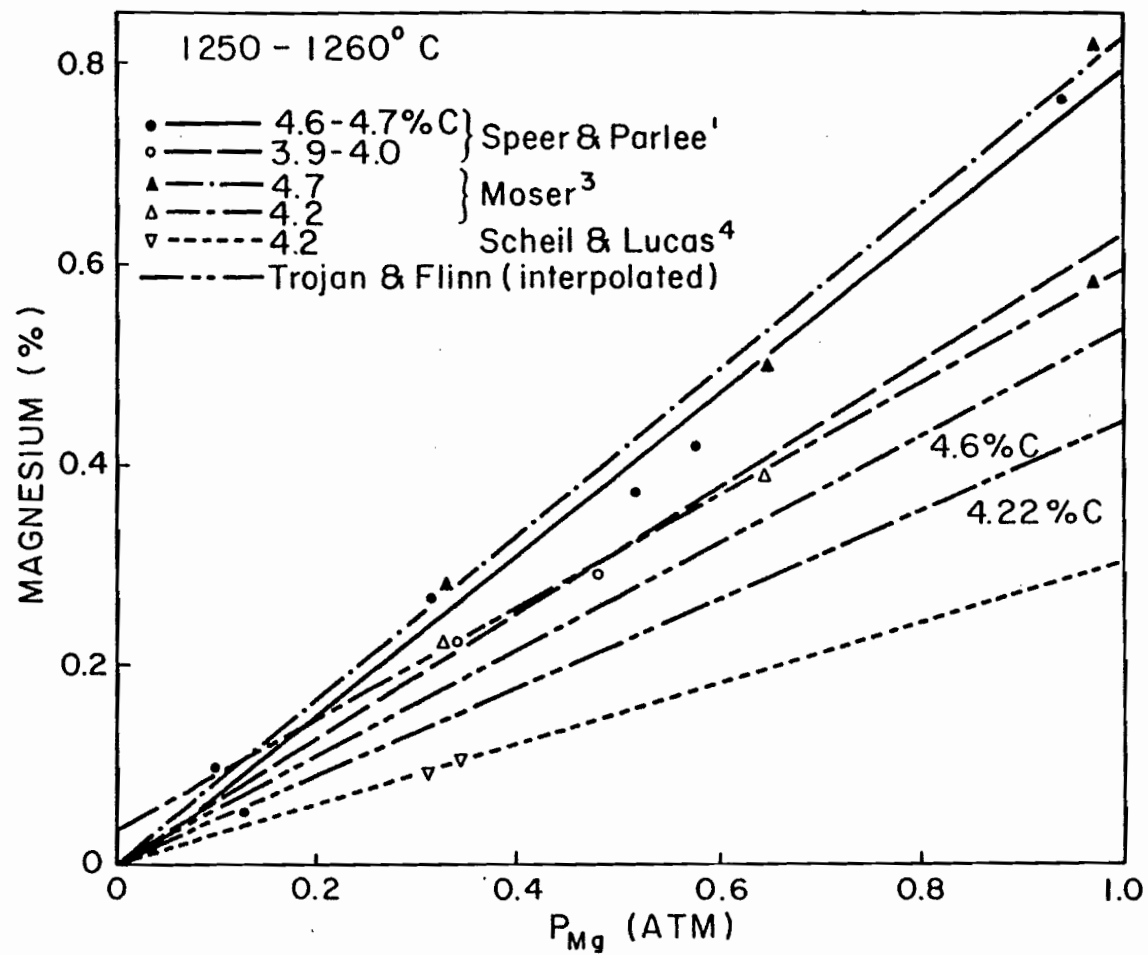


FIGURE B1. Magnesium solubility in cast irons.

$$\log H'_{4.7\%C} = -7.82 + \frac{11839 \pm 800}{T} \quad (B3)$$

and

$$\log H'_{4.0\%C} = -5.68 + \frac{8461 \pm 922}{T} \quad (B4)$$

Accordingly, at 1250°C, the values of H' are $0.90 - 0.63$ and $0.75 - 0.56$ at 4.7 and 4.0%C, respectively.

They accounted for the effect of carbon with an activity coefficient in the following manner:

$$\log H' = \log \frac{h_{Mg}}{p_{Mg}} - \log f_{Mg} \quad (B5)$$

where

$$\log f_{Mg} = \log f_{Mg}^0 + e_{Mg}^C(\%C) + e_{Mg}^{Mg}(\%Mg) \quad (B6)$$

using first order interaction parameters defined by:⁷

$$e_j^i = \frac{\partial \log h_j}{\partial \%i} \quad (B7)$$

Because magnesium in cast iron obeys Henry's Law, $f_{Mg}^0 = 1$ and $e_{Mg}^{Mg} = 0$, therefore all deviations from Henry's Law are due to changes in carbon content.

To compare the amounts of magnesium dissolved in two cast irons of different carbon contents, X and Y %C at one atmosphere of magnesium, one combines Equations (B5) and (B6) to obtain

$$e_{Mg}^C(X) + \log(H'_X) = e_{Mg}^C(Y) + \log(H'_Y) \quad (B8)$$

TABLE B1
COMPARISON OF H' VALUES

Source	%C			
	4.0	4.2	4.4	4.7
Speer's ¹ data Figure B1 1523-1533 K	0.63	-	-	0.79
Moser's ³ data Figure B1 1523-1533 K	-	0.59	-	0.82
Speer's ¹ correlations 1523 K	+ 2.27 0.75 - 0.56	+ 2.27 0.81 - 0.56	+ 2.11 0.81 - 0.63	+ 2.11 0.90 - 0.63
1533 K	+ 2.07 0.69 - 0.52	+ 2.07 0.74 - 0.52	+ 1.86 0.73 - 0.56	+ 1.86 0.80 - 0.56
This author 1523-1533 K	-	0.67	0.72	-

They¹ determined

$$e_{Mg}^c = 2.78 - \frac{4472}{T} \quad (B9)$$

Equation (B8) was used to interpolate $H'_{4.2\%C}$ and $H'_{4.4\%C}$ from $H'_{4.0\%C}$ and $H'_{4.7\%C}$, respectively, which are reported in Table B1. These calculations were also performed at 1533 K. Equation (B8) was also used to find e_{Mg}^c directly from Speer and Parlee's¹ data at 4.0 and 4.7%C, which was - 0.14. This was then used to interpolate $H'_{4.2\%C}$ and $H'_{4.4\%C}$ in this author's calculations in Table B1.

REFERENCES

1. Speer, M.C. and Parlee, N.A.D.: A.F.S. Cast Metals Research Journal, Sept. 1972, pp.122-128.
2. Trojan, P.K. and Flinn, R.A.: Trans. A.S.M., Vol. 54, (1961), pp.549-66.
3. Moser, R.: Giessereiforschung in English, Vol. 21, No.3, (1969), pp.130-39.
4. Scheil, V.E. and Lukas, H.L.: Giesserei techn.-wiss. Beihefte, Vol. 17, No.2, (1965), pp.61-64.
5. Kubaschewski, O., Evans, E. Ll. and Alcock, C.B.: "Metallurgical Thermochemistry", Fourth Edition, Pergamon Press, Oxford, (1967).
6. Darken, L.S. and Gurry, R.W.: "Physical Chemistry of Metals", McGraw-Hill Book Company, Inc., New York, (1953).
7. Elliott, J.F., Gliesser, M. and Ramakrishnan, V.: "Thermochemistry for Steelmaking", II, Addison-Wesley Press, Reading, Mass., (1963).

APPENDIX C

MASS TRANSFER CORRELATIONS

The literature on mass transfer to bubbles is extensive and has recently been well-reviewed.¹ Summaries of the most common correlations to mobile and immobile bubbles are contained in Tables C1 and C2, respectively. They are by no means complete, but do cover the entire range of bubble shapes and sizes. For Reynolds numbers greater than 10, the mobile mass transfer coefficients are approximately 2 to 10 times greater than the corresponding immobile coefficient. The shapes and velocities of bubbles have been correlated by Grace.¹⁷ He showed that the Davies and Taylor¹⁸ expression for the rising velocities of spherical-cap bubbles

$$U = 1.02 \left(\frac{g}{2} D_E \right)^{1/2} \quad (C1)$$

is appropriate for water and liquid metals, thus it is used in the present work.

The physical properties necessary for the evaluation of transport correlations have been taken from the literature: the density of iron - 4.4% carbon at 1523 K is 7.0 g cm^{-3} ¹⁹ and the viscosity is 0.09 Poise.²⁰ The diffusivity was estimated to be $3 \times 10^{-5} \text{ cm}^2 \text{ s}^{-1}$ from the theories of self-diffusion in liquid metals, but could be in error by a factor of 3.²¹ The diffusivity of sulphur in carbon-saturated irons has been measured, and at 1523 K it is $1.5 \times 10^{-5} \text{ cm}^2 \text{ s}^{-1}$,^{22,23} within a factor of 2.

TABLE C1

MASS TRANSFER CORRELATIONS FOR SINGLE BUBBLES WITH MOBILE INTERFACES

Sherwood Number Sh	Derivation	Range of Applicability	Experimental Confirmation	Source
$0.65 \text{ Pe}^{0.5}$	creeping flow, boundary layer theory	spheres, $\text{Re} < 1$, $\text{Pe} \geq 1$	none	Levich ²
$1.13 \text{ Pe}^{0.5}$	potential flow, boundary layer theory	spheres, $\text{Re} \geq 1$, $\text{Pe} \geq 1$	yes, Hammerton and Garner ³	Boussinesq ¹⁴
$1.13 \text{ Pe}^{0.5}$	potential flow, penetration theory	spheres, $\text{Re} \geq 1$	yes, Hammerton and Garner ³	Higbie ⁵
$1.13(1 - \frac{2.96}{\text{Re}^{1/2}})^{1/2} \text{ Pe}^{1/2}$	potential flow, penetration	spheres, $\text{Re} > 1$, $\text{Pe} \geq 1$	none	Lochiel and Calderbank ⁶
$\frac{2}{3}(1+j)^{1/2} \left[\frac{2.26\text{E}^{1/3}(\text{E}^2-1)^{1/2}\text{Pe}^{1/2}}{\text{E}(\text{E}^2-1)^{1/2} + \ln(\text{E} + (\text{E}^2-1)^{1/2})} \right]$	Zahm's ⁷ stream- function, boundary layer theory	oblate spheroids, $\text{Re} > 1$, $\text{Pe} > 1$	none	Lochiel and Calderbank ⁶
$1.15 \text{ Pe}^{1/2}$	potential flow, boundary layer theory	front of spherical cap bubbles, equivalent areas	yes	Baird and Davidson ⁸ , Weber ⁹
$1.21 \text{ Pe}^{1/2}$	potential flow, boundary layer theory	spherical cap bubbles over frontal area	yes	Lochiel and Calderbank ⁶ , Coppus ¹⁰
$1.32 \text{ Pe}^{1/2}$	potential flow, boundary layer theory	spherical cap bubbles over frontal area	yes	Johnson, Besik and Hamielec ¹¹
$1.12 \text{ Pe}^{1/2} \left(\frac{\text{D}_E}{0.5+0.2 \text{ D}_E} \right)^{1/2}$	potential flow, penetration theory	spherical cap bubbles over frontal area	yes, Coppus ¹⁰	Johnson, Besik and Hamielec ¹¹
$0.886 \text{ Pe}^{1/2}$	potential flow, penetration theory	spherical cap bubbles over frontal area	no	Coppus ¹⁰
$0.341 \text{ Pe}^{1/2}$	wake shedding, penetration theory	rear of spherical cap bubbles, equivalent areas	yes	Weber ⁹

TABLE C2
MASS TRANSFER CORRELATIONS FOR SINGLE BUBBLES WITH IMMOBILE INTERFACES

Sherwood Number	Derivation	Range of Applicability	Experimental Confirmation	Source
$1.01 Pe^{1/3}$	creeping flow	spheres, $Re < 1$, $Pe \geq 1$	none	Levich ²
$0.99 Pe^{1/3}$	laminar flow, boundary layer theory	spheres, $Re < 1$, $Pe \geq 10^3$	none	Friedlander ¹²
$0.99 Pe^{1/3}$	potential flow, boundary layer theory	spheres, $Re < 1$, $Pe > 100$	none	Lochiel and Calderbank ⁶
$.84 Re^{1/2} Sc^{1/3}$	separation at 108° , boundary layer theory, rear 20% of front	spheres, $Re > 1$	yes, Garner and Suckling ¹⁸	Lochiel and Calderbank ⁶
$2 + 0.552 Re^{1/2} Sc^{1/3}$	boundary layer theory	spheres, $Sc \leq 2.4$ $10 < Re < 10^3$	yes	Frossling ¹⁴
$2 + 0.6 Re^{1/2} Sc^{1/3}$	boundary layer theory	spheres, $Sc \geq 1$, $2 \leq Re \leq 200$	yes	Ranz & Marshall ¹⁵
$.84 \left(\frac{A_{\text{sphere}}}{A_{\text{oblate}}} \right)^{1/2} E^{1/6} Re^{1/2} Sc^{1/3}$	empirical	oblate spheroids	yes, Skolland and Cornish ¹⁶	Lochiel and Calderbank ⁶
$0.824 Sc^{-1/6} Pe^{1/2}$	boundary layer theory	front of spherical cap bubbles, equivalent area	yes	Weber ⁹

REFERENCES

1. Clift, R., Grace, J.R. and Weber, M.E.: Bubbles, Drops and Particles, Academic Press, N.Y., in press.
2. Levich, V.G.: Physiochemical Hydrodynamics, Prentice Hall, New York, (1962).
3. Hammerton, D. and Garner, F.H.: Trans. Instn. Chem. Engrs., Vol. 32, (1954), Supplement, pp.S18-S24.
4. Boussinesq, M.: Ann. Chim. et Phys. (Paris), Vol. 29, (1913), p.364.
5. Higbie, R.: Trans. A.I.Ch.E., Vol. 31, (1935), pp.365-87.
6. Lochiel, A.C. and Calderbank, P.H.: Chem. Eng. Sci., Vol. 19, (1964), pp.471-84.
7. Zahm, A.F.: Nat. Advis. Comm. Aeronaut., Rep. 253 1926 517, Washington.
8. Baird, M.H.I. and Davidson, J.F.: Chem. Eng. Sci., Vol. 17, (1962), pp.87-93.
9. Weber, M.E.: Chem. Eng. Sci.: Vol. 30, (1975), pp.1507-10.
10. Coppus, J.H.C.: Thesis, Eindhoven University of Technology, the Netherlands, 1977.
11. Johnson, A.I., Besik, F. and Hamielec, A.E.: Can. J. Chem. Eng., Vol. 47, (1969), p.559.
12. Friedlander, S.K.: A.I.Ch.E.J., Vol. 3, (1957), p.43.
13. Garner, F.H. and Suckling, R.D.: A.I.Ch.E.J., Vol. 4, (1958), pp.114-24.
14. Frossling, N.: Beitraege Zur Geophysik, Vol. 32, (1938), pp.170-216.
15. Ranz, W.E. and Marshall, W.R.: Chem. Eng. Prog., Vol. 48, (1952), pp.141-46, 173-80.
16. Skelland, A.H.P. and Cornish, A.R.H.: A.I.Ch.E.J., Vol. 9, (1963), pp.73-76.
17. Grace, J.R.: Trans. Instn. Chem. Engrs., Vol. 51, (1973), pp.116-20.

18. Davies, R.M. and Taylor, G.I.: Proc. Roy. Soc. (London), Vol. A 200, (1950), pp.375-87.
19. 'The Making, Shaping and Treating of Steel', ed. McGannon, H.E., United States Steel Corp., Pittsburgh, (1971).
20. Elliott, J.F., Gliesser, M. and Ramakrishnan, V.: "Thermochemistry for Steelmaking, II", Addison-Wesley Press, Reading, Mass., (1963).
21. Irons, G.A.: M.Sc. Thesis, McGill University, Montreal, 1975.
22. Kawa, J.: Japan Inst. Metals, Vol. 20, (1956), p.514.
23. Grace, R.E. and Derge, G.: Trans. Met. Soc. A.I.M.E., Vol. 212, (1958), p.331.

NOMENCLATURE

<u>Symbol</u>	<u>Significance</u>
A	bubble area
D_E	equivalent spherical bubble diameter
e	shape factor defined by $(1 - E^{-2})^{1/2}$
E	bubble eccentricity, width to height ratio
g	gravitational acceleration
j	shape factor defined by $\frac{E \sin^{-1} e - eE^2}{e - E \sin^{-1} e}$
k_L	liquid phase mass transfer coefficient
Pe	bubble Peclet Number, $\frac{D_E U}{D_L}$
Re	bubble Reynolds Number, $\frac{D_E U}{\nu}$
Sc	liquid phase Schmidt Number, $\frac{\nu}{D_L}$
Sh	dimensionless liquid phase mass transfer coefficient, $\frac{k_L D_E}{D_L}$
U	rising velocity of the bubble
μ	viscosity
ν	kinematic viscosity
ρ	density

APPENDIX D

EXTRA EXPERIMENTAL RESULTS AND CALCULATIONS

The results for two other runs at low sulphur, 2 and 7, are contained in Figures D1 and D2, where reasonable agreement between the model and the results was obtained. Three other runs, 13, 14 and 16, in the next three figures did not demonstrate as good agreement with the model. This was apparently because of leaks in the retort, as discussed in the text.

The detailed calculations of the transfer and reaction rates are also contained in this section. Simply stated, the rates were obtained from the slopes of the magnesium and sulphur against time curves, at various times through each run. The bubble areas were estimated, so that the specific reaction rates could be calculated. Several simplifying assumptions have been made in these calculations, however the accuracy of the data does not warrant more exact treatment.

The step-by-step calculations follow with the numerical values contained in Table D1. The bath weight, W_{Fe} , was the average weight calculated from the bath volume before and after bubbling (for a density of 7.0 g cm^{-3}). Similarly, h was the average metal depth over the nozzle. The average flow rate, Q , was that determined from the weight loss of the retort during the bubbling time, plus the argon carrier gas flow rate:

$$Q = \frac{\Delta W_{Mg}}{\Delta t} \frac{RT}{PM_{Mg}} + Q_{Ar} \quad (D1)$$

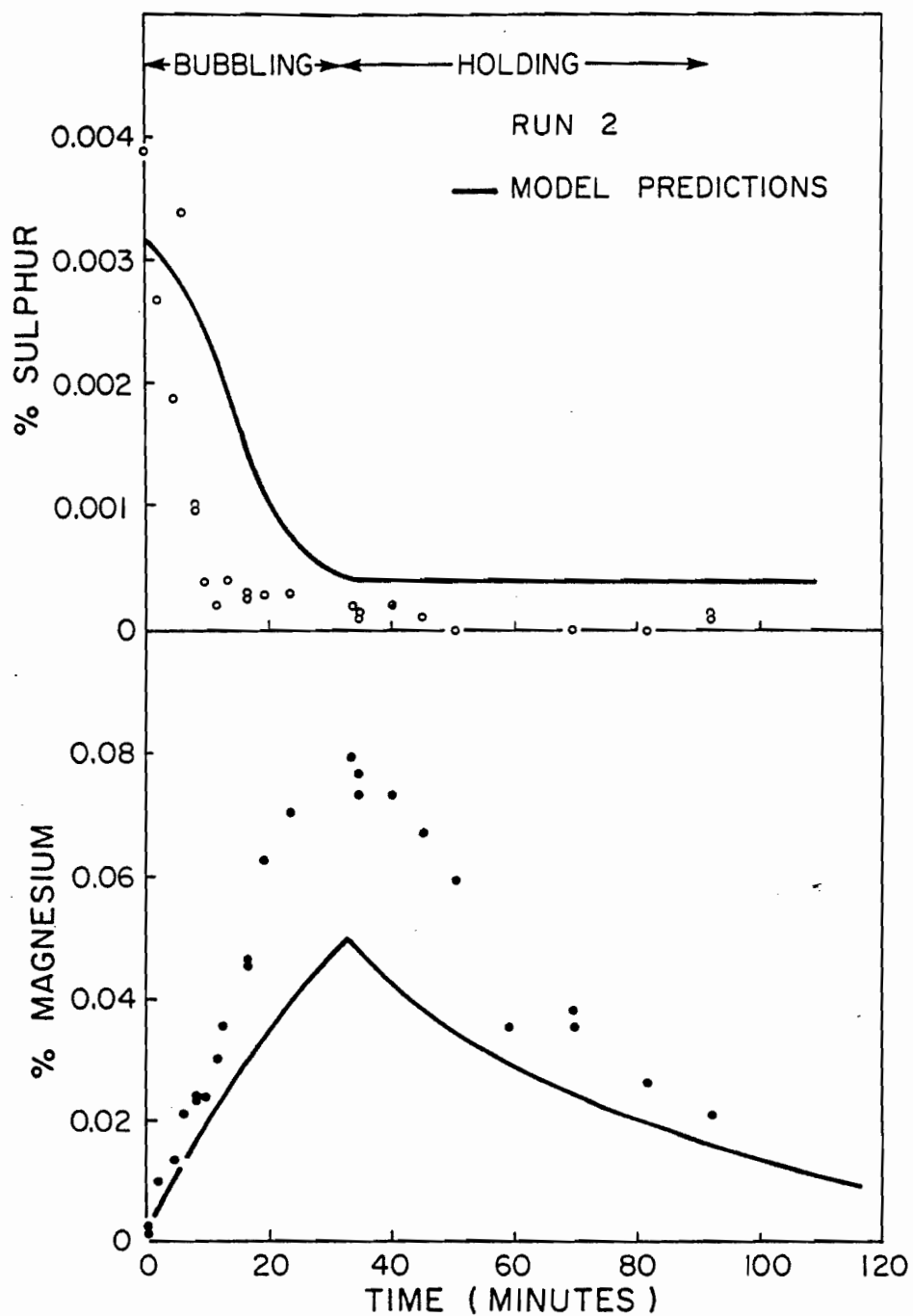


FIGURE D1. Magnesium and sulphur contents as a function of time for Run 2. The curves represent the results of the computer model.

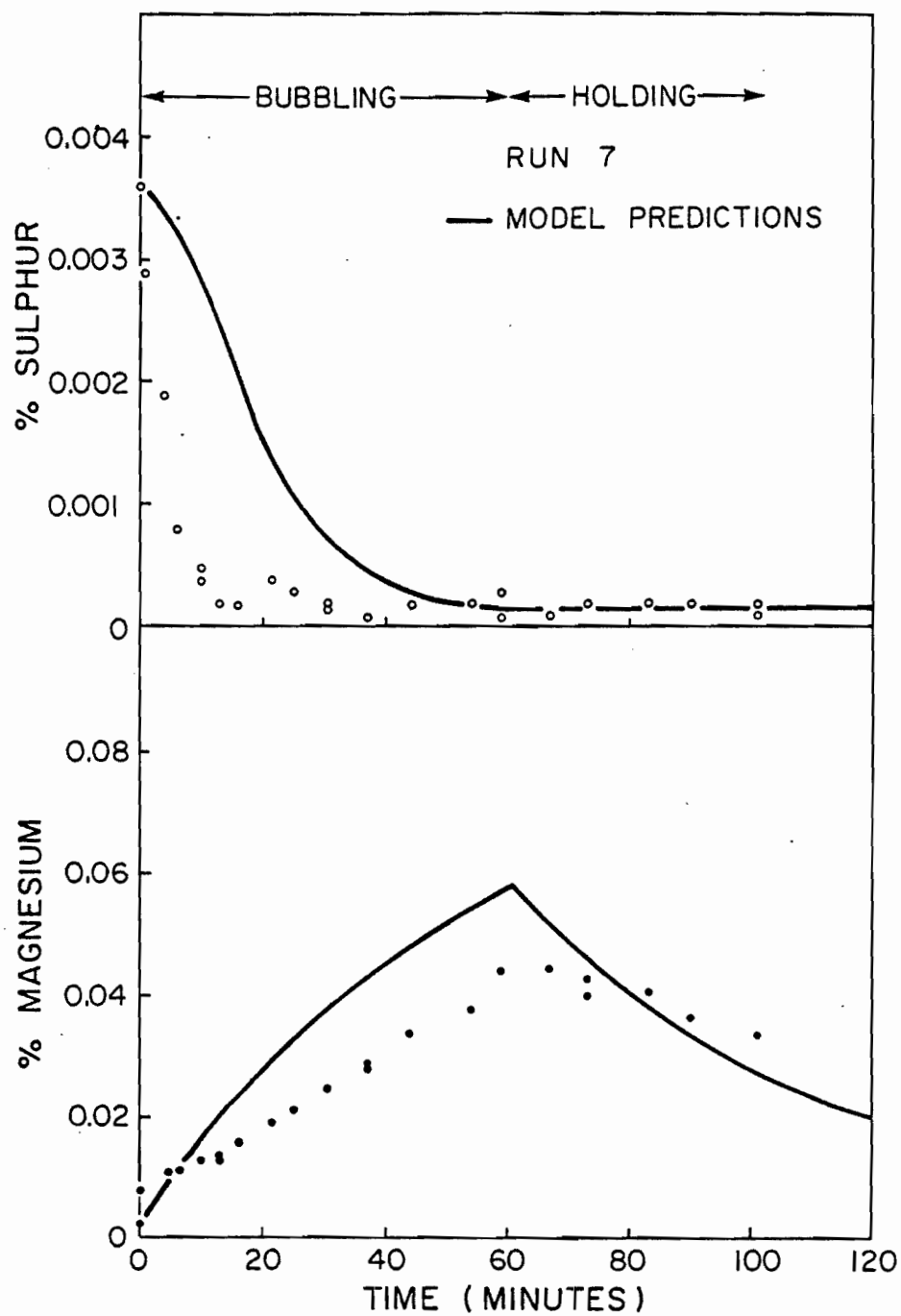


FIGURE D2. Magnesium and sulphur contents as a function of time for Run 7. The curves represent the results of the computer model.

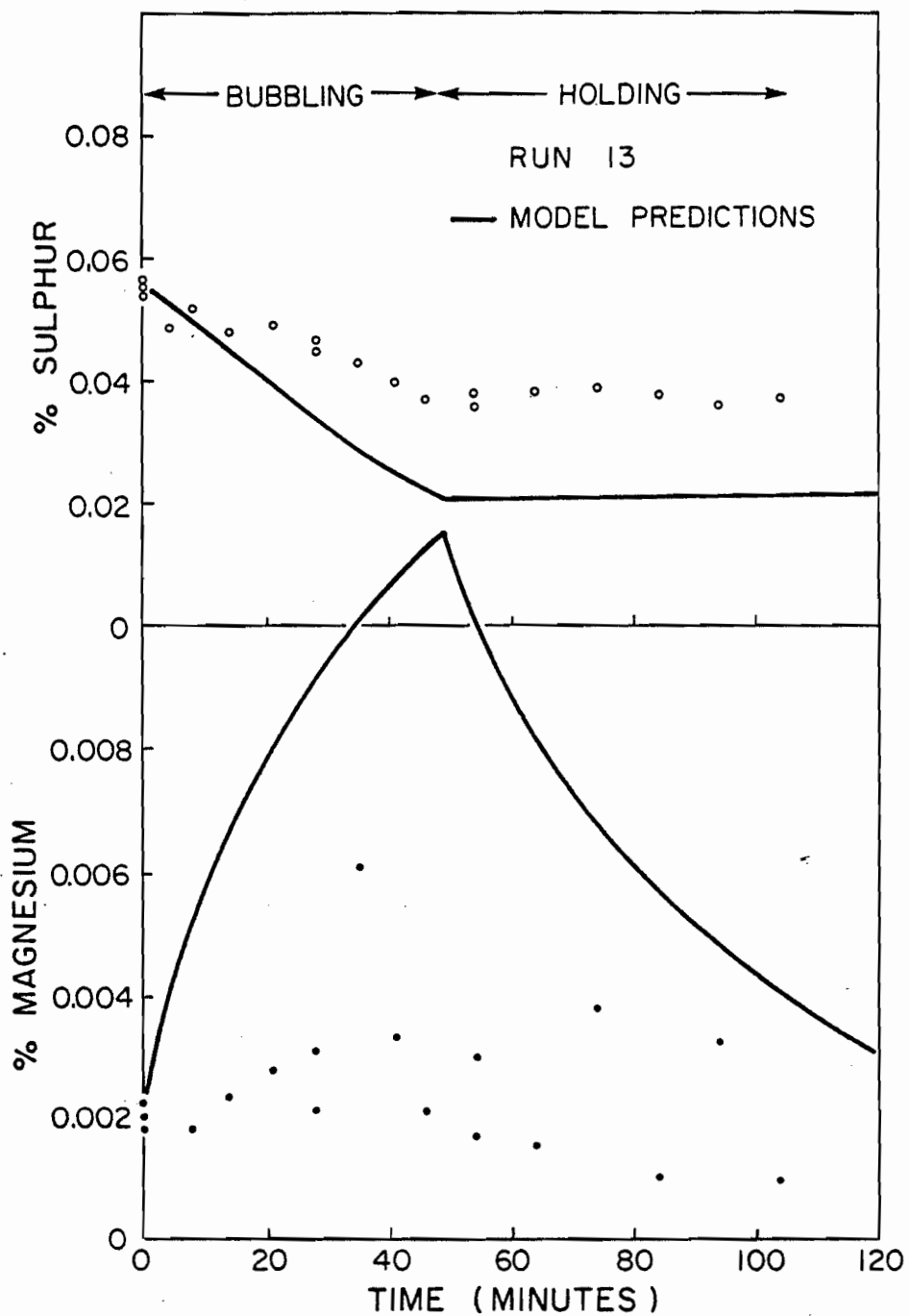


FIGURE D3. Magnesium and sulphur contents as a function of time for Run 13. The curves represent the results of the computer model.

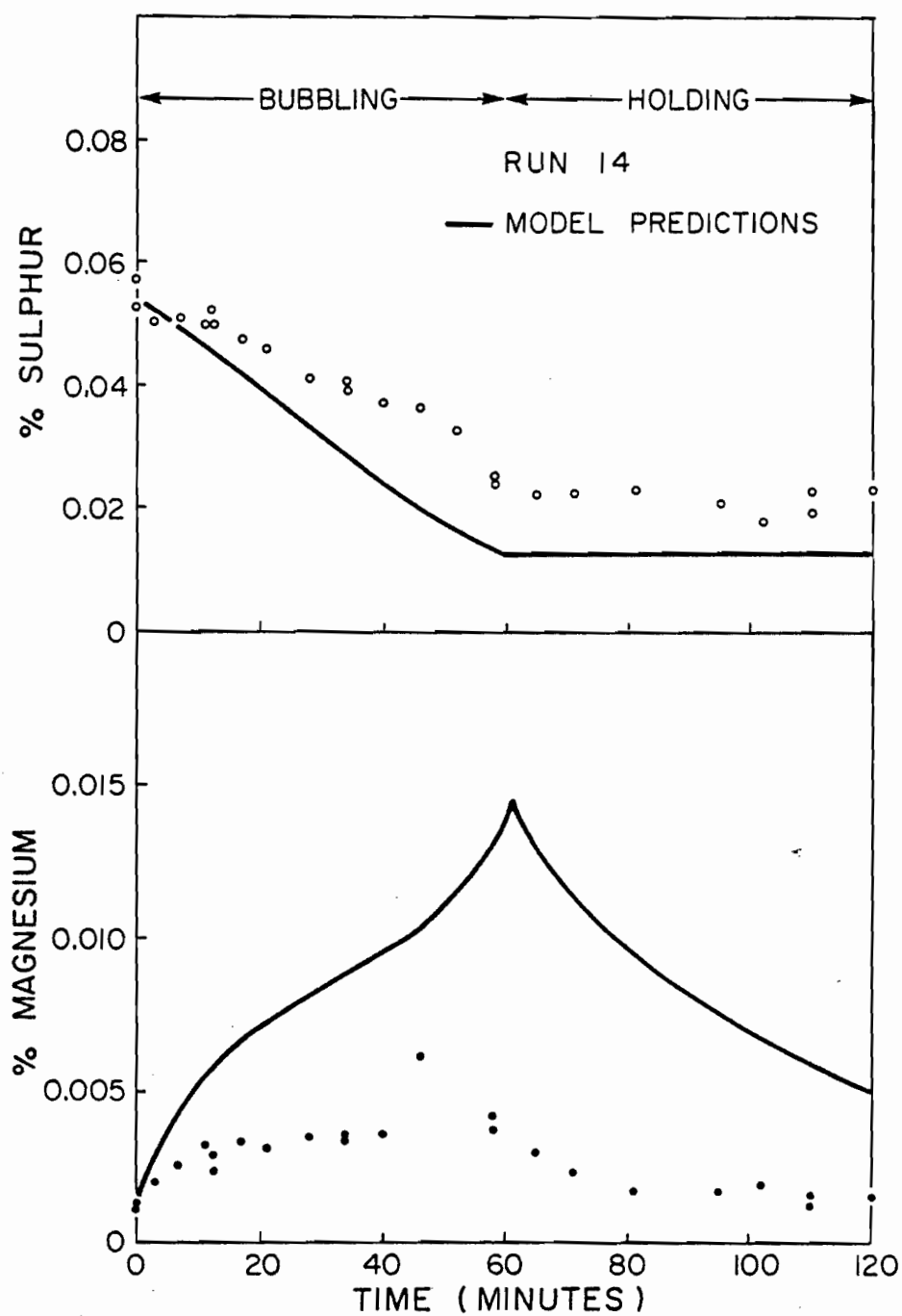


FIGURE D4. Magnesium and sulphur contents as a function of time for Run 14. The curves represent the results of the computer model.

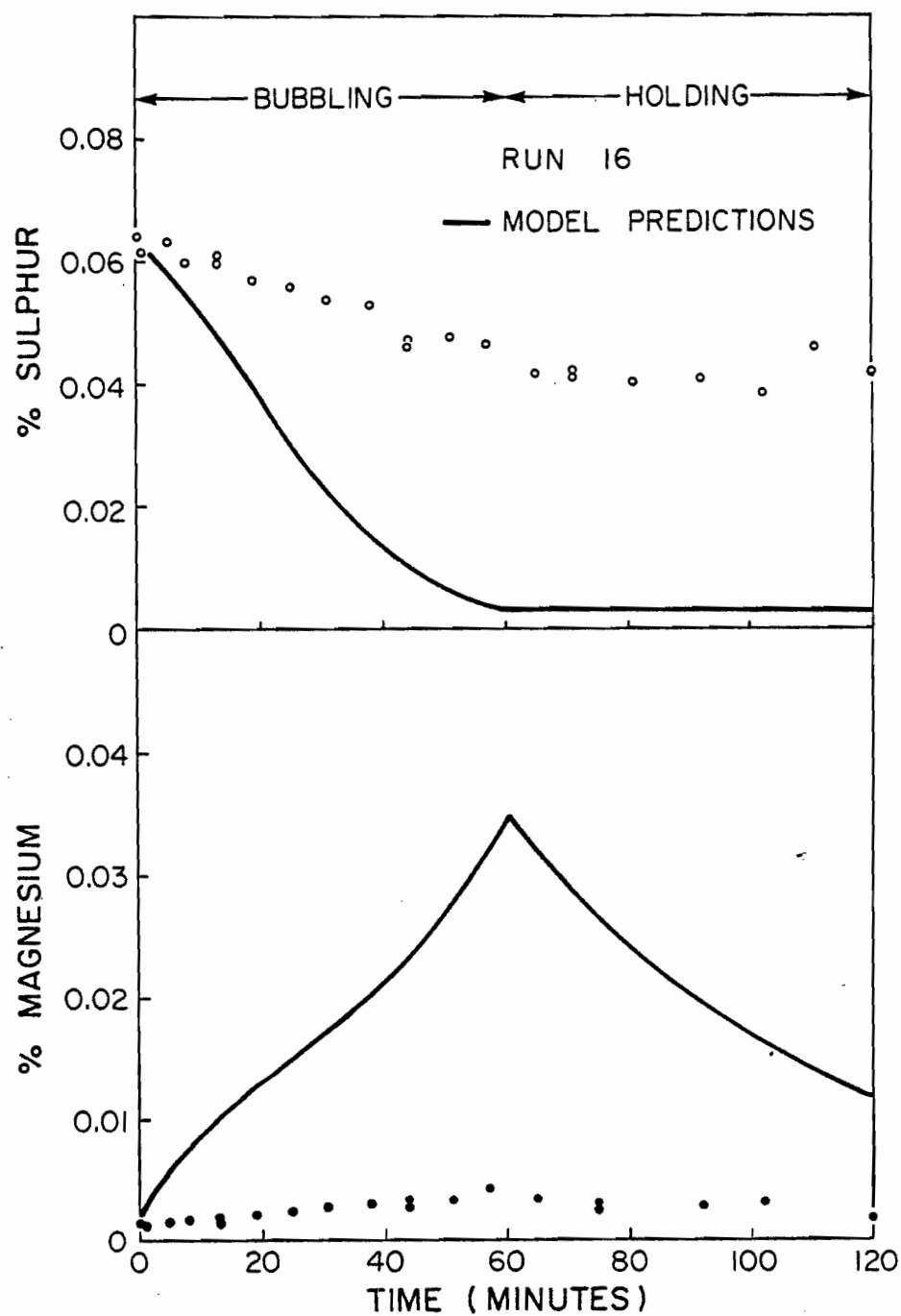


FIGURE D5. Magnesium and sulphur contents as a function of time for Run 16. The curves represent the results of the computer model.

TABLE D1
RATE CALCULATIONS

No.	Run	Time (min)	W_{Fe} ($g \times 10^{-4}$)	h (cm)	Q ($cm^3 \cdot s^{-1}$)	X_{Ar}	V_C (cm^3)	D_E^0 (cm)	V_B^0 (cm^3)	A_E^0 (cm^2)	f_B (s^{-1})	U ($cm \cdot s^{-1}$)	t_R (s)
1	1	3	5.816	12.1	381.	0.	581.	4.07	35.3	52.0	10.8	45.6	0.265
2		15											
3	2	5	5.816	12.1	219.	0.	481.	3.44	21.4	37.2	10.3	41.9	0.289
4		10											
5		20											
6	7	5	6.289	14.9	125.	0.155	560.	2.99	14.0	28.1	8.92	39.1	0.381
7		20											
8		50											
9	11	5	6.289	15.6	107.	0.181	716.	2.95	13.4	27.3	7.98	38.8	0.402
10		20											
11		45											
12	12	5	6.492	12.7	53.1	0.115	763.	2.66	9.87	22.3	5.37	36.9	0.344
13		20											
14		40											
15	13	16	6.492	11.4	76.8	0.253	727.	2.78	11.3	24.4	6.80	37.7	0.302
16		36											
17	14	5	6.492	10.2	80.0	0.243	767.	2.83	11.8	25.1	6.76	38.0	0.267
18		25											
19		45											
20	15	10	6.154	9.84	256.	0.280	774.	3.67	25.9	42.3	9.87	43.3	0.227
21		30											
22		50											
23	16	30	6.357	23.5	73.	0.266	755.	2.75	10.9	23.7	6.73	37.4	0.627
24		50											

TABLE D1 (cont'd.)

No.	% Mg	% S	$\Delta\% \text{ Mg}/\Delta t$ (%.s ⁻¹ x10 ⁷)	$-\Delta\% \text{ S}/\Delta t$ (%.s ⁻¹ x10 ⁷)	\dot{N}_{Mg}	\dot{N}_{MgS} (mole.s ⁻¹ x10 ⁵)	\dot{N}_{T}	X_{AR}^{F} (-)	$V_{\text{B}_3}^{\text{F}}$ (cm ³)	$\Lambda_{\text{E}}^{\text{F}}$ (cm ²)	Λ'' (cm ²)
1	0.0085	0.0006	310.	5.0	74.2	0.907	305.	0.	26.6	43.1	162.
2	0.043	0.0002	317.	< 0.5	75.9	0.0907	305.	0.	26.5	43.0	162.
3	0.016	0.0019	517.	50.	124.	9.07	175.	0.	5.12	14.4	95.4
4	0.028	0.0004	325.	50.	77.8	9.07	175.	0.	10.8	23.6	109.
5	0.060	0.0003	708.	0.71	169.	0.129	175.	0.	0.716	3.87	79.7
6	0.011	0.0016	83.3	66.6	21.6	13.1	100.	0.237	9.14	21.1	97.6
7	0.018	0.0003	100.	1.66	25.9	0.325	100.	0.210	10.3	22.9	86.6
8	0.0375	0.0002	121.	< 0.1	31.3	0.0196	100.	0.226	9.62	21.9	99.0
9	0.0027	0.178	25.	260.	6.47	51.0	85.6	0.551	4.40	21.3	91.6
10	0.0038	0.155	2.2	260.	0.569	51.0	85.6	0.455	5.33	14.8	81.1
11	0.0041	0.114	1.1	260.	0.284	51.0	85.6	0.451	5.37	14.8	81.1
12	0.0040	0.0528	86.7	117.	23.2	23.7	42.5	-	1.14	5.28	36.6
13	0.0065	0.0420	6.94	117.	1.85	23.7	42.5	0.288	3.94	12.1	42.9
14	0.0070	0.0280	6.94	117.	1.85	23.7	42.5	0.288	3.94	12.1	42.9
15	0.0023	0.050	12.5	60.6	3.34	12.3	61.4	0.339	8.42	20.0	57.8
16	0.0032	0.042	4.0	60.6	1.07	12.3	61.4	0.323	8.44	20.7	58.5
17	0.0025	0.0516	15.7	72.1	4.19	14.6	64.0	0.344	8.33	19.9	53.1
18	0.0033	0.0440	2.78	72.1	0.742	14.6	64.0	0.320	8.99	20.9	54.0
19	0.0040	0.0355	16.7	72.1	4.46	14.6	64.0	0.346	8.31	19.8	53.1
20	0.0055	0.0400	40.0	390.	10.1	74.9	205.	0.478	15.1	29.5	102.
21	0.0225	0.0030	200.	30.4	50.6	5.76	205.	0.386	18.8	34.2	107.
22	0.0365	0.0016	200.	5.33	50.6	1.02	205.	0.374	19.4	34.9	108.
23	0.0025	0.0545	3.33	55.5	0.871	11.0	58.4	0.334	8.65	20.3	105.
24	0.0033	0.0475	15.0	55.5	3.92	11.0	58.4	0.357	8.08	19.4	103.

TABLE D1 (cont'd.)

No.	N_{Mg}'' (mole.cm ⁻² .s ⁻¹ .10 ⁺⁷)	N_{MgS}''	k_{LMg} (cm.s ⁻¹ .10 ⁺⁴)	k_{LS}	N_{EV} (mole.s ⁻¹ .10 ⁺⁵)	k_L (cm.s ⁻¹ .10 ⁺⁴)
1	45.8	0.560	22.7	428.	6.56	23.3
2	46.9	0.056	23.2	128.	33.2	31.2
3	130.	9.51	64.5	2300.	12.4	75.6
4	71.4	8.32	35.4	9540.	21.6	46.1
5	212.	0.162	105.	247.	46.3	-
6	22.1	27.5	13.6	7890.	8.49	27.3
7	29.9	0.375	18.1	574.	13.9	28.1
8	31.6	0.0198	19.4	45.4	29.0	37.3
9	7.06	55.7	5.51	143.	2.08	50.8
10	0.701	62.9	0.508	186.	2.94	48.7
11	0.350	62.9	0.254	253.	3.17	48.7
12	63.4	64.8	71.1	563.	3.09	-
13	4.31	55.2	2.68	603.	5.02	44.3
14	4.31	55.2	2.68	905.	5.40	44.8
15	5.78	21.3	4.07	195.	1.77	21.2
16	1.83	21.0	1.27	230.	2.47	18.8
17	7.89	27.5	5.56	244.	1.93	27.5
18	1.37	27.0	0.945	282.	2.55	22.8
19	8.39	27.5	5.91	355.	3.09	29.4
20	9.90	73.4	7.92	842.	4.25	70.0
21	47.3	5.38	35.3	823.	17.4	51.4
22	46.9	0.944	34.5	271.	28.2	54.3
23	0.830	10.5	0.589	88.2	1.93	93.2
24	3.81	10.7	2.74	103.	2.55	12.2

x_{Ar}^0 was the fraction of argon in the gas flow at the nozzle, before any magnesium dissolved.

The bubble equivalent diameter was calculated from the correlation for pure argon:¹

$$D_E^0 = 1.444 N_c'^{0.816} + \left[(2.086 N_c'^{1.632} + 0.0259 Q^2)^{1/2} \right]^{1/3} \quad \text{.....(D2)}$$

$$N_c' = 16.3 \int_0^{V_c} \frac{dV_c}{T_{V_c}} \quad \text{(D3)}$$

where V_c was the freeboard in the magnesium retort. The integral was evaluated numerically by considering the temperature and volume of each section of the retort.

The volume of the bubble was

$$V_B^0 = \frac{\pi}{6} (D_E^0)^3 \quad \text{(D4)}$$

and its equivalent area was

$$A_E^0 = \pi (D_E^0)^2 \quad \text{(D5)}$$

The frequency of bubble formation was

$$f = Q/V_B^0 \quad \text{(D6)}$$

The rising velocity was calculated from the Davies and Taylor² formula:

$$U = 22.6(D_E^0)^{1/2} \quad (D7)$$

thus, the rising time was

$$t_R = h/U \quad (D8)$$

The slopes of the magnesium and sulphur curves against time were $\Delta\% \text{ Mg}/\Delta t$ and $\Delta\% \text{ S}/\Delta t$, respectively. The molar rates of transfer were:

$$\dot{N}_{\text{Mg}} = \frac{\Delta\% \text{ Mg}}{\Delta t} \frac{W_{\text{Fe}}}{2430} \quad (D9)$$

$$\dot{N}_{\text{MgS}} = \frac{-\Delta\% \text{ S}}{\Delta t} \frac{W_{\text{Fe}}}{3206} \quad (D10)$$

for the whole bath. The molar rate of injection was

$$\dot{N}_T = Q \frac{P}{RT} \quad (D11)$$

The final bubble volume and argon content at the bath surface were calculated from

$$\frac{V_B^F}{V_B^O} = \frac{X_{\text{Ar}}^O}{X_{\text{Ar}}^F} = 1 - \frac{\dot{N}_{\text{Mg}} + \dot{N}_{\text{MgS}}}{\dot{N}_T} \quad (D12)$$

The final equivalent area A_E^F was calculated from Equation (D5) and the average total interfacial area in the melt at each instant was

$$A'' = \left(\frac{A_E^O + A_E^F}{2} \right) f_B t_R + \frac{A_E^O}{2} \quad (D13)$$

The apparent molar flux of magnesium from the bubbles and sulphur to them were

$$\dot{N}_{Mg}'' = \frac{\dot{N}_{Mg}}{A''} \quad (D14)$$

and

$$\dot{N}_{MgS}'' = \frac{\dot{N}_{MgS}}{A''} \quad (D15)$$

The apparent first order rate constants (or mass transfer coefficients) were then

$$k_{LMg} = \frac{\dot{N}_{Mg}''}{\bar{C}_{Mg}^*} \quad (D16)$$

and

$$k_{LS} = \frac{\dot{N}_{MgS}''}{C_S} \quad (D17)$$

where \bar{C}_{Mg}^* was the average equilibrium interfacial molar concentration of magnesium throughout bubble rise:

$$\bar{C}_{Mg}^* = 2.02 \times 10^{-3} (1 - \bar{X}_{Ar}) \quad (D18)$$

The analysis in the text indicated that almost all of the magnesium dissolved before desulphurization occurred, thus the magnesium mass transfer coefficient was recalculated to include the desulphurization. Evaporation from the bath surface was also incorporated:

$$\dot{N}_{EV} = k_{EV} A_{BATH} C_{Mg} \quad (D19)$$

$$= 7.72 \times 10^{-3} \% \text{ Mg (mole s}^{-1}\text{)} \quad (D20)$$

but this correction later was generally small. Thus the total mass transfer coefficient was calculated from

$$k_L = \frac{\dot{N}_{Mg} + \dot{N}_{MgS} + \dot{N}_{EV}}{A'' \bar{C}_{Mg}^*} \quad (D21)$$

The average value was quoted in the text.

REFERENCES

1. Irons, G.A. and Guthrie, R.I.L.: Met. Trans. B, Vol. 9B, (1978), pp.101-10.
2. Davies, R.M. and Taylor, G.I.: Proc. Roy. Soc. (London), Vol. A200, (1950), pp.375-87.

APPENDIX E
COMPUTER SIMULATIONS

As discussed in the text, a WAT5 FORTRAN-language computer program was developed to ensure that the interpretation of the results was in fact correct, and could "predict" the results given certain initial conditions. Referring to the computer print-out in this Appendix, one can see that these conditions are read in line 4. They include the starting magnesium and sulphur levels, the apparent second order rate constant, the magnesium solubility, the magnesium and sulphur mass transfer coefficients, the evaporative mass transfer coefficient, the flow rate, the magnesium partial pressure, the total bubble area, the bath weight, the iteration time interval, and the bubbling and holding times, respectively. The symbols are explained at the end of this Appendix. The data is displayed in lines 75 to 83 for the experimental runs. The data is checked from lines 6 to 19. The procedures are initialized down to line 24. The 'do-loop' for successive time iterations for the mass transfer is contained between lines 25 and 70. Line 29 calculated NT which is the total amount of magnesium dissolved in the iron according to the experimental mass transfer coefficient. The amount of sulphur reacted, NDES, is calculated according to the experimentally determined second-order rate equation. From lines 32 to 37 a check is made to make sure NDES is not greater than NT. The correction for magnesium evaporation from the bath surface is performed in line 38. The new sulphur and magnesium contents, PCS and PCMG are then calculated in lines 39 and 40. NQ, the

number of moles of magnesium added to the bath up to that time, and thus the magnesium weight percent added, PCA, are calculated in the next 2 lines. In lines 43 and 44 the magnesium recovery, MR and desulphurization efficiency, DSE, up to that time are calculated. Lines 45 to 56 control the format of print-out. From lines 57 to the end, the holding period is considered. Magnesium is allowed to evaporate (line 58) so that the magnesium content decreases (line 62) in each time increment.

NOMENCLATURE

<u>Symbol</u>	<u>Significance</u>
A	equivalence spherical area of all the bubbles in the bath, cm^2
AB	surface area of the bath, cm^2
CH	variable used in a check
DT	iteration time interval, s
DSE	desulphurization efficiency, defined in the text
HC	Henry's Constant, $\% \text{ Mg} \cdot (\text{atm Mg})^{-1}$
I, IC, IS, J	'Do-loop' counters
K	second order rate constant, $\text{mole} \cdot \%^{-2} \text{s}^{-1}$
KLE	mass transfer coefficient for evaporation, cm s^{-1}
KLMG	mass transfer coefficient for magnesium dissolution, cm s^{-1}
KLS	mass transfer coefficient for sulphur transport to the bubbles, cm s^{-1}
MR	magnesium recovery, used in text
NDES	number of moles desulphurized in each time increment by the second order reaction, mole

<u>Symbol</u>	<u>Significance</u>
NMG	residual number of moles of magnesium dissolved in each time increment after the desulphurization is considered, mole
NMGS	total number of moles desulphurized in each time increment, mole
NQ	number of moles of magnesium injected in each time increment, mole
NT	number of moles of magnesium dissolved in each time increment, without considering dissolution, mole
PCA	magnesium injected as a percent of the bath weight, %
PCMG	magnesium content of the bath, %
PCMGO	initial magnesium content of the bath, %
PCS	sulphur content of the bath, %
PCSO	initial sulphur content of the bath, %
PMG	partial pressure of the magnesium in the bubble, atm.
Q	total gas flow rate, cm^3s^{-1}
T	real time in the simulation, s
TB	duration of bubbling period, min
TH	duration of holding period, min
TM	real time in the simulation, min
TP	time counter, s
WFE	bath weight, g


```

0001 /LOAD WAT5
0002 REAL KLMG,KLS,K,NT,NMG,NMGS,KLE,NDES,NQ,MR
0003 DO 16 J=1,20
0004 READ(5,*)PCMG0,PCSO,K,HC,KLMG,KLS,KLE,Q,PMG,A,WFE,DT,TB,TH
0005 IF(PCMG0.EQ.9.)GO TO 17
0006 WRITE(6,100)PCMG0,PCSO,K,HC,KLMG,KLS,KLE,Q,PMG,A,WFE,DT,TB,TH
0007 100 FORMAT(1H ,/,/,',PCMG0=',I7.4,/,',PCSO=',F7.4,/,
0008 @'K=',F6.3,/,',HC=',F6.3,/,
0009 @'KLMG=',F8.5,/,',KLS=',F8.5,/,
0010 @'KLE=',F8.5,/,',Q=',F10.2,/,
0011 @'PMG=',F7.4,/,',A=',F10.2,/,
0012 @'WFE=',F12.1,/,',DT=',F9.5,/,
0013 @'TB=',F5.1,/,',TH=',F5.1)
0014 PCMG=PCMG0
0015 PCS=PCSO
0016 NT=.00288*KLMG*A*(HC*PMG-PCMG)*DT
0017 CH=8.18E-06*PMG*Q*DT
0018 IF(NT.GT.CH)WRITE(6,105)
0019 105 FORMAT(1H ,',MR IS GREATER THAN 1')
0020 TP=0.
0021 IC=0
0022 IS=0
0023 T=0.
0024 AB=304.
0025 DO 10 I=1,10000
0026 T=T+DT
0027 TP=TP+DT
0028 IF(T.GT.TB*60.)GO TO 20
0029 NT=.00288*KLMG*A*(HC*PMG-PCMG)*DT
0030 NDES=K*(PCMG*PCS-8.E-06)*DT
0031 NMGS=NDES+.00218*KLS*A*PCS*DT
0032 NMG=NT-NDES
0033 IF(NMG.GT.0.)GO TO 11
0034 IC=IC+1
0035 IF(IC.EQ.1)WRITE(6,101)
0036 101 FORMAT(1H ,',NMG WAS NEGATIVE')
0037 11 CONTINUE
0038 NMG=NMG-.00288*KLE*AB*PMG*DT
0039 PCS=PCS-3206.*NMGS/WFE
0040 PCMG=PCMG+2430.*NMG/WFE
0041 NQ=8.18E-06*PMG*Q*T
0042 PCA=NQ*2430./WFE

```

```

0043      MR=((PCMG-PCMG0)*WFE/2430.+(PCSO-PCS)*WFE/3206.)/NQ
0044      DSE=(PCSO-PCS)*WFE/3206./NQ
0045      IF(I.EQ.1)WRITE(6,102)NT,NQ
0046 102   FORMAT(1H , 'NT=' ,E11.4,/, 'NQ=' ,E11.4,/,/,
0047      @'T(MIN)',5X,'PCA',5X,'PCMG',6X,'PCS',
0048      @6X,'MR',7X,'DSE',/)
0049      IF((PCS.LE.0.).OR.(PCMG.LE.0.))GO TO 16
0050      IF((TP.LT.119.9999).OR.(TP.GT.120.0001))GO TO 10
0051      TP=0.
0052      TM=T/60.
0053      WRITE(6,103)TM,PCA,PCMG,PCS,MR,DSE
0054 103   FORMAT(1H ,F6.2,5(3X,F6.4))
0055      GO TO 10
0056 20    CONTINUE
0057      IF(T.GT.(60.*(TB+TH)))GO TO 16
0058      NMG=.00288*KLE*AB*PCMG*DT
0059      IF(IS.EQ.0)WRITE(6,104)
0060 104   FORMAT(1H ,/)
0061      IS=IS+1
0062      PCMG=PCMG-2430.*NMG/WFE
0063      MR=((PCMG-PCMG0)*WFE/2430.+(PCSO-PCS)*WFE/3206.)/NQ
0064      DSE=(PCSO-PCS)*WFE/3206./NQ
0065      IF((PCS.LE.0.).OR.(PCMG.LE.0.))GO TO 16
0066      IF((TP.LT.599.9999).OR.(TP.GT.600.0001))GO TO 10
0067      TP=0.
0068      TM=T/60.
0069      WRITE(6,103)TM,PCA,PCMG,PCS,MR,DSE
0070 10    CONTINUE
0071 16    CONTINUE
0072 17    STOP
0073      END
0074 $DATA
0075 .002 .0007 .92 .7 .0046 .0046 .00881 381. 1. 162. 58160. 12. 23. 30.
0076 .0022 .0032 .92 .7 .0046 .0046 .00881 219. 1. 94.7 58160. 12. 32. 60.
0077 .002 .0036 .92 .7 .0046 .0046 .00881 125. .845 94.4 62890. 12. 60. 60.
0078 .002 .19 .92 .7 .0046 .0046 .00881 107. .819 84.6 62890. 12. 60. 60.
0079 .002 .056 .92 .7 .0046 .0046 .00881 53.1 .885 40.8 64920. 12. 52. 60.
0080 .0019 .056 .92 .7 .0046 .0046 .00881 76.8 .747 58.2 64290. 12. 44. 60.
0081 .0018 .054 .92 .7 .0046 .0046 .00881 80. .757 53.4 64290. 12. 60. 60.
0082 .0018 .0624 .92 .7 .0046 .0046 .00881 256. .72 106. 61540. 12. 60. 60.
0083 .0015 .064 .92 .7 .0046 .0046 .00881 73. .734 104. 63570. 12. 60. 60.
0084 9. 9. 9. 9. 9. 9. 9. 9. 9. 9. 9. 9. 9. 9.
*END

```

APPENDICESLIST OF FIGURES

- Figure B1 Magnesium solubility in cast iron.
- Figure D1 Magnesium and sulphur contents as a function of time
for Run 2. The curves represent the results of the
computer model.
- Figure D2 Magnesium and sulphur contents as a function of time
for Run 7. The curves represent the results of the
computer model.
- Figure D3 Magnesium and sulphur contents as a function of time
for Run 13. The curves represent the results of the
computer model.
- Figure D4 Magnesium and sulphur contents as a function of time
for Run 14. The curves represent the results of the
computer model.
- Figure D5 Magnesium and sulphur contents as a function of time
for Run 16. The curves represent the results of the
computer model.

APPENDICESLIST OF TABLES

Table A1	Industrial Desulphurization Practice
Table B1	Comparison of H' Values
Table C1	Mass Transfer Correlations for Single Bubbles with Mobile Interfaces
Table C2	Mass Transfer Correlations for Single Bubbles with Immobile Interfaces
Table D1	Rate Calculations